Course 12

SUPERCONDUCTING QUBITS

Michel H. Devoret[†] and John M. Martinis*

† *Applied Physics Department, Yale University, New Haven CT 06520*
* *National Institute of Standards and Technology, Boulder CO 80305*

D. Estève, J.-M. Raimond and J. Dalibard, eds.
Les Houches, Session LXXIX, 2003
Quantum Entanglement and Information Processing
Intrication quantique et traitement de l'information

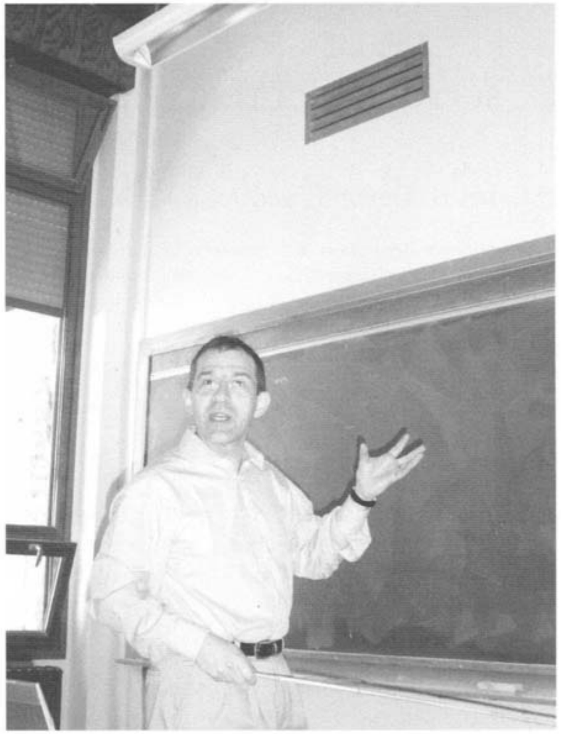

Contents

1. Introduction

1.1. The problem of implementing a quantum computer

The theory of information has been revolutionized by the discovery that quantum algorithms can run exponentially faster than their classical counterparts, and by the invention of quantum error-correction protocols [1]. These fundamental breakthroughs have lead scientists and engineers to imagine building entirely novel types of information processors. However, the construction of a computer exploiting quantum – rather than classical – principles represents a formidable scientific and technological challenge. While quantum bits must be strongly inter-coupled by gates to perform quantum computation, they must at the same time be completely decoupled from external influences, except during the write, control and readout phases when information must flow in and out of the quantum computer. This difficulty does not exist for conventional (classical) bits, which follow irreversible dynamics that damp the noise of the environment.

Most proposals for implementing a quantum computer have been based on qubits constructed from microscopic degrees of freedom: electron or nuclear spin, atomic transition dipoles and so on (see other lectures in this book). These degrees of freedom are naturally very well isolated from their environment, and hence decohere very slowly. The main challenge of these implementations is enhancing the inter-qubit coupling to the level required for fast gate operations without introducing decoherence from parasitic environmental modes and noise.

In this review, we will discuss a radically different experimental approach based on "quantum integrated circuits," where qubits are constructed from *collective* electrodynamic modes of macroscopic electrical elements, rather than microscopic degrees of freedom. An advantage of this approach is that these qubits have an intrinsically large electromagnetic cross-section, which implies they may be easily coupled together in complex topologies via simple linear electrical elements like capacitors, inductors, and transmission lines. However, strong coupling also presents a related challenge: is it possible to isolate these electrodynamic qubits from ambient parasitic noise while retaining open communication channels for the write, control, and read operations? The main purpose of this article is to review the considerable progress that has been made in the past few years towards this goal, and to explain how new ideas about methodology and materials are likely to improve coherence to the threshold needed for quantum error correction.

1.2. Scope of this review

Before starting our discussion, we must warn the reader that this review is atypical in that it is neither historical nor exhaustive. Some important works have not been included or are only partially covered. We have on purpose narrowed our focus: we adopt the point of view of an engineer trying to determine the best strategy for building a reliable machine with given performances. This approach obviously runs the risk of presenting a biased and even incorrect account of recent scientific results, since the optimization of a complex system is always a intricate process with many hidden passageways and dead-ends. We hope nevertheless that the following sections will at least stimulate discussions on how to harness the physics of quantum integrated circuits into a mature quantum information processing technology.

After ending this introduction with a general presentation of quantum integrated circuits, we will first treat the simplest example of circuits, the superconducting linear LC oscillator. Although it cannot lead to a useful qubit, this circuit allows the presentation of the circuit variables and parameters with minimal mathematical complications. We will then introduce the Josephson junction as the crucial non-linear, non-dissipative element. The problem of dealing with the fluctuations in the offset charge of the junction will lead us to the three basic types of superconducting qubits. After showing how their coherence is affected by the intrinsic noise of the junction we will embark on the discussion of how to design a faithful and fast readout without compromising the coherence. Issues associated with quantum gates will be finally dealt with.

2. Basic features of quantum integrated circuits

2.1. Ultra-low dissipation: superconductivity

For an integrated circuit to behave quantum mechanically, the first requirement is very low dissipation. More specifically, all metallic parts need to be made out of a material that has negligible resistance at the qubit operating temperature and at the qubit transition frequency. The loss of only one energy quantum completely spoils quantum coherence. Low temperature superconductors [2] such as aluminium or niobium are therefore ideal for the task of carrying quantum signals. For this reason, quantum integrated circuit implementations have been nicknamed "superconducting qubits"[1].

2.2. *Ultra-low noise : low temperature*

The degrees of freedom of the quantum integrated circuit must be cooled to temperatures where the typical energy kT of thermal fluctuations is much less that the energy quantum $\hbar\omega_{01}$ associated with the transition between the states |qubit=0> and |qubit=1>. For reasons which will become clear in subsequent sections, this frequency for superconducting qubits is in the 5-20GHz range and therefore, the operating temperature temperature T must be around 20mK (Recall that 1K corresponds to about 20 GHz). These temperatures may be readily obtained by cooling the chip with a dilution refrigerator. Perhaps more importantly though, the "electromagnetic temperature" of the wires of the control and readout ports connected to the chip must also be cooled to these low temperatures, which requires careful electromagnetic filtering. Note that electromagnetic damping mechanisms are usually stronger at low temperatures than those originating from electron-phonon coupling. The techniques [3] and requirements [4] for ultra-low noise filtering have been known for about 20 years. From the requirements $kT \ll \hbar\omega_{01}$ and $\hbar\omega_{01} \ll \Delta$, where Δ is the energy gap of the superconducting material, one must use superconducting materials with a transition temperature greater than about 1K.

2.3. *Non-linear, non-dissipative elements: tunnel junctions*

Quantum signal processing cannot be performed using only purely linear components. In quantum circuits, however, the non-linear elements must obey the additional requirement of being non-dissipative. Elements like PIN diodes or CMOS transistors are thus forbidden, even if they could be operated at ultra-low temperatures.

There is only one electronic element that is both non-linear and non-dissipative at arbitrarily low temperatures: the superconducting tunnel junction (also known as a Josephson tunnel junction [5]). As illustrated in Fig. 1, this circuit element consists of a sandwich of two superconducting thin films separated by an insulating layer that is thin enough (typically $\sim$1nm) to allow tunneling of discrete charges through the barrier. In later sections we will describe how the tunneling of Cooper pairs creates a strong non-linear inductance, thus yielding viable

---

[1] In principle, other condensed phases of electrons, such as high-Tc superconductivity or the quantum Hall effect, both integer and fractional, are possible and would also lead to quantum integrated circuits of the general type discussed here. We do not pursue this subject further than this note, however, because dissipation in these new phases is, by far, not as well understood as in low-Tc superconductivity.

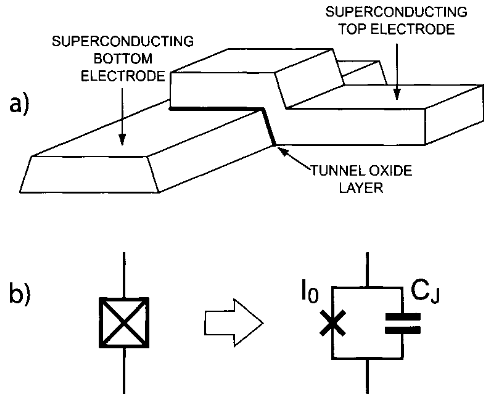

Fig. 1. a) Josephson tunnel junction made with two superconducting thin films; b) Schematic representation of a Josephson tunnel junction. The irreducible Josephson element is represented by a cross.

qubit energy levels. The tunnel barrier is typically fabricated from oxidation of the superconducting metal, which results in a reliable barrier since the oxidation process is self-terminating [6]. The materials properties of amorphous aluminum oxide (alumina) make it an attractive tunnel insulating layer. In part because of its well-behaved oxide, aluminim is the material from which good quality tunnel junctions are most easily fabricated, it is often said that aluminium is to superconducting quantum circuits what silicon is to conventional MOSFET circuits. Although the Josephson effect is a subtle physical effect involving a combination of tunneling and superconductivity, the junction fabrication process is relatively straightforward.

2.4. *Design and fabrication of quantum integrated circuits*

Superconducting junctions and wires are fabricated using techniques borrowed from conventional integrated circuits[2]. Quantum circuits are typically made on silicon wafers using optical or electron-beam lithography and thin film deposition. They present themselves as a set of micron-size or sub-micron-size circuit elements (tunnel junctions, capacitors, and inductors) connected by wires or transmission lines. The size of the chip and elements are such that, to a large extent, the electrodynamics of the circuit can be analyzed using simple transmission line equations or even a lumped element approximation. Contact to the chip

---

[2] It is worth mentioning that chips with tens of thousands of junctions have been successfully fabricated for the voltage standard and for the Josephson signal processors, which are only exploiting the speed of Josephson elements, not their quantum properties.

is made by wires bonded to mm-size metallic pads. The circuit can be designed using conventional layout and classical simulation programs.

Thus, many of the design concepts and tools of conventional electronics can be directly applied to quantum circuits. Nevertheless, there are still important differences between conventional and quantum circuits at the conceptual level.

2.5. *Integrated circuits that obey macroscopic quantum mechanics*

At the conceptual level, conventional and quantum circuits differ in that, in the former, the collective electronic degrees of freedom such as currents and voltages are classical variables, whereas in the latter, these degrees of freedom must be treated by quantum operators which do not necessarily commute. A more concrete way of presenting this rather abstract difference is to say that a typical electrical quantity, such as the charge on the plates of a capacitor, can be thought of as a simple number is conventional circuits, whereas in quantum circuits, the charge on the capacitor must be represented by a wave function giving the probability amplitude of all charge configurations. For example, the charge on the capacitor can be in a superposition of states where the charge is both positive and negative at the same time. Similarly the current in a loop might be flowing in two opposite directions at the same time. These situations have originally been nicknamed "macroscopic quantum effects" by Tony Leggett [7] to emphasize that quantum integrated circuits are displaying phenomena involving the collective behavior of many particles, which are in contrast to the usual quantum effects associated with microscopic particles such as electrons, nuclei or molecules[3].

2.6. *DiVicenzo criteria*

We conclude this section by briefly mentioning how quantum integrated circuits satisfy the so-called DiVicenzo criteria for the implementation of quantum computation [8]. The non-linearity of tunnel junctions is the key property ensuring that non-equidistant level subsystems can be implemented (criterion # 1: qubit existence). As in many other implementations, initialization is made possible (criterion #2: qubit reset) by the use of low temperature. Absence of dissipation in superconductors is one of the key factors in the quantum coherence of the system (criterion # 3: qubit coherence). Finally, gate operation and readout (criteria #4 and #5) are easily implemented here since electrical signals confined to and traveling along wires constitute very efficient coupling methods.

---

[3] These microscopic effects determine also the properties of materials, and explain phenomena such as superconductivity and the Josephson effect itself. Both classical and quantum circuits share this bottom layer of microscopic quantum mechanics.

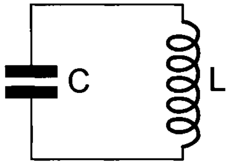

Fig. 2. Lumped element model for an electromagnetic resonator: LC oscillator.

3. The simplest quantum circuit

3.1. *Quantum LC oscillator*

We consider first the simplest example of a quantum integrated circuit, the LC oscillator. Although it cannot lead to a useful qubit, this circuit allows us to describe general key circuit variables and parameters with minimal mathematical complications. As shown in Fig. 2, it consists of an inductor L connected to a capacitor C, all metallic parts being superconducting. This simple circuit is the lumped-element version of a superconducting cavity or a transmission line resonator (for instance, the link between cavity resonators and LC circuits is elegantly discussed by Feynman [9]). The equations of motion of the LC circuit are those of an harmonic oscillator. It is convenient to take the position coordinate as being the flux Φ in the inductor, while the role of the conjugate momentum is played by the charge Q on the capacitor. The variables Φ and Q have to be treated as canonically conjugate quantum operators that obey $[\Phi, Q] = i\hbar$. The Hamiltonian of the circuit is $H = \frac{1}{2}\Phi^2/L + \frac{1}{2}Q^2/C$, which can be equivalently written as $H = \hbar\omega_0(n + \frac{1}{2})$ where n is the number operator for photons in the resonator and $\omega_0 = 1/\sqrt{LC}$ is the resonance frequency of the oscillator. It is important to note that the parameters of the circuit Hamiltonian are not fundamental constants of Nature. They are engineered quantities with a large range of possible values which can be modified easily by changing the dimensions of elements, a standard lithography operation. It is in this sense, in our opinion, that the system is unambiguously "macroscopic". The other important combination of the parameters L and C is the characteristic impedance $Z = \sqrt{L/C}$ of the circuit. Along with the residual resistance of the circuit and/or its radiation loss, both of which we can model as a series resistance R, this impedance determines the quality factor of the oscillation: $\mathcal{Q} = Z/R$. The theory of the harmonic oscillator shows that a quantum superposition of ground state and first excited state decays on a time scale precisely given by $1/RC$, yielding a quality factor for quantum coherence limited by $\mathcal{Q}$. These considerations illustrate the very useful general link between the classical measure of dissipation and the upper limit of the quantum coherence time.

3.2. Practical considerations

In practice, the circuit shown in Fig. 2 may be fabricated using planar components with lateral dimensions around 10μm, giving values of L and C approximately 0.1nH and 1pF, respectively, and yielding $\omega_0/2\pi \simeq$ 16GHz and $Z_0 = 10\Omega$. If we use aluminium, a good BCS superconductor with transition temperature of 1.1K and a gap $\Delta/e \simeq 200\mu V$, dissipation from the breaking of Cooper pairs will begin at frequencies greater than $2\Delta/h \simeq$ 100GHz. The residual resistivity of a BCS superconductor decreases exponentially with the inverse of temperature and linearly with frequency, as shown by the Mattis-Bardeen (MB) formula $\rho(\omega) \sim \rho_0 \frac{\hbar\omega}{k_B T} \exp(-\Delta/k_B T)$ [10], where ρ_0 is the resistivity of the metal in the normal state (we are treating here the case of the so-called "dirty" superconductor [11], which is well adapted to thin film systems). According to MB, the intrinsic losses of the superconductor, at the temperature and frequency (typically 20mK and 20GHz) characterizing the qubit dynamics, can be safely neglected. However, we must warn the reader that the intrisinsic losses in the superconducting material do not exhaust, by far, the causes of dissipation, even if very high quality factors have been demonstrated in superconducting cavity experiments [12].

3.3. Matching to the vacuum impedance: a useful feature, not a bug

Although the intrisinsic dissipation of superconducting circuits can be made very small, losses are in general governed by the coupling of the circuit with the electromagnetic environment that is present in the form of write, control and readout lines. These lines (which we also refer to as ports) have a characteristic propagation impedance $Z_c \simeq 50\Omega$, which is constrained to be a fraction of the impedance of the vacuum $Z_{\text{vac}} = 377\Omega$. It is thus easy to see that our LC circuit, with a characteristic impedance of $Z_0 = 10\Omega$, tends to be rather well impedance-matched to any pair of leads. This circumstance occurs very frequently in circuits, and almost never in microscopic systems such as atoms which interact very weakly with electromagnetic radiation[4]. Matching to Z_{vac} is a useful feature because it allows strong coupling for writing, reading, and logic operations. As we mentioned earlier, the challenge with quantum circuits is to isolate them from parasitic degrees of freedom. **The major task of this review is to explain how this has been achieved so far and what level of isolation is attainable.**

---

[4] The impedance of an atom can be crudely seen as being given by the impedance quantum $R_K = h/e^2$. We live in a universe where the ratio $Z_{vac}/2R_K$, also known as the fine structure constant 1/137.0, is a small number.

3.4. The consequences of being macroscopic

While our example shows that quantum circuits can be mass-produced by standard microfabrication techniques and that their parameters can be easily engineered to reach some optimal condition, it also points out evident drawbacks of being macroscopic for qubits.

The engineered quantities L and C can be written as

$$\begin{aligned} L &= L^{stat} + \Delta L(t) \\ C &= C^{stat} + \Delta C(t) \end{aligned} \tag{3.1}$$

a) The first term on the right-handside denotes the static part of the parameter. It has **statistical variations**: unlike atoms whose transition frequencies in isolation are so reproducible that they are the basis of atomic clocks, circuits will always be subject to parameter variations from one fabrication batch to another. Thus prior to any operation using the circuit, the transition frequencies and coupling strength will have to be determined by "diagnostic" sequences and then taken into account in the algorithms.

b) The second term on the right-handside denotes the time-dependent fluctuations of the parameter. It describes **noise** due to residual material defects moving in the material of the substrate or in the material of the circuit elements themselves. This noise can affect for instance the dielectric constant of a capacitor. The low frequency components of the noise will make the resonance frequency wobble and contribute to the dephasing of the oscillation. Furthermore, the frequency component of the noise at the transition frequency of the resonator will induce transitions between states and will therefore contribute to energy relaxation.

Let us stress that statistical variations and noise are not problems affecting superconducting qubit parameters only. For instance when several atoms or ions are put together in microcavities for gate operation, patch potential effects lead to expressions similar in form to Eq. 3.1 for the parameters of the hamiltonian, even if the isolated single qubit parameters are fluctuation-free.

3.5. The need for non-linear elements

Not all aspects of quantum information processing using quantum integrated circuits can be discussed within the framwork of the LC circuit which lacks an important ingredient: non-linearity. In the harmonic oscillator, all transitions between neighbouring states are degenerate as a result of the parabolic shape of the potential. In order to have a qubit, the transition frequency between states |qubit=0> and |qubit=1> must be sufficiently different from the transition between higher-lying eigenstates, in particular 1 and 2. Indeed, the maximum number of 1-qubit operations that can be performed coherently scales as $\mathcal{Q}_{01} \left|\omega_{01} - \omega_{12}\right| / \omega_{01}$ where $\mathcal{Q}_{01}$ is the quality factor of the $0 \to 1$ transition. Josephson tunnel junctions are crucial for quantum circuits since they have a strongly non-parabolic, inductive potential energy.

4. The Josephson non-linear inductance

At low temperatures, and at the low voltages and low frequencies corresponding to quantum information manipulation, the Josephson tunnel junction behaves as a pure non-linear inductance (Josephson element) in parallel with the capacitance corresponding to the parallel plate capacitor formed by the two overlapping films of the junction (Fig. 1b). This minimal, yet precise model, allows arbitrary complex quantum circuits to be analysed by a quantum version of conventional circuit theory. Even though the tunnel barrier is a layer of order ten atoms thick, the value of the Josephson non-linear inductance is very robust against static disorder, just like an ordinary inductance – such as the one considered in section 3 – is very insensitive to the position of each atom in the wire. We refer to [13] for a detailed discussion of this point.

4.1. Constitutive equation

Let us recall that a linear inductor, like any electrical element, can be fully characterized by its constitutive equation. Introducing a generalization of the ordinary magnetic flux, which is only defined for a loop, we define the **branch flux of an electric element** by $\Phi(t) = \int_{-\infty}^{t} V(t_1)dt_1$, where $V(t)$ is the space integral of the electric field along a current line inside the element. In this language, the current $I(t)$ flowing through the inductor is proportional to its branch flux $\Phi(t)$:

$$I(t) = \frac{1}{L}\Phi(t) \tag{4.1}$$

Note that the generalized flux $\Phi(t)$ can be defined for any electric element with two leads (dipole element), and in particular for the Josephson junction, even though it does not resemble a coil. The Josephson element behaves inductively, as its branch flux-current relationship [5] is:

$$I(t) = I_0 \sin\left[2\pi\Phi(t)/\Phi_0\right] \tag{4.2}$$

This inductive behavior is the manifestation, at the level of collective electrical variables, of the inertia of Cooper pairs tunneling across the insulator (kinetic inductance). The discreteness of Cooper pair tunneling causes the periodic flux dependence of the current, with a period given by a universal quantum constant Φ_0, the superconducting flux quantum $h/2e$. The junction parameter I_0 is called the critical current of the tunnel element. It scales proportionally to the area of the tunnel layer and diminishes exponentially with the tunnel layer thickness. Note that the constitutive relation Eq. 4.2 expresses in only one equation the two Josephson relations [5]. This compact formulation is made possible by the introduction of the branch flux.

The purely sinusoidal form of the constitutive relation Eq. 4.2 can be traced to the perturbative nature of Cooper pair tunneling in a tunnel junction. Higher harmonics can appear if the tunnel layer becomes very thin, though their presence would not fundamentally change the discussion presented in this review. The quantity $2\pi\Phi(t)/\Phi_0 = \delta$ is called the gauge-invariant phase difference accross the junction (often abridged into "phase"). It is important to realize that at the level of the constitutive relation of the Josephson element, this variable is nothing else than an electromagnetic flux in dimensionless units. In general, we have

$$\theta = \delta \bmod 2\pi$$

where θ is the phase difference between the two superconducting condensates on both sides of the junction. This last relation expresses how the superconducting ground state and electromagnetism are tied together.

4.2. Other forms of the parameter describing the Josephson non-linear inductance

The Josephson element is also often described by two other parameters, each of which carry exactly the same information as the critical current. The first one is the Josephson effective inductance $L_{J0} = \varphi_0/I_0$, where $\varphi_0 = \Phi_0/2\pi$ is the reduced flux quantum. The name of this other form becomes obvious if we expand the sine function in Eq. 4.2 in powers of Φ around $\Phi = 0$. Keeping the leading term, we have $I = \Phi/L_{J0}$. Note that the junction behaves for small signals almost as a point-like kinetic inductance: a 100nm×100nm area junction will have a typical inductance of 100nH, whereas the same inductance is only obtained magnetically with a loop of about 1cm in diameter. More generally, it is convenient to define the phase-dependent Josephson inductance

$$L_J(\delta) = \left(\frac{\partial I}{\partial \Phi}\right)^{-1} = \frac{L_{J0}}{\cos\delta}$$

Note that the Josephson inductance not only depends on δ, it can actually become infinite or negative! Thus, under the proper conditions, the Josephson

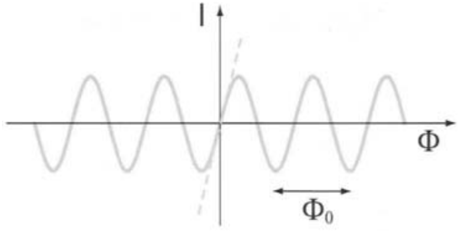

Fig. 3. Sinusoidal current-flux relationship of a Josephson tunnel junction, the simplest non-linear, non-dissipative electrical element (solid line). Dashed line represents current-flux relationship for a linear inductance equal to the junction effective inductance.

element can become a switch and even an active circuit element, as we will see below.

The other useful parameter is the Josephson energy $E_J = \varphi_0 I_0$. If we compute the energy stored in the junction as $E(t) = \int_{-\infty}^{t} I(t_1)\, V(t_1)\, dt_1$, we find $E(t) = -E_J \cos\left[2\pi\Phi(t)/\Phi_0\right]$. In contrast with the parabolic dependence on flux of the energy of an inductor, the potential associated with a Josephson element has the shape of a cosine washboard. The total height of the corrugation of the washboard is $2E_J$.

4.3. *Tuning the Josephson element*

A direct application of the non-linear inductance of the Josephson element is obtained by splitting a junction and its leads into 2 equal junctions, such that the resulting loop has an inductance much smaller the Josephson inductance. The two smaller junctions in parallel then behave as an effective junction [14] whose Josephson energy varies with Φ_{ext}, the magnetic flux externally imposed through the loop:

$$E_J(\Phi_{ext}) = E_J \cos(\pi\Phi_{ext}/\Phi_0) \tag{4.3}$$

Here, E_J the total Josephson energy of the two junctions. The Josephson energy can be modulated in a similar fashion by applying a magnetic field in the plane parallel to the tunnel layer.

5. The quantum isolated Josephson junction

5.1. *Form of the hamiltonian*

If we leave the leads of a Josephson junction unconnected, we obtain the simplest example of an non-linear electrical resonator. In order to analyse its quantum dynamics, we apply the prescriptions of quantum circuit theory briefly summarized in Appendix 1. Choosing a representation privileging the branch variables of the Josephson element, the momentum corresponds to the charge $Q = 2eN$ having tunneled through the element and the canonically conjugate position is the flux $\Phi = \varphi_0\theta$ associated with the superconducting phase difference across the tunnel layer. Here, N and θ are treated as operators that obey $[\theta, N] = i$. It is important to note that the operator N has integer eigenvalues whereas the phase θ is an operator corresponding to the position of a point on the unit circle (an angle modulo 2π).

By eliminating the branch charge of the capacitor, we obtain the hamiltonian

$$H = E_{CJ}(N - Q_r/2e)^2 - E_J\cos\theta \tag{5.1}$$

where $E_{CJ} = \frac{(2e)^2}{2C_J}$ is the Coulomb charging energy corresponding to one Cooper pair on the junction capacitance C_J and where Q_r is the residual offset charge on the capacitor.

One may wonder how the constant Q_r got into the hamiltonian, since no such term appeared in the corresponding LC circuit in section 3. The continuous charge Q_r is equal to the charge that pre-existed on the capacitor when it was wired with the inductor. Such offset charge is not some nit-picking theoretical construct. Its physical origin is a slight difference in work function between the two electrodes of the capacitor and/or an excess of charged impurities in the vicinity of one of the capacitor plates relative to the other. The value of Q_r is in practice very large compared to the Cooper pair charge $2e$, and since the hamiltonian 5.1 is invariant under the transformation $N \to N \pm 1$, its value can be considered completely random.

Such residual offset charge also exists in the LC circuit. However, we did not include it in our description of section 3 since a time-independent Q_r does not appear in the dynamical behavior of the circuit: it can be removed from the hamiltonian by performing a trivial canonical transformation leaving the form of the hamiltonian unchanged.

It is not possible, however, to iron this constant out of the isolated junction hamiltonian 5.1 because the potential is not quadratic in θ. The parameter Q_r plays a role here similar to the vector potential appearing in the hamiltonian of an electron in a magnetic field.

5.2. *Fluctuations of the parameters of the hamiltonian*

The hamiltonian 5.1 thus depends on three parameters which, following our discussion of the LC oscillator, we write as

$$\begin{aligned} Q_r &= Q_r^{stat} + \Delta Q_r(t) \\ E_C &= E_C^{stat} + \Delta E_C(t) \\ E_J &= E_J^{stat} + \Delta E_J(t) \end{aligned} \tag{5.2}$$

in order to distinguish the static sample-to-sample variation resulting from fabrication irreproducibility from the time-dependent fluctuations. While Q_r^{stat} can be considered fully random (see above discussion), E_C^{stat} and E_J^{stat} can generally be adjusted to a precision better than 20%. The relative fluctuations $\Delta Q_r(t)/2e$ and $\Delta E_J(t)/E_J$ are found to have a $1/f$ power spectral density with a typical standard deviations at 1Hz roughly of order $10^{-3}\text{Hz}^{-1/2}$ and $10^{-5}\text{Hz}^{-1/2}$, respectively, for a junction with a typical area of $0.01\mu\text{m}^2$ [15]. The noise appears to be produced by independent two-level fluctuators [16]. The relative fluctuations $\Delta E_C(t)/E_C$ are much less known, but the behavior of some glassy insulators at low temperatures might lead us to expect also a $1/f$ power spectral density, but probably with a weaker intensity than those of $\Delta E_J(t)/E_J$. We refer to the 3 noise terms in Eq.5.2 as offset charge, dielectric and critical current noises, respectively.

6. Why three basic types of Josephson qubits?

The first-order problem in realizing a Josephson qubit is to suppress as much as possible the detrimental effect of the fluctuations of Q_r, while retaining the nonlinearity of the circuit. There are three main stategies for solving this problem and they lead to three fundamental basic type of qubits involving only one Josephson element.

6.1. The Cooper pair box

The simplest circuit is called the "Cooper pair box" and was first described theoretically, albeit in a slightly different version than presented here, by M. Büttiker [17]. It was first realized experimentally by the Saclay group in 1997 [18]. Quantum dynamic in the time domain was first seen by the NEC group in 1999 [19]. In the Cooper pair box, the variations of the residual offset charge Q_r are compensated by biasing the Josephson tunnel junction with a voltage source U in series with a "gate" capacitor C_g (see Fig. 4a). One can easily show that the hamiltonian of the Cooper pair box is

$$H = E_C\left(N - N_g\right)^2 - E_J\cos\theta \tag{6.1}$$

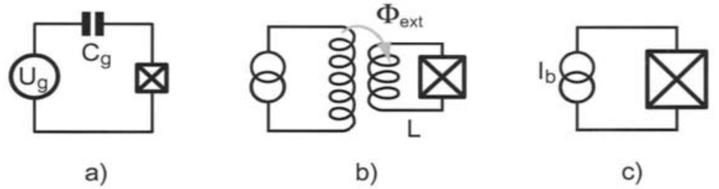

Fig. 4. a) Cooper pair box (prototypal charge qubit), b) RF-SQUID (prototypal flux qubit) and c) current-biased junction (prototypal phase qubit). The charge qubit and the flux qubit requires small junctions fabricated with e-beam lithography while the phase qubit can be fabricated with conventional optical lithography.

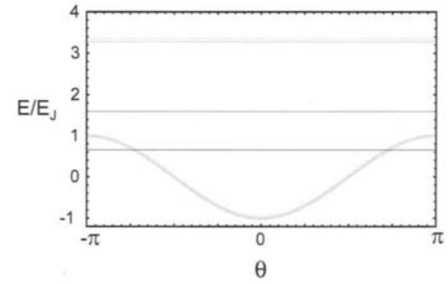

Fig. 5. Potential landscape for the phase in a Cooper pair box (thick solid line). The first few levels for $E_J/E_C = 1$ and $N_g = 1/2$ are indicated by thin horizontal solid lines.

Here $E_C = \frac{(2e)^2}{2(C_J+C_g)}$ is the charging energy of the island of the box and $N_g = Q_r + C_gU/2e$. Note that this hamiltonian has the same form as hamiltonian 5.1. Often N_g is simply written as $C_gU/2e$ since U at the chip level will deviate substantially from the generator value at high-temperature due to stray emf's in the low-temperature cryogenic wiring.

In Fig. 5 we show the potential in the θ representation as well as the first few energy levels for $E_J/E_C = 1$ and $N_g = 0$. As shown in Appendix 2, the Cooper pair box eigenenergies and eigenfunctions can be calculated with special functions known with arbitrary precision, and in Fig 6 we plot the first few eigenenergies as a function of N_g for $E_J/E_C = 0.1$ and $E_J/E_C = 1$. Thus, the Cooper box is to quantum circuit physics what the hydrogen atom is to atomic physics. We can modify the spectrum with the action of two externally controllable electrodynamic parameters: N_g, which is directly proportional to U, and E_J, which can be varied by applying a field through the junction or by using a split junction and applying a flux through the loop, as discussed in section 3. These parameters

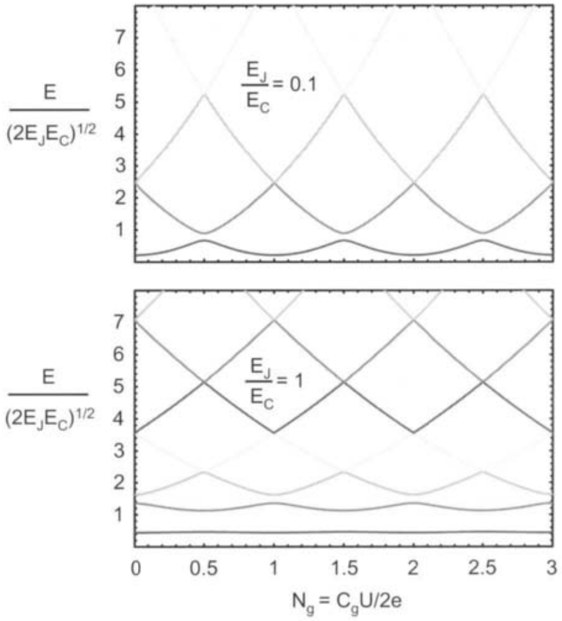

Fig. 6. Energy levels of the Cooper pair box as a function of N_g, for two values of E_J/E_C. As E_J/E_C increases, the sensitivity of the box to variations of offset charge diminishes, but so does the non-linearity. However, the non-linearity is the slowest function of E_J/E_C and a compromise advantageous for coherence can be found.

bear some resemblance to the Stark and Zeeman fields in atomic physics. For the box, however much smaller values of the fields are required to change the spectrum entirely.

We now limit ourselves to the two lowest levels of the box. Near the degeneracy point $N_g = 1/2$ where the electrostatic energy of the of the two charge states $|N=0\rangle$ and $|N=1\rangle$ are equal, we get the reduced hamiltonian [18,20]

$$H_{qubit} = -E_z\left(\sigma_Z + X_{control}\sigma_X\right) \tag{6.2}$$

where, in the limit $E_J/E_C \ll 1$, $E_z = \frac{E_J}{2}$and $X_{control} = 2\frac{E_C}{E_J}\left(\frac{1}{2} - N_g\right)$. In Eq. 6.2, σ_Z and σ_X refer to the Pauli spin operators, with the X direction being chosen along the charge operator, the variable of the box we can naturally couple to.

If we plot the energy of the eigenstates of 6.2 as a function of the control parameter $X_{control}$, we obtain the universal level repulsion diagram shown in

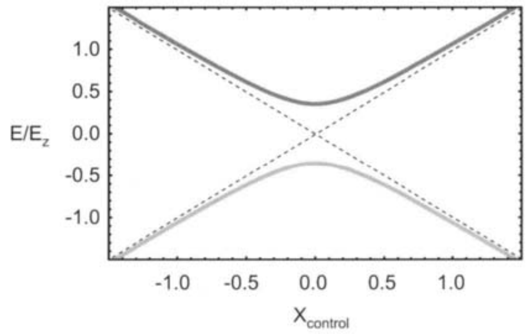

Fig. 7. Universal level anticrossing found both for the Cooper pair box and the RF-SQUID at their "sweet spot".

Fig. 7. Note that the minimum energy splitting is given by E_J. Comparing Eq. 6.2 with the spin hamiltonian in NMR, we see that E_J plays the role of the Zeeman field while the electrostatic energy plays the role of the transverse field. Indeed we can send on the control port corresponding to U time-varying voltage signals in the form of NMR-type pulses and prepare arbitrary superpositions of states [21].

The expression 6.2 shows that at the "sweet spot" $X_{control} = 0$, i.e. the degeneracy point $N_g = \frac{1}{2}$, the qubit transition frequency is to first order insentive to the offset charge noise ΔQ_r. We will discuss in the next section how an extension of the Cooper pair box circuit can display quantum coherence properties on long time scales by using this property.

In general, circuits derived from the Cooper pair box have been nicknamed "charge qubits". One should not think, however, that in charge qubits, quantum information is *encoded* with charge. Both the charge N and phase θ are quantum variables and they are both uncertain for a generic quantum state. Charge in "charge qubits" should be understood as refering to the "controlled variable", i.e. the qubit variable that couples to the control line we use to write or manipulate quantum information. In the following, for better comparison between the three qubits, we will be faithful to the convention used in Eq. 6.2, namely that σ_X represents the *controlled variable.*

6.2. *The RF-SQUID*

The second circuit – the so-called RF-SQUID [22] – can be considered in several ways the dual of the Cooper pair box (see Fig. 4b). It employs a superconducting transformer rather than a gate capacitor to adjust the hamiltonian. The two sides

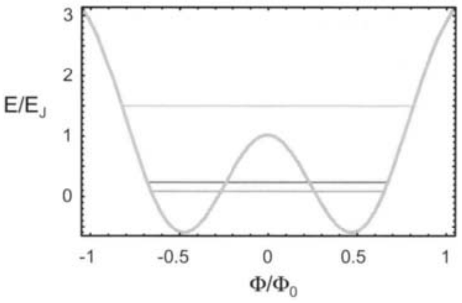

Fig. 8. Schematic potential energy landcape for the RF-SQUID.

of the junction with capacitance C_J are connected by a superconducting loop with inductance L. An external flux Φ_{ext} is imposed through the loop by an auxiliary coil. Using the methods of Appendix 1, we obtain the hamiltonian [7]

$$H = \frac{q^2}{2C_J} + \frac{\phi^2}{2L} - E_J \cos\left[\frac{2e}{\hbar}\left(\phi - \Phi_{ext}\right)\right] \tag{6.3}$$

We are taking here as degree of freedom the integral ϕ of the voltage across the inductance L, i.e. the flux through the superconducting loop, and its conjugate variable, the charge q on the capacitance C_J; $\left[\phi, q\right] = i\hbar$. Note that in this representation, the phase θ, corresponding to the branch flux across the Josephson element, has been eliminated. Note also that the flux ϕ, in contrast to the phase θ, takes its values on a line and not on a circle. Likewise, its conjugate variable q, the charge on the capacitance, has continuous eigenvalues and not integer ones like N. Note that we now have three adjustable energy scales: E_J, $E_{CJ} = \frac{(2e)^2}{2C_J}$ and $E_L = \frac{\Phi_0^2}{2L}$.

The potential in the flux representation is schematically shown in Fig. 8 together with the first few levels, which have been seen experimentally for the first time by the SUNY group [23]. Here, no analytical expressions exist for the eigenvalues and the eigenfunctions of the problem, which has two aspect ratios: E_J/E_{CJ} and $\lambda = L_J/L - 1$.

Whereas in the Cooper box the potential is cosine-shaped and has only one well since the variable θ is 2π-periodic, we have now in general a parabolic potential with a cosine corrugation. The idea here for curing the detrimental effect of the offset charge fluctuations is very different than in the box. First of all Q_r^{stat} has been neutralized by shunting the 2 metallic electrodes of the junction by the superconducting wire of the loop. Then, the ratio E_J/E_{CJ} is chosen to be much larger than unity. This tends to increase the relative strength

of quantum fluctuations of q, making offset charge fluctuations ΔQ_r small in comparison. The resulting loss in the non-linearity of the first levels is compensated by taking λ close to zero and by flux-biasing the device at the half-flux quantum value $\Phi_{ext} = \Phi_0/2$. Under these conditions, the potential has two degenerate wells separated by a shallow barrier with height $E_B = \frac{3\lambda^2}{2}E_J$. This corresponds to the degeneracy value $N_g = 1/2$ in the Cooper box, with the inductance energy in place of the capacitance energy. At $\Phi_{ext} = \Phi_0/2$, the two lowest energy levels are then the symmetric and antisymmetric combinations of the two wavefunctions localized in each well, and the energy splitting between the two states can be seen as the tunnel splitting associated with the quantum motion through the potential barrier between the two wells, bearing close resemblance to the dynamics of the ammonia molecule. This splitting E_S depends exponentially on the barrier height, which itself depends strongly on E_J. We have $E_S = \eta\sqrt{E_B E_{CJ}}\exp\left(-\xi\sqrt{E_B/E_{CJ}}\right)$ where the numbers η and ξ have to be determined numerically in most practical cases. The non-linearity of the first levels results thus from a subtle cancellation between two inductances: the superconducting loop inductance L and the junction effective inductance $-L_{J0}$ which is opposed to L near $\Phi_{ext} = \Phi_0/2$. However, as we move away from the degeneracy point $\Phi_{ext} = \Phi_0/2$, the splitting $2E_\Phi$ between the first two energy levels varies linearly with the applied flux $E_\Phi = \zeta\frac{\Phi_0^2}{2L}\left(N_\Phi - 1/2\right)$. Here the parameter $N_\Phi = \Phi_{ext}/\Phi_0$, also called the flux frustration, plays the role of the reduced gate charge N_g. The coefficient ζ has also to be determined numerically. We are therefore again, in the vicinity of the flux degeneracy point $\Phi_{ext} = \Phi_0/2$ and for $E_J/E_{CJ} \gg 1$, in presence of the universal level repulsion behavior (see Fig. 7) and the qubit hamiltonian is again given by

$$H_{qubit} = -E_z\left(\sigma_Z + X_{control}\sigma_X\right) \tag{6.4}$$

where now $E_z = E_S/2$ and $X_{control} = 2\frac{E_\Phi}{E_S}\left(\frac{1}{2} - N_\Phi\right)$. The qubits derived from this basic circuit [24,32] have been nicknamed "flux qubits". Again, quantum information is not directly represented here by the flux ϕ, which is as uncertain for a general qubit state as the charge q on the capacitor plates of the junction. The flux ϕ is the system variable to which we couple when we write or control information in the qubit, which is done by sending current pulses on the primary of the RF-SQUID transformer, thereby modulating N_Φ, which itself determines the strength of the pseudo-field in the X direction in the hamiltonian 6.4. Note that the parameters E_S, E_Φ, and N_Φ are all influenced to some degree by the critical current noise, the dielectric noise and the charge noise. Another independent noise can also be present, the noise of the flux in the loop, which is not found in the box and which will affect only N_Φ. Experiments on DC-SQUIDS [14] have shown

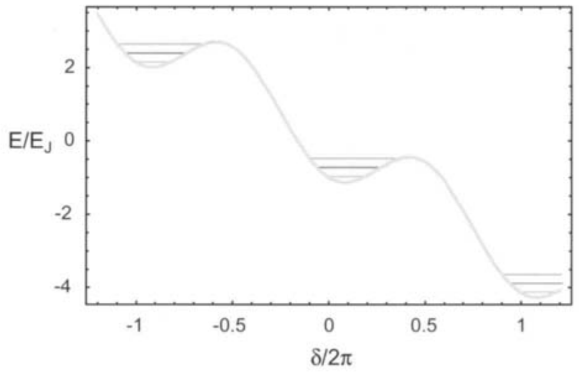

Fig. 9. Tilted washboard potential of the current-biased Josephson junction.

that this noise, in adequate conditions, can be as low as $10^{-8}(h/2e)/\mathrm{Hz}^{-1/2}$ at a few KHz. However, experimental results on flux qubits (see below) seem to indicate that larger apparent flux fluctuations are present, either as a result of flux trapping or critical current fluctuations in junctions implementing inductances.

6.3. Current-biased junction

The third basic quantum circuit biases the junction with a fixed DC-current source (Fig. 7c). Like the flux qubit, this circuit is also insensitive to the effect of offset charge and reduces the effect of charge fluctuations by using large ratios of E_J/E_{CJ}. A large non-linearity in the Josephson inductance is obtained by biasing the junction at a current I very close to the critical current. A current bias source can be understood as arising from a loop inductance with $L \rightarrow \infty$ biased by a flux $\Phi \rightarrow \infty$ such that $I = \Phi/L$. The Hamiltonian is given by

$$H = E_{CJ}p^2 - I\varphi_0\delta - I_0\varphi_0\cos\delta\,, \tag{6.5}$$

where the gauge invariant phase difference operator δ is, apart from the scale factor φ_0, precisely the branch flux across C_J. Its conjugate variable is the charge $2ep$ on that capacitance, a continuous operator. We have thus $[\delta, p] = i$. The variable δ, like the variable ϕ of the RF-SQUID, takes its value on the whole real axis and its relation with the phase θ is $\delta \bmod 2\pi = \theta$ as in our classical analysis of section 4.

The potential in the δ representation is shown in Fig. 9. It has the shape of a tilted washboard, with the tilt given by the ratio I/I_0. When I approaches I_0, the

phase is $\delta \approx \pi/2$, and in its vicinity, the potential is very well approximated by the cubic form

$$U(\delta) = \varphi_0(I_0 - I)(\delta - \pi/2) - \frac{I_0\varphi_0}{6}(\delta - \pi/2)^3 \tag{6.6}$$

Note that its shape depends critically on the difference $I_0 - I$. For $I \lesssim I_0$, there is a well with a barrier height $\Delta U = (2\sqrt{2}/3)I_0\varphi_0(1 - I/I_0)^{3/2}$ and the classical oscillation frequency at the bottom of the well (so-called plasma oscillation) is given by

$$\begin{aligned}\omega_p &= \frac{1}{\sqrt{L_J(I)C_J}}\\ &= \frac{1}{\sqrt{L_{J0}C_J}}\left[1 - (I/I_0)^2\right]^{1/4}\end{aligned}$$

Quantum-mechanically, energy levels are found in the well (see Fig. 11) [3] with non-degenerate spacings. The first two levels can be used for qubit states [25], and have a transition frequency $\omega_{01} \simeq 0.95\omega_p$.

A feature of this qubit circuit is built-in readout, a property missing from the two previous cases. It is based on the possibility that states in the cubic potential can tunnel through the cubic potential barrier into the continuum outside the barrier. Because the tunneling rate increases by a factor of approximately 500 each time we go from one energy level to the next, the population of the $|1\rangle$ qubit state can be reliably measured by sending a probe signal inducing a transition from the 1 state to a higher energy state with large tunneling probability. After tunneling, the particle representing the phase accelerates down the washboard, a convenient self-amplification process leading to a voltage $2\Delta/e$ across the junction. Therefore, a finite voltage $V \neq 0$ suddenly appearing across the junction just after the probe signal implies that the qubit was in state $|1\rangle$, whereas $V = 0$ implies that the qubit was in state $|0\rangle$.

In practice, like in the two previous cases, the transition frequency $\omega_{01}/2\pi$ falls in the 5-20GHz range. This frequency is only determined by material properties of the barrier, since the product $C_J\,L_J$ does not depend on junction area. The number of levels in the well is typically $\Delta U/\hbar\omega_p \approx 4$.

Setting the bias current at a value I and calling ΔI the variations of the difference $I - I_0$ (originating either in variations of I or I_0), the qubit Hamiltonian is given by

$$H_{qubit} = \hbar\omega_{01}\sigma_Z + \sqrt{\frac{\hbar}{2\omega_{01}C_J}}\Delta I(\sigma_X + \chi\sigma_Z), \tag{6.7}$$

where $\chi = \sqrt{\hbar\omega_{01}/3\Delta U} \simeq 1/4$ for typical operating parameters. In contrast with the flux and phase qubit circuits, the current-biased Josephson junction does not have a bias point where the $0 \rightarrow 1$ transition frequency has a local minimum. The hamiltonian cannot be cast into the NMR-type form of Eq. 6.2. However, a sinusoidal current signal $\Delta I\ (t) \sim \sin\omega_{01}t$ can still produce σ_X rotations, whereas a low-frequency signal produces σ_Z operations [26].

In analogy with the preceding circuits, qubits derived from this circuit and/or having the same phase potential shape and qubit properties have been nicknamed "phase qubits" since the controlled variable is the phase (the X pseudo-spin direction in hamiltonian 6.7).

6.4. Tunability versus sensitivity to noise in control parameters

The reduced two-level hamiltonians Eqs. 6.2,6.4 and 6.7 have been tested thoroughly and are now well-established. They contain the very important parametric dependence of the coefficient of σ_X, which can be viewed on one hand as how much the qubit can be tuned by an external control parameter, and on the other hand as how much it can be dephased by uncontrolled variations in that parameter. It is often important to realize that even if the control parameter has a very stable value at the level of room-temperature electronics, the noise in the electrical components relaying its value at the qubit level might be inducing detrimental fluctuations. An example is the flux through a superconducting loop, which in principle could be set very precisely by a stable current in a coil, and which in practice often fluctuates because of trapped flux motion in the wire of the loop or in nearby superconducting films. Note that, on the other hand, the two-level hamiltonian does not contain the non-linear properties of the qubit, and how they conflict with its intrinsic noise, a problem which we discuss in the next subsection.

6.5. Non-linearity versus sensitivity to intrinsic noise

The three basic quantum circuit types discussed above illustrate a general tendency of Josephson qubits. If we try to make the level structure very non-linear, i.e. $|\omega_{01} - \omega_{12}| \gg \omega_{01}$, we necessarily expose the system sensitively to at least one type of intrinsic noise. The flux qubit is contructed to reach a very large non-linearity, but is also maximally exposed, relatively speaking, to critical current noise and flux noise. On the other hand, the phase qubit starts with a relatively small non-linearity and acquires it at the expense of a precise tuning of the difference between the bias current and the critical current, and therefore exposes itself also to the noise in the latter. The Cooper box, finally, acquires non-linearity at the expense of its sensitivity to offset charge noise. The search for the optimal qubit circuit involves therefore a detailed knowledge of the relative intensities of the various sources of noise, and their variations with all the construction parameters of the qubit, and in particular – this point is crucial – the properties of the materials involved in the tunnel junction fabrication. No such in-depth of knowledge exists at the time of this writing and one can only make educated guesses.

The qubit optimization problem is also further complicated by the necessity to readout quantum information, which we address just after reviewing the relationships between the intensity of noise and the decay rates of quantum information.

7. Qubit relaxation and decoherence

A generic quantum state of a qubit can be represented as a unit vector $\vec{S}$ pointing on a sphere, the so-called Bloch sphere. One distinguishes two broad classes of errors. The first one corresponds to the tip of the Bloch vector diffusing along a meridian, i.e. a great circle passing through the poles (latitude fluctuations). This process is called energy relaxation or state-mixing. The second class corresponds to the tip of the Bloch vector diffusing along a parallel, i.e. a circle perpendicular to the line joining the two poles (longitude fluctuations). This process is called dephasing or decoherence.

In Appendix 2 we define precisely these rates and show that they are directly proportional to the power spectral densities of the noises entering in the parameters of the hamiltonian of the qubit. More precisely, we find that the decoherence rate is proportional to the total spectral density of the quasi-zero-frequency noise in the qubit frequency. The relaxation rate, on the other hand, is proportional to the total spectral density near the qubit frequency of the noise in the field perpendicular to the eigenaxis of the qubit.

In principle, the expressions for the relaxation and decoherence rate could lead to a ranking of the various qubit circuits: from their reduced spin hamiltonian, one can find with what coefficient each basic noise source contributes to the various spectral densities entering in the rates. One could then optimize the various parameters of the qubit to greatly reduce its sensitivity to noise. However, before discussing this question further, we must realize that the readout itself can provide substantial additional noise sources for the qubit. Therefore, the design of a qubit circuit that maximizes the number of coherent gate operations is a subtle optimization problem which must treat in parallel both the intrinsic noises of the qubit and the back-action noise of the readout.

8. Readout of superconducting qubits

8.1. Formulation of the readout problem

We have examined so far the various basic circuits for qubit implementation and their associated methods to write and manipulate quantum information. Another important task quantum circuits must perform is the readout of that information. As we mentioned earlier, the difficulty of the readout problem is to open a coupling channel to the qubit for extracting information without at the same time submitting it to noise.

Ideally, the readout part of the circuit – referred to in the following simply as "readout" – should include both a switch, which defines an "OFF" and an "ON" phase, and a state measurement device. During the OFF phase, where reset and gate operations take place, the measurement device should be completely decoupled from the qubit degrees of freedom. During the ON phase, the measurement device should be maximally coupled to a qubit variable that distinguishes the 0 and the 1 state. However, this condition is not sufficient. The back-action of the measurement device during the ON phase should be weak enough not to relax the qubit [27].

The readout can be characterized by 4 parameters. The first one describes the sensitivity of the measuring device while the next two describes its back-action, factoring in the quality of the switch (see Appendix 3 for their definition):

i) the measurement time τ_m defined as the time taken by the measuring device to reach a signal-to-noise ratio of 1 in the determination of the state.

ii) the energy relaxation time Γ_1^{ON} of the qubit in the ON state.

iii) the coherence decay rate Γ_2^{OFF} of the qubit information in the OFF state.

iv) the dead time t_d needed to reset the measuring device after a qubit measurement. The readout is usually perturbed by the energy expenditure associated with producing a signal strong enough for external detection.

Simultaneously minimizing these parameters to improve readout performance cannot be done without running into conflicts. An important quantity to optimize is the readout fidelity. By construction, at the end of the ON phase, the readout should have reached one of two classical states: 0_c and 1_c, the outcomes of the measurement process. The latter can be described by 2 probabilities: the probability $p_{00_c}(p_{11_c})$ that starting from the qubit state $|0\rangle$ ($|1\rangle$) the measurement yields $0_c(1_c)$. The readout fidelity (or discriminating power) is defined as $F = p_{00c} + p_{11_c} - 1$. For a measuring device with a signal-to-noise ratio increasing like the square of measurement duration τ, we would have, if back-action could be neglected, $F = \mathrm{erf}\left(2^{-1/2}\tau/\tau_m\right)$.

8.2. Requirements and general strategies

The fidelity and speed of the readout, usually not discussed in the context of quantum algorithms because they enter marginally in the evaluation of their complexity, are actually key to experiments studying the coherence properties of qubits and gates. A very fast and sensitive readout will gather at a rapid pace information on the imperfections and drifts of qubit parameters, thereby allowing the experimenter to design fabrication strategies to fight them or even correct them in real time.

We are thus mostly interested in "single-shot" readouts [27], for which F is order unity, as opposed to schemes in which a weak measurement is performed continuously [28]. If $F \ll 1$, of order F^{-2} identical preparation and readout cycles need to be performed to access the state of the qubit. The condition for "single-shot" operation is

$$\Gamma_1^{ON}\tau_m < 1$$

The speed of the readout, determined both by τ_m and t_d, should be sufficiently fast to allow a complete characterization of all the properties of the qubit before any drift in parameters occurs. With sufficient speed, the automatic correction of these drifts in real time using feedback will be possible.

Rapidly pulsing the readout on and off with a large decoupling amplitude such that

$$\Gamma_2^{OFF}T_2 - 1 \ll 1$$

requires a fast, strongly non-linear element, which is provided by one or more auxiliary Josephson junctions. Decoupling the qubit from the readout in the OFF phase requires balancing the circuit in the manner of a Wheatstone bridge, with the readout input variable and the qubit variable corresponding to 2 orthogonal electrical degrees of freedom. Finally, to be as complete as possible even in presence of small asymmetries, the decoupling also requires an impedance mismatch between the qubit and the dissipative degrees of freedom of the readout. In the next subsection, we discuss how these general ideas have been implemented in 2nd generation quantum circuits. The examples we have chosen all involve a readout circuit which is built-in the qubit itself to provide maximal coupling during the ON phase, as well as a decoupling scheme which has proven effective for obtaining long decoherence times.

8.3. Phase qubit: tunneling readout with a DC-SQUID on-chip amplifier.

The simplest example of a readout is provided by a system derived from the phase qubit (See Fig. 10). In the phase qubit, the levels in the cubic potential

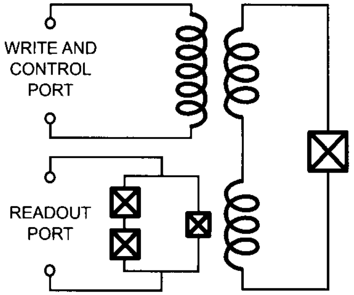

Fig. 10. Phase qubit implemented with a Josephson junction in a high-inductance superconducting loop biased with a flux sufficiently large that the phase across the junction sees a potential analogous to that found for the current-biased junction. The readout part of the circuit is an asymmetric hysteretic SQUID which is completely decoupled from the qubit in the OFF phase. Isolation of the qubit both from the readout and control port is obtained through impedance mismatch of transformers.

are metastable and decay in the continuum, with level $n+1$ having roughly a decay rate Γ_{n+1} 500 times faster than the decay Γ_n of level n. This strong level number dependence of the decay rate leads naturally to the following readout scheme: when readout needs to be performed, a microwave pulse at the transition frequency ω_{12} (or better at ω_{13}) transfers the eventual population of level 1 into level 2, the latter decaying rapidly into the continuum, where it subsequently loses energy by friction and falls into the bottom state of the next corrugation of the potential (because the qubit junction is actually in a superconducting loop of large but finite inductance, the bottom of this next corrugation is in fact the absolute minimum of the potential and the particle representing the system can stay an infinitely long time there). Thus, at the end of the readout pulse, the sytem has either decayed out of the cubic well (readout state 1_c) if the qubit was in the $|1\rangle$ state or remained in the cubic well (readout state 0_c) if the qubit was in the $|0\rangle$ state. The DC-SQUID amplifier is sensitive enough to detect the change in flux accompanying the exit of the cubic well, but the problem is to avoid sending the back-action noise of its stabilizing resistor into the qubit circuit. The solution to this problem involves balancing the SQUID loop in such a way, that for readout state 0_c, the small signal gain of the SQUID is zero, whereas for readout state 1_c, the small signal gain is non-zero [16]. This signal dependent gain is obtained by having 2 junctions in one arm of the SQUID whose total Josephson inductance equals that of the unique junction in the other arm. Finally, a large impedance mismatch between the SQUID and the qubit is obtained by a transformer. The fidelity of such readout is remarkable: 95% has been demonstrated. In Fig. 11, we show the result of a measurement of Rabi oscillations with such qubit+readout.

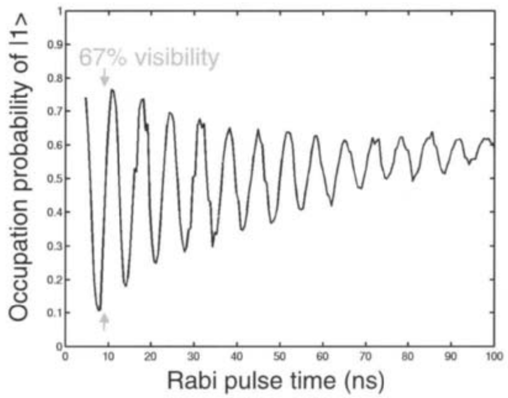

Fig. 11. Rabi oscillations observed for the qubit of Fig. 10.

8.4. Cooper-pair box with non-linear inductive readout: the "Quantronium" circuit

The Cooper-pair box needs to be operated at its "sweet spot" (degeneracy point) where the transition frequency is to first order insensitive to offset charge fluctuations. The "Quantronium" circuit presented in Fig. 12 is a 3-junction bridge configuration with two small junctions defining a Cooper box island, and thus a charge-like qubit which is coupled capacitively to the write and control port (high-impedance port). There is also a large third junction, which provides a non-linear inductive coupling to the read port. When the read port current I is zero, and the flux through the qubit loop is zero, noise coming from the read port is decoupled from the qubit, provided that the two small junctions are identical both in critical current and capacitance. When I is non-zero, the junction bridge is out of balance and the state of the qubit influences the effective non-linear inductance seen from the read port. A further protection of the impedance mismatch type is obtained by a shunt capacitor across the large junction: at the resonance frequency of the non-linear resonator formed by the large junction and the external capacitance C, the differential mode of the circuit involved in the readout presents an impedance of the order of an ohm, a substantial decoupling from the 50Ω transmission line carrying information to the amplifier stage. The readout protocol involves a DC pulse [21, 29] or an RF pulse [30] stimulation of the readout mode. The response is bimodal, each mode corresponding to a state of the qubit. Although the theoretical fidelity of the DC readout can attain 95%, only a maximum of 40% has been obtained so far. The cause of this discrepancy

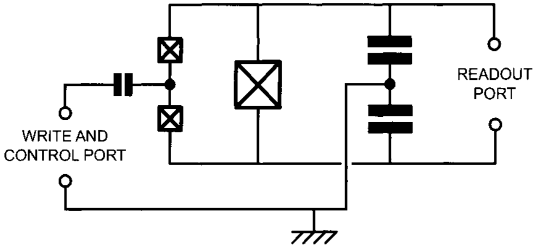

Fig. 12. "Quantronium" circuit consisting of a Cooper pair box with a non-linear inductive readout. A Wheatstone bridge configuration decouples qubit and readout variables when readout is OFF. Impedance mismatch isolation is also provided by additional capacitance in parallel with readout junction.

is still under investigation.

In Fig. 13 we show the result of a Ramsey fringe experiment demonstrating that the coherence quality factor of the quantronium can reach 25 000 at the sweet spot [21]. By studying the degradation of the qubit absorption line and of the Ramsey fringes as one moves away from the sweet spot, it has been possible to show that the residual decoherence is limited by offset charge noise and by flux noise [31]. In principle, the influence of these noises could be further reduced by a better optimization of the qubit design and parameters. In particular, the operation of the box can tolerate ratios of E_J/E_C around 4 where the sensitivity to offset charge is exponentially reduced and where the non-linearity is still of order 15%. The quantronium circuit has so far the best coherence quality factor. We believe this is due to the fact that critical current noise, one dominant intrinsic source of noise, affects this qubit far less than the others, relatively speaking, as can be deduced from the qubit hamiltonians of section 6.

8.5. 3-junction flux qubit with built-in readout

Fig. 14 shows a third example of buit-in readout, this time for a flux-like qubit. The qubit by itself involves 3 junctions in a loop, the larger two of the junctions playing the role of the loop inductance in the basic RF-SQUID [32]. The advantage of this configuration is to reduce the sensitivity of the qubit to external flux variations. The readout part of the circuit involves 2 other junctions forming a hysteretic DC-SQUID whose offset flux depends on the qubit flux state. The critical current of this DC-SQUID has been probed by a DC pulse, but an RF pulse could be applied as in another flux readout. Similarly to the two previous cases, the readout states 1_c and 0_c, which here correspond to the DC-SQUID having switched or not, map very well the qubit states $|1\rangle$ and $|0\rangle$, with a fidelity better than 60%. Here also, a bridge technique orthogonalizes the readout mode, which is the common mode of the DC-SQUID, and the qubit mode, which is coupled to the loop of the DC-SQUID. External capacitors provide additional protection through impedance mismatch. Fig. 15 shows Ramsey fringes obtained with this system.

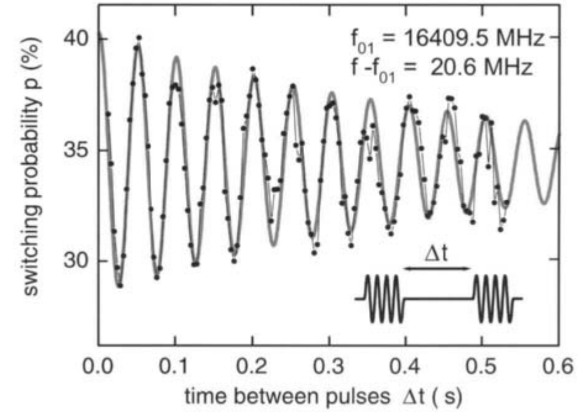

Fig. 13. Measurement of Ramsey fringes for the Quantronium. Two $\pi/2$ pulses separated by a variable delay are applied to the qubit before measurement. The frequency of the pulse is slightly detuned from the transition frequency to provide a stroboscopic measurement of the Larmor precession of the qubit.

8.6. Too much on-chip dissipation can be bad: Do not stir up the dirt!

All the circuits above include an on-chip amplification scheme producing high-level signals which can be read directly by high-temperature low-noise electronics. In the second and third examples, these signals lead to non-equilibrium quasiparticle excitations being produced in the near vicinity of the qubit junctions. An elegant experiment has recently demonstrated that the presence of these excitations increases the offset charge noise [33]. More generally, one can legitimately worry that large energy dissipation on the chip itself will lead to an increase of the noises discussed in section 5.2. A broad class a new readout schemes addresses this question [30, 34, 35]. They are based on a purely dispersive measurement of a qubit susceptibility (capacitive or inductive). A probe signal is sent to the qubit. The signal is coupled to a qubit variable whose average value is identical in the 2 qubit states (for instance, in the capacitive susceptibility, the variable is the island charge in the charge qubit at the degeneracy point). The state-dependent phase

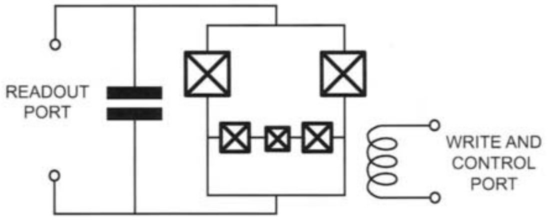

Fig. 14. Three-junction flux qubit with a non-linear inductive readout. The medium-size junctions play the role of an inductor. Bridge configuration for nulling out back-action of readout is also employed here, as well as impedance mismatch provided by additional capacitance.

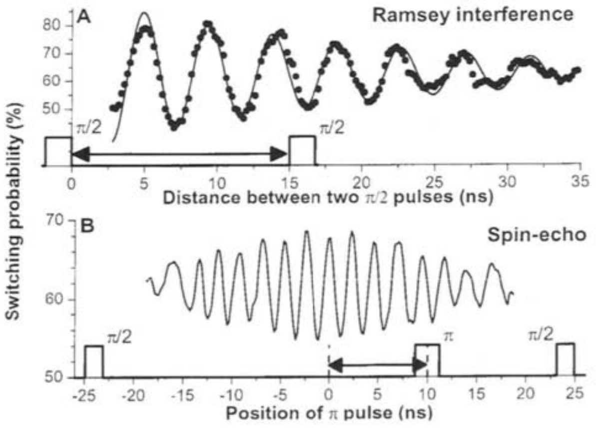

Fig. 15. Panel A: Ramsey fringes obtained for qubit of Fig. 14. Panel B: echo showing the fast dynamics of decoherence processes.

shift of the reflected signal is then amplified by a linear low-temperature amplifier and finally discriminated at high temperature against an adequately chosen threshold. In addition to being very thrifty in terms of energy being dissipated on chip, these new schemes also provide a further natural decoupling action: when the probe signal is off, the back-action of the amplifier is also completely shut off.

9. Coupling superconducting qubits

A priori, 3 types of coupling scheme can be envisioned:

a) In the first type, the transition frequency of the qubits are all equal and the coupling between any pair is switched on using one or several junctions as non-linear elements [36, 37].

b) In the second type, the couplings are fixed, but the transition frequencies of a pair of qubits, originally detuned, are brought on resonance when the coupling between them needs to be turned on [38, 39].

c) In the third type, which bears close resemblance to the methods used in NMR [1], the couplings and the resonance frequencies of the qubits remain fixed, the qubits being always detuned. Being off-diagonal, the coupling elements have negligible action on the qubits. However, when a strong microwave field is applied to the target and control qubits at their mean frequency, they become in "speaking terms" for the exchange of energy quanta and gate action can take place [40].

So far only scheme b) has been tested experimentally.

The advantage of schemes b) and c) is that they work with purely passive reactive elements like capacitors and inductors which should remain very stable as a function of time and which also should present very little high-frequency noise. In a way, we must design quantum integrated circuits in the manner that vacuum tube radios were designed in the 50's: only 6 tubes were used for a complete heterodyne radio set, including the power supply. Nowadays several hundreds of transistors are used in a radio or any hi-fi system. In that ancient era of classical electronics, linear elements like capacitors, inductors or resistors were "free" because they were relatively reliable whereas tubes could break down easily. We have to follow a similar path in quantum integrated circuit, the reliability issues having become noise minimization issues.

10. Can coherence be improved with better materials?

Up to now, we have discussed how, given the power spectral densities of the noises ΔQ_r, ΔE_C and ΔE_J, we could design a qubit equipped with control, readout and coupling circuits. It is worthwhile to ask at this point if we could improve the material properties to gain in the coherence of the qubit, assuming all other problems like noise in the control channels and the back-action of the readout have been solved. A model put forward by one of us (JMM) and collaborators shed some light on the direction one would follow to answer this question. The $1/f$ spectrum of the materials noises suggests that they all originate from 2-level fluctuators in the amorphous alumina tunnel layer of the junction itself, or its close vicinity. The substrate or the surface of the superconducting films are also suspect in the case of ΔQ_r and ΔE_C but their influence would be relatively weaker and we ignore them for simplicity. These two-level systems are supposed to be randomly distributed positional degrees of freedom ξ_i with effective spin-1/2 properties, for instance an impurity atom tunneling between two adjacent potential wells. Each two-level system is in principle characterized by 3 parameters: the energy splitting $\hbar\omega_i$, and the two coefficients α_i and β_i of the Pauli matrix representation of $\xi_i = \alpha_i \sigma_{iz} + \beta_i \sigma_{ix}$. The random nature of the problem leads us to suppose that α_i and β_i are both Gaussian random variables with the same standard deviation ρ_i. By carrying a charge, the thermal and quantum motion of ξ_i can contribute to $\Delta Q_r = \sum_i q_i \xi_i$ and $\Delta E_C = \sum_i c_i \frac{\beta_i^2}{\omega_i} \sigma_{iz}$. Likewise, by modifying the transmission of a tunneling channel in its vicinity, the motion of ξ_i can contribute to $\Delta E_J = \sum_i g_i \xi_i$. We can further suppose that the quality of the material of the junction is simply characterized by a few numbers. The essential one is the density ν of the transition frequencies ω_i in frequency space and in real space, assuming a ω^{-1} distribution (this is necessary to explain the $1/f$ behavior) and a uniform spatial distribution on the surface of the junction. Recent experiments indicate that the parameter ν is of order$10^5 \mu\mathrm{m}^{-2}(\mathrm{decade})^{-1}$. Then, assuming a universal ρ independent of frequency, only one coefficient is needed per noise, namely, the average modulation efficiency of each fluctuator. Such analysis provides a common language for describing various experiments probing the dependence of decoherence on the material of the junction. Once the influence of the junction fabrication parameters (oxydation pressure and temperature, impurity contents, and so on) on these noise intensities will be known, it will be possible to devise optimized fabrication procedures, in the same way perhaps as the $1/f$ noise in C-MOS transistors has been reduced by careful material studies.

11. Concluding remarks and perspectives

The logical thread through this review of superconducting qubits has been the question "What is the best qubit design?". We unfortunately cannot, at present, conclude by giving a definitive answer to this complex optimisation problem.

Yet, a lot has already been achieved, and superconducting qubits are becoming serious competitors of trapped ions and atoms. The following properties of quantum circuits have been demonstrated:

a) Coherence quality factors $Q_\varphi = T_\varphi \omega_{01}$ can attain at least 2.10^4
b) Readout and reset fidelity can be greater than 95%
c) All states on the Bloch sphere can be addressed
d) Spin echo techniques can null out low frequency drift of offset charges
e) Two qubits can be coupled and RF pulses can implement gate operation
f) A qubit can be fabricated using only optical lithography techniques

The major problem we are facing is that these various results have not been obtained at the same time IN THE SAME CIRCUIT, although succesful design elements in one have often been incorporated into the next generation of others. The complete optimization of the single qubit+readout has not been achieved yet. However, we have presented in this review the elements of a systematic methodology resolving the various conflicts that are generated by all the different requirements. Our opinion is that, once noise sources are better characterized, an appropriate combination of all the known circuit design strategies for improving coherence, as well as the understanding of optimal tunnel layer growth conditions for lowering the intrinsic noise of Josephson junctions, should lead us to reach the 1-qubit and 2-qubit coherence levels needed for error correction [43]. Along the way, good medium term targets to test overall progress on the simultaneous fronts of qubit coherence, readout and gate coupling are the measurement of Bell 's inequality violation or the implementation of the Deutsch-Josza algorithm, both of which requiring the simultaneous satisfaction of properties a)-e).

Acknowledgements

The authors have greatly benefited from discussions with I. Chuang, D. Esteve, S. Girvin, S. Lloyd, H. Mooij, R. Schoelkopf, I. Siddiqi, C. Urbina and D. Vion. They would like also to thank the participants of the Les Houches Summer School on Quantum Information Processing and Entanglement held in 2003 for useful exchanges. Finally, funding from ARDA/ARO and the Keck Fundation is gratefully acknowledged.

12. Appendix1: Quantum circuit theory

The problem we are addressing in this section is, given a superconducting circuit made up of capacitors, inductors and Josephson junctions, how to systematically write its quantum hamiltonian, the generating function from which the quantum dynamics of the circuit can be obtained. This problem has been considered first by Yurke and Denker [44] in a seminal paper and analyzed in further details by Devoret [45]. We will only summarize here the results needed for this review.

The circuit is given as a set of branches, which can be capacitors, inductors or Josephson tunnel elements, connected at nodes. Several independent paths formed by a succession of branches can be found between nodes. The circuit can therefore contain one or several loops. It is important to note that a circuit has not one hamiltonian but many, each one depending on a particular representation. We are describing here one particular type of representation, which is usually well adapted to circuits containing Josephson junctions. Like in classical circuit theory, a set of independent current and voltages has to be found for a particular representation. We start by associating to each branch b of the circuit, the current i_b flowing through it and the voltage v_b across it (a convention has to be made first on the direction of the branches). Kirchhoff's laws impose relations among branch variables and some of them are redundant. The following procedure is used to eliminate redundant branches: one node of the circuit is first chosen as ground. Then from the ground, a loop-free set of branches called spanning tree is selected. The rule behind the selection of the spanning tree is the following: each node of the circuit must be linked to the ground by one and only one path belonging to the tree. In general, inductors (linear or non-linear) are preferred as branches of the tree but this is not necessary. Once the spanning tree is chosen (note that we still have many possibilities for this tree), we can associate to each node a "node voltage" v_n which is the algebraic sum of the voltages along the branches between ground and the node. The conjugate "node current" i_n is the algebraic sum of all currents flowing to the node through capacitors ONLY. The dynamical variables appearing in the hamiltonian of the circuit are the node fluxes and node charges defined as

$$\begin{aligned} \phi_n &= \int_{-\infty}^{t} v(t_1)\,dt_1 \\ q_n &= \int_{-\infty}^{t} i(t_1)\,dt_1 \end{aligned}$$

Using Kirchhoff's laws, it is possible to express the flux and the charge of each branch as a linear combination of all the node fluxes and charges, respectively. In this inversion procedure, the total flux through loops imposed by external flux bias sources and polarisation charges of nodes imposed by charge bias sources, appear.

If we now sum the energies of all branches of the circuit expressed in terms of node flux and charges, we will obtain the hamiltonian of the circuit corresponding to the representation associated with the particular spanning tree. In this hamiltonian, capacitor energies behave like kinetic terms while the inductor energies behave as potential terms. The hamiltonian of the LC circuit written in section 2 is an elementary example of this procedure.

Once the hamiltonian is obtained it is easy get its quantum version by replacing all the node fluxes and charges by their quantum operator equivalent. The flux and charge of a node have a commutator given by $i\hbar$, like the position and momentum of a particle:

$$\begin{aligned} \phi &\to \hat{\phi} \\ q &\to \hat{q} \\ \left[\hat{\phi}, \hat{q}\right] &= i\hbar \end{aligned}$$

One can also show that the flux and charge operators corresponding to a branch share the same commutation relation. Note that for the special case of the Josephson element, the phase $\hat{\theta}$ and Cooper pair number $\hat{N}$, which are its dimensionless electric variables, have the property:

$$\left[\hat{\theta}, \hat{N}\right] = i$$

In the so-called charge basis, we have

$$\begin{aligned} \hat{N} &= \sum_N N \left|N\right\rangle \left\langle N\right| \\ \cos\hat{\theta} &= \frac{1}{2}\sum_N \left(\left|N\right\rangle \left\langle N+1\right| + \left|N+\right\rangle \left\langle N\right|\right) \end{aligned}$$

while in the so-called phase basis, we have

$$\hat{N} = \left|\theta\right\rangle \frac{\partial}{i\partial} \left\langle\theta\right|$$

Note that since the Cooper pair number $\hat{N}$ is an operator with integer eigenvalues, its conjugate variable $\hat{\theta}$, has eigenvalues behaving like angles, i.e. they are defined only modulo 2π.

In this review, outside this appendix, we have dropped the hat on operators for simplicity.

13. Appendix 2: Eigenenergies and eigenfunctions of the Cooper pair box

From Appendix 1, it easy to see that the hamiltonian of the Cooper pair box leads to the Schrodinger equation

$$\left[E_C\left(\frac{\partial}{i\partial\theta}-N_g\right)^2-E_J\cos\theta\right]\Psi_k(\theta)=E_k\Psi_k(\theta)$$

The functions $\Psi_k(\theta)\,\mathrm{e}^{-iN_g}$ and energies E_k are solutions of the Mathieu equation and can be found with arbitrary precision for all values of the parameters N_g and E_J/E_C [46]. For instance, using the program Mathematica, we find

$$\begin{aligned}
E_k &= E_C\mathcal{M}_A\left[k+1-(k+1)\bmod 2+2N_g(-1)^k,\,-2E_J/E_C\right]\\
\Psi_k(\theta) &= \frac{e^{iN_g\theta}}{\sqrt{2\pi}}\left\{\mathcal{M}_C\left[\frac{4E_k}{E_C},\frac{-2E_J}{E_C},\frac{\theta}{2}\right]\right.\\
&\quad\left.+i(-1)^{k+1}\mathcal{M}_S\left[\frac{4E_k}{E_C},\frac{-2E_J}{E_C},\frac{\theta}{2}\right]\right\}
\end{aligned}$$

where $\mathcal{M}_A(r,q)=$ `MathieuCharacteristicA[r,q]`,
$\mathcal{M}_C(a,q,z)=$ `MathieuC[a,q,z]`,
$\mathcal{M}_S(a,q,z)=$ `MathieuS[a,q,z]`.

14. Appendix 3: Relaxation and decoherence rates for a qubit

Definition of the rates

We start by introducing the spin eigenreference frame $\hat{z}$, $\hat{x}$ and $\hat{y}$ consisting of the unit vector along the eigenaxis and the associated orthogonal unit vectors ($\hat{x}$ is in the XZ plane). For instance, for the Cooper pair box, we find that $\hat{z}=\cos\alpha\hat{Z}+\sin\alpha\hat{X}$, with $\tan\alpha=2E_C\left(N_g-1/2\right)/E_J$, while $\hat{x}=-\sin\alpha\hat{Z}+\cos\alpha\hat{X}$.

Starting with $\vec{S}$ pointing along $\hat{x}$ at time $t=0$, the dynamics of the Bloch vector in absence of relaxation or decoherence is

$$\vec{S}_0(t)=\cos(\omega_{01})\,\hat{x}+\sin(\omega_{01})\,\hat{y}$$

In presence of relaxation and decoherence, the Bloch vector will deviate from $\vec{S}_0(t)$ and will reach eventually the equilibrium value $S_z^{eq}\hat{z}$, where $S_z^{eq}=\tanh\frac{\hbar\omega_{01}}{2k_BT}$. We define the relaxation and decoherence rates as

$$\begin{aligned}
\Gamma_1 &= \lim_{t\to\infty}\frac{\ln\left\langle S_z(t)-S_z^{eq}\right\rangle}{t}\\
\Gamma_\phi &= \lim_{t\to\infty}\frac{\ln\left[\frac{\left\langle\vec{S}(t).\vec{S}_0(t)\right\rangle}{\left|\vec{S}(t)-S_z^{eq}\hat{z}\right|}\right]}{t}
\end{aligned}$$

Note that these rates have both a useful and rigorous meaning only if the evolution of the components of the average Bloch vector follows, after a negligibly short settling time, an exponential decay. The Γ_1 and Γ_ϕ rates are related to the NMR spin relaxation times T_1 and T_2 [47] by

$$\begin{aligned}
T_1 &= \Gamma_1^{-1}\\
T_2 &= \left(\Gamma_\phi+\Gamma_1/2\right)^{-1}
\end{aligned}$$

The T_2 time can be seen as the net decay time of quantum information, including the influence of both relaxation and dephasing processes. In our discussion of superconducting qubits, we must separate the contribution of the two type of processes since their physical origin is in general very different and cannot rely on the T_2 time alone.

Expressions for the rates

The relaxation process can be seen as resulting from unwanted transitions between the two eigenstate of the qubit induced by fluctuations in the effective fields along the x and y axes. Introducing the power spectral density of this field, one can demonstrate from Fermi's Golden Rule that, for perturbative fluctuations,

$$\Gamma_1=\frac{S_x(\omega_{01})+S_y(\omega_{01})}{\hbar^2}$$

Taking the case of the Cooper pair box as an example, we find that $S_y(\omega_{01})=0$ and that

$$S_x(\omega)=\int_{-\infty}^{+\infty}dte^{i\omega t}\left\langle A(t)\,A(0)\right\rangle+\left\langle B(t)\,B(0)\right\rangle$$

where

$$\begin{aligned} A(t) &= \frac{\Delta E_J(t)\, E_{el}}{2\sqrt{E_J^2+E_{el}^2}} \\ B(t) &= \frac{E_J\, \Delta E_{el}(t)}{2\sqrt{E_J^2+E_{el}^2}} \\ E_{el} &= 2E_C\left(N_g-1/2\right) \end{aligned}$$

Since the fluctuations $\Delta E_{el}(t)$ can be related to the impedance of the environment of the box [18,20,48], an order of magnitude estimate of the relaxation rate can be performed, and is in rough agreement with observations [21,49].

The decoherence process, on the other hand, is induced by fluctuations in the effective field along the eigenaxis z. If these fluctuations are Gaussian, with a white noise spectral density up to frequencies of order several Γ_ϕ (which is often not the case because of the presence of 1/f noise) we have

$$\Gamma_\phi = \frac{S_z(\omega \simeq 0)}{\hbar^2}$$

In presence of a low frequency noise with an 1/f behavior, the formula is more complicated [50]. If the environment producing the low frequency noise consists of many degrees of freedom, each of which is very weakly coupled to the qubit, then one is in presence of classical dephasing which, if slow enough, can in principle be fought using echo techniques. If, one the other hand, only a few degrees of freedom like magnetic spins or glassy two-level systems are dominating the low frequency dynamics, dephasing is quantum and not correctable, unless the transition frequencies of these few perturbing degrees of freedom is itself very stable.

References

[1] M. A. Nielsen and I. L. Chuang, *Quantum Computation and Quantum Information* (Cambridge, 2000).

[2] M. Tinkham, *Introduction to Superconductivity* (Krieger, Malabar, 1985).

[3] J.M. Martinis, M.H. Devoret, J. Clarke, Phys. Rev. Lett. 55, 1543-1546 (1985); M.H. Devoret, J.M. Martinis, J. Clarke, Phys. Rev. Lett. 55, 1908-1911 (1985); J. M. Martinis, M.H. Devoret and J. Clarke, Phys. Rev. 35, 4682 (1987).

[4] J.M. Martinis and M. Nahum, Phys Rev. B48, 18316-19 (1993).

[5] B.D. Josephson, in *Superconductivity*, R.D. Parks, ed. (Marcel Dekker, New York, 1969).

[6] I. Giaever, Phys. Rev. Lett. 5, 147, 464 (1960)

[7] A.O. Caldeira and A.J. Leggett, Ann. Phys. (NY) 149, 347-456 (1983); A.J. Leggett, J. Phys. CM 14, R415-451 (2002).

[8] D. P. DiVincenzo, arXiv:quant-ph/0002077,

[9] R. P. Feynman, *Lectures on Physics* (Addison-Wesley, Reading, 1964) Vol. 2, Chap. 23.

[10] D.C. Mattis and J. Bardeen, Phys. Rev. 111, 412 (1958)

[11] P.G. de Gennes, *Superconductivity of Metals and Alloys* (Benjamin, New York, 1966)

[12] J.M. Raimond, M. Brune and S. Haroche, Rev. Mod. Phys. 73, 565 (2001).

[13] J.M. Martinis and K. Osborne, in *Quantum Information and Entanglement*, Eds. J.M. Raimond, D. Esteve and J. Dalibard, Les Houches Summer School Series, arXiv:cond-mat/0402430

[14] J. Clarke, Proc. IEEE 77, 1208 (1989)

[15] D. J. Van Harlingen, B.L.T. Plourde, T.L. Robertson, P.A. Reichardt, and John Clarke, preprint

[16] R. W. Simmonds, K. M. Lang, D. A. Hite, D. P. Pappas, and J. M. Martinis, submitted to Phys. Rev. Lett.

[17] M. Büttiker, Phys. Rev. B36, 3548 (1987).

[18] V. Bouchiat, D. Vion, P. Joyez, D. Esteve, M.H. Devoret, Physica Scripta T76 (1998) p.165-70.

[19] Y. Nakamura , Yu. A Pashkin, and J. S. Tsai, Nature 398, 786 (1999).

[20] Yu. Makhlin, G. Schön, and A. Shnirman, Rev. Mod. Phys. 73, 357-400 (2001).

[21] D. Vion, A. Aassime, A. Cottet, P. Joyez, H. Pothier, C. Urbina, D. Esteve, and M.H. Devoret, Science 296 (2002), p. 286-9.

[22] A. Barone and G. Paternò, *Physics and Applications of the Josephson Effect* (Wiley, New York, 1992)

[23] S. Han, R. Rouse and J.E. Lukens, Phys. Rev. Lett. 84, 1300 (2000); J.R. Friedman, V. Patel, W. Chen, S.K. Tolpygo and J.E. Lukens, Nature 406, 43 (2000).

[24] J.E. Mooij, T.P. Orlando, L. Levitov, Lin Tian, C.H. van der Wal and S. Lloyd, Science 285, 1036 (1999); C.H. van der Wal, A.C.J. ter Haar, F.K. Wilhem, R.N. Schouten, C. Harmans, T.P. Orlando, S. Loyd and J.E. Mooij, Science 290, 773 (2000).

[25] J. M. Martinis, S. Nam, J. Aumentado, and C. Urbina, Phys. Rev. Lett. 89, 117901 (2002)

[26] M. Steffen, J. Martinis and I.L. Chuang, PRB 68, 224518 (2003).

[27] M.H. Devoret and R.J. Schoelkopf, Nature, 406, 1039 (2002).

[28] A.N. Korotkov, D.V. Averin, arXiv:cond-mat/0002203

[29] A. Cottet, D. Vion, A. Aassime, P. Joyez, D. Esteve, and M.H Devoret, Physica C 367, 197 (2002)

[30] I. Siddiqi, R. Vijay, F. Pierre, C.M. Wilson, M. Metcalfe, C. Rigetti, L. Frunzio and M. Devoret, submitted.

[31] D. Vion, A. Aassime, A. Cottet, P. Joyez, H. Pothier, C. Urbina, D. Esteve, and M.H. Devoret, Fortschritte der Physik, 51,

[32] I. Chiorescu, Y. Nakamura, C. J. P. M. Harmans, and J. E. Mooij, Science 299, p. 1869 (2003).

[33] J. Mannik and J.E. Lukens, arXiv:cond-mat/0305190 v2

[34] A. Blais, Ren-Shou Huang, A. Wallraff, S. M. Girvin, R. J. Schoelkopf, arXiv:cond-mat/0402216

[35] A. Lupascu, C. J. M. Verwijs, R. N. Schouten, C. J. P. M. Harmans, J. E. Mooij, submitted.

[36] Variable electrostatic transformer: controllable coupling of two charge qubits, D.V. Averin, C. Bruder, Phys. Rev. Lett. 91, 057003 (2003).

[37] A. Blais, A. Maassen van den Brink, A. M. Zagoskin, Phys. Rev. Lett. 90, 127901 (2003)

[38] Pashkin Yu. A., Yamamoto T., Astafiev O., Nakamura Y., Averin D.V., and Tsai J. S.:"Quantum oscillation in two coupled charge qubit", Nature 421 (2003).

[39] J. B. Majer, F.G. Paauw, A.C.J. ter Haar, C.J.P.M. Harmans, J.E. Mooij, arXiv:cond-mat/0308192.

[40] C. Rigetti and M. Devoret, unpublished

[41] Nakamura Y., Pashkin Yu. A., and Tsai J. S., Phys. Rev. Lett. 88, 047901 (2002).

[42] D. Vion, A. Aassime, A. Cottet, P. Joyez, H. Pothier, C. Urbina, D. Esteve, and M.H. Devoret, Forts. der Physik, 51, 462 (2003).

[43] J. Preskill, J. Proc. R. Soc. London Ser. A454, 385 (1998).

[44] B. Yurke and J.S. Denker, Phys. Rev. A 29 (1984) 1419.

[45] M.H. Devoret in *"Quantum Fluctuations"*, S. Reynaud, E. Giacobino, J. Zinn-Justin, eds. (Elsevier, Amsterdam, 1996) p. 351

[46] A. Cottet, *Implementation of a quantum bit in a superconducting circuit,* PhD Thesis, Université Paris 6, 2002

[47] A. Abragam, Principles of Nuclear Magnetic Resonance (Oxford University Press, Oxford, 1985).

[48] R. J. Schoelkopf, A. A. Clerk, S. M. Girvin, K. W. Lehnert, M. H. Devoret. arXiv:cond-mat/0210247.

[49] K.W. Lehnert, K. Bladh, L.F. Spietz, D. Gunnarsson, D.I. Schuster, P. Delsing, and R.J. Schoelkopf, Phys. Rev.Lett., 90, 027002 (2002).

[50] J.M. Martinis, S. Nam, J. Aumentado, K.M. Lang, and C. Urbina, Phys. Rev. B67, 462 (2003).

Course 13

SUPERCONDUCTING QUBITS AND THE PHYSICS OF JOSEPHSON JUNCTIONS

John M. Martinis

National Institute of Standards and Technology, 325 Broadway, Boulder, CO 80305-3328, USA

D. Estève, J.-M. Raimond and J. Dalibard, eds.
Les Houches, Session LXXIX, 2003
Quantum Entanglement and Information Processing
Intrication quantique et traitement de l'information

Contents

1. Introduction

Josephson junctions are good candidates for the construction of quantum bits (qubits) for a quantum computer[1]. This system is attractive because the low dissipation inherent to superconductors make possible, in principle, long coherence times. In addition, because complex superconducting circuits can be microfabricated using integrated-circuit processing techniques, scaling to a large number of qubits should be relatively straightforward. Given the initial success of several types of Josephson qubits[2, 3, 4, 5, 6, 7, 9, 8, 10], a question naturally arises: what are the essential components that must be tested, understood, and improved for eventual construction of a Josephson quantum computer?

In this paper we focus on the physics of the Josephson junction because, being nonlinear, it is the fundamental circuit element that is needed for the appearance of usable qubit states. In contrast, *linear* circuit elements such as capacitors and inductors can form low-dissipation superconducting resonators, but are unusable for qubits because the energy-level spacings are degenerate. The nonlinearity of the Josephson inductance breaks the degeneracy of the energy level spacings, allowing dynamics of the system to be restricted to only the two qubit states. The Josephson junction is a remarkable nonlinear element because it combines negligible dissipation with extremely large nonlinearity - the change of the qubit state by only one photon in energy can modify the junction inductance by order unity!

Most theoretical and experimental investigations with Josephson qubits assume perfect junction behavior. Is such an assumption valid? Recent experiments by our group indicate that coherence is limited by microwave-frequency fluctuations in the critical current of the junction[10]. A deeper understanding of the junction physics is thus needed so that nonideal behavior can be more readily identified, understood, and eliminated. Although we will not discuss specific imperfections of junctions in this paper, we want to describe a clear and precise model of the Josephson junction that can give an intuitive understanding of the Josephson effect. This is especially needed since textbooks do not typically derive the Josephson effect from a microscopic viewpoint. As standard calculations use only perturbation theory, we will also need to introduce an exact description of the Josephson effect via the mesoscopic theory of quasiparticle bound-states.

The outline of the paper is as follows. We first describe in Sec. 2 the nonlinear Josephson inductance. In Sec. 3 we discuss the three types of qubit circuits, and show how these circuits use this nonlinearity in unique manners. We then give a brief derivation of the BCS theory in Sec. 4, highlighting the appearance of the macroscopic phase parameter. The Josephson equations are derived in Sec. 5 using standard first and second order perturbation theory that describe quasiparticle and Cooper-pair tunneling. An exact calculation of the Josephson effect then follows in Sec. 6 using the quasiparticle bound-state theory. Section 7 expands upon this theory and describes quasiparticle excitations as transitions from the ground to excited bound states from nonadiabatic changes in the bias. Although quasiparticle current is typically calculated only for a constant DC voltage, the advantage to this approach is seen in Sec. 8, where we qualitatively describe quasiparticle tunneling with AC voltage excitations, as appropriate for the qubit state. This section describes how the Josephson qubit is typically insensitive to quasiparticle damping, even to the extent that a phase qubit can be constructed from microbridge junctions.

2. The nonlinear Josephson inductance

A Josephson tunnel junction is formed by separating two superconducting electrodes with an insulator thin enough so that electrons can quantum-mechanically tunnel through the barrier, as illustrated in Fig. 1 . The Josephson effect describes the supercurrent I_J that flows through the junction according to the classical equations

$$I_J = I_0 \sin\delta \tag{2.1a}$$

$$V = \frac{\Phi_0}{2\pi}\frac{d\delta}{dt}\,, \tag{2.1b}$$

where $\Phi_0 = h/2e$ is the superconducting flux quantum, I_0 is the critical-current parameter of the junction, and $\delta = \phi_L - \phi_R$ and V are respectively the superconducting phase difference and voltage across the junction. The dynamical behavior of these two equations can be understood by first differentiating Eq. 2.1a and replacing $d\delta/dt$ with V according to Eq. 2.1b

$$\frac{dI_J}{dt} = I_0 \cos\delta\,\frac{2\pi}{\Phi_0}V\,. \tag{2.2}$$

With dI_J/dt proportional to V, this equation describes an inductor. By defining a Josephson inductance L_J according to the conventional definition $V = L_J dI_J/dt$, one finds

$$L_J = \frac{\Phi_0}{2\pi I_0 \cos\delta}\,. \tag{2.3a}$$

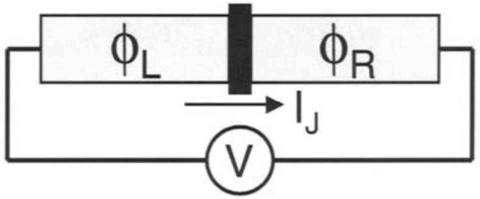

Fig. 1. Schematic diagram of a Josephson junction connected to a bias voltage V. The Josephson current is given by $I_J = I_0 \sin\delta$, where $\delta = \phi_L - \phi_R$ is the difference in the superconducting phase across the junction.

The $1/\cos\delta$ term reveals that this inductance is nonlinear. It becomes large as $\delta \to \pi/2$, and is negative for $\pi/2 < \delta < 3\pi/2$. The inductance at zero bias is $L_{J0} = \Phi_0/2\pi I_0$.

An inductance describes an energy-conserving circuit element. The energy stored in the junction is given by

$$U_J = \int I_J V dt \tag{2.4a}$$

$$= \int I_0 \sin\delta \, \frac{\Phi_0}{2\pi}\frac{d\delta}{dt} dt \tag{2.4b}$$

$$= \frac{I_0\Phi_0}{2\pi}\int \sin\delta \, d\delta \tag{2.4c}$$

$$= -\frac{I_0\Phi_0}{2\pi}\cos\delta \,. \tag{2.4d}$$

This calculation of energy can be generalized for other nondissipative circuit elements. For example, a similar calculation for a current bias gives $U_{\mathrm{bias}} = -(I\Phi_0/2\pi)\delta$. Conversely, if a circuit element has an energy $U(\delta)$, then the current-phase relationship of the element, analogous to Eq. 2.1a, is

$$I_J(\delta) = \frac{2\pi}{\Phi_0}\frac{\partial U(\delta)}{\partial\delta} \,. \tag{2.5}$$

A generalized Josephson inductance can be also be found from the second derivative of U ,

$$\frac{1}{L_J} = \left(\frac{2\pi}{\Phi_0}\right)^2 \frac{\partial^2 U(\delta)}{\partial\delta^2} \,. \tag{2.6}$$

The classical and quantum behavior of a particular circuit is described by a Hamiltonian, which of course depends on the exact circuit configuration. The procedure for writing down a Hamiltonian for an arbitrary circuit has been described in detail in a prior publication[11]. The general form of the Hamiltonian for the Josephson effect is $H_J = U_J$.

3. Phase, flux, and charge qubits

A Josephson qubit can be understood as a nonlinear resonator formed from the Josephson inductance and its junction capacitance. nonlinearity is crucial because the system has many energy levels, but the operating space of the qubit must be restricted to only the two lowest states. The system is effectively a two-state system[12] only if the frequency ω_{10} that drives transitions between the qubit states $0 \longleftrightarrow 1$ is different from the frequency ω_{21} for transitions $1 \longleftrightarrow 2$.

We review here three different ways that these nonlinear resonators can be made, and which are named as phase, flux, or charge qubits.

The circuit for the phase-qubit circuit is drawn in Fig. 2(a). Its Hamiltonian is

$$H = \frac{1}{2C}\widehat{Q}^2 - \frac{I_0\Phi_0}{2\pi}\cos\widehat{\delta} - \frac{I\Phi_0}{2\pi}\widehat{\delta} \,, \tag{3.1}$$

where C is the capacitance of the tunnel junction. A similar circuit is drawn for the flux-qubit circuit in Fig. 2(b), and its Hamiltonian is

$$H = \frac{1}{2C}\widehat{Q}^2 - \frac{I_0\Phi_0}{2\pi}\cos\widehat{\delta} + \frac{1}{2L}(\Phi - \frac{\Phi_0}{2\pi}\widehat{\delta})^2 \,. \tag{3.2}$$

The charge qubit has a Hamiltonian similar to that in Eq. 3.1, and is described elsewhere in this publication. Here we have explicitly used notation appropriate for a quantum description, with operators charge $\widehat{Q}$ and phase difference $\widehat{\delta}$ that obey a commutation relationship $[\widehat{\delta}, \widehat{Q}] = 2ei$. Note that the phase and flux qubit Hamiltonians are equivalent for $L \to \infty$ and $I = \Phi/L$, which corresponds to a current bias created from an inductor with infinite impedance.

The commutation relationship between $\widehat{\delta}$ and $\widehat{Q}$ imply that these quantities must be described by a wavefunction. The characteristic widths of this wavefunction are controlled by the energy scales of the system, the charging energy of the junction $E_C = e^2/2C$ and the Josephson energy $E_J = I_0\Phi_0/2\pi$. When the energy of the junction dominates, $E_J \gg E_C$, then $\widehat{\delta}$ can almost be described classically and the width of its wavefunction is small $\langle\widehat{\delta}^2 - \langle\widehat{\delta}\rangle^2\rangle \ll 1$. In contrast, the uncertainty in charge is large $\langle\widehat{Q}^2 - \langle\widehat{Q}\rangle^2\rangle \gg (2e)^2$.

If the Josephson inductance is constant over the width of the $\widehat{\delta}$ wavefunction, then a circuit is well described as a L_J-C harmonic oscillator, and the qubit states

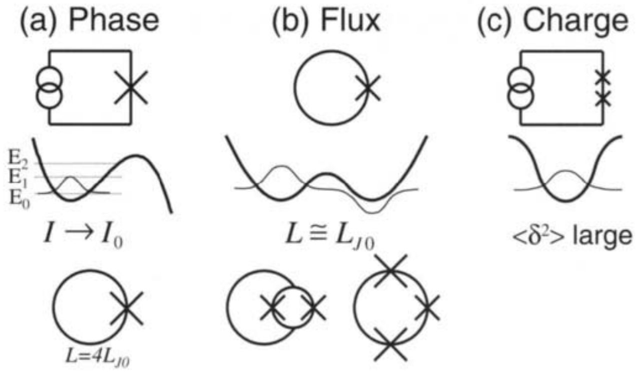

Fig. 2. Comparison of the phase (a), flux (b), and charge (c) qubits. Top row illustrates the circuits, with each "X" symbol representing a Josephson juncton. Middle row has a plot of the Hamiltonian potential (thick line), showing qualitatively different shapes for three qubit types. Ground-state wavefunction is also indicated (thin line). Key circuit parameters are listed in next row. Lowest row indicates variations on the basic circuit, as discussed in text. The lowest three energy levels are illustrated for the phase qubit (dotted lines).

are degenerate and not usable. Usable states are created only when the Josephson inductance changes over the δ-wavefunction.

The most straightforward way for the wavefunction to be affected by the Josephson nonlinearity is for $\widehat{\delta}$ to have a large width , which occurs when $E_J \sim E_C$. A practical implementation of this circuit is illustrated in Fig 2(c), where a double-junction Coulomb blockade device is used instead of a single junction to isolate dissipation from the leads[2, 4]. Because the wavefunction extends over most of the -cos $\widehat{\delta}$ Hamiltonian, the transition frequency ω_{10} can differ from ω_{21} by more than 10 %, creating usable qubit states[13].

Josephson qubits are possible even when $E_J \gg E_C$, provided that the junction is biased to take advantage of its strong nonlinearity. A good example is the phase qubit[6], where typically $E_J \sim 10^4 E_C$, but which is biased near $\delta \lesssim \pi/2$ so that the inductance changes rapidly with δ (see Eq. 2.3a). Under these conditions the potential can be accurately described by a cubic potential, with the barrier height $\Delta U \rightarrow 0$ as $I \rightarrow I_0$. Typically the bias current is adjusted so that the number of energy levels in the well is $\sim 3-5$, which causes ω_{10} to differ from ω_{21} by an acceptably large amount ~ 5 %.

Implementing the phase qubit is challenging because a current bias is required with large impedance. This impedance requirement can be met by biasing the junction with flux through a superconducting loop with a large loop inductance L, as discussed previously and drawn in Fig. 2(a). To form multiple stable flux states and a cubic potential, the loop inductance L must be chosen such that $L \gtrsim 2L_{J0}$. We have found that a design with $L \simeq 4.5L_{J0}$ is a good choice since the potential well then contains the desired cubic potential and only one flux state into which the system can tunnel, simplifying operation.

The flux qubit is designed with $L \lesssim L_{J0}$ and biased in flux so that $\langle\widehat{\delta}\rangle = \pi$. Under these conditions the Josephson inductance is negative and is almost canceled out by L. The small net negative inductance near $\widehat{\delta} = \pi$ turns positive away from this value because of the $1/\cos\delta$ nonlinearity, so that the final potential shape is quartic, as shown in Fig. 2(b). An advantage of the flux qubit is a large net nonlinearity, so that ω_{10} can differ from ω_{21} by over 100 %.

The need to closely tune L with L_{J0} has inspired the invention of several variations to the simple flux-qubit circuit, as illustrated in Fig. 2(b). One method is to use small area junctions[7] with $E_J \sim 10E_C$, producing a large width in the $\widehat{\delta}$ wavefunction and relaxing the requirement of close tuning of L with L_{J0}. Another method is to make the qubit junction a two-junction SQUID, whose critical current can then be tuned via a second flux-bias circuit[14, 15]. Larger junctions are then permissible, with $E_J \sim 10^2 E_C$ to $10^3 E_C$. A third method is to fabricate the loop inductance from two or more larger critical-current junctions[16]. These junctions are biased with phase less than $\pi/2$, and thus act as positive inductors. The advantage to this approach is that junction inductors are smaller than physical inductors, and fabrication imperfections in the critical currents of the junctions tend to cancel out and make the tuning of L with L_{J0} easier.

In summary, the major difference between the phase, flux, and charge qubits is the shape of their nonlinear potentials, which are respectively cubic, quartic, and cosine. It is impossible at this time to predict which qubit type is best because their limitations are not precisely known, especially concerning decoherence mechanisms and their scaling. However, some general observations can be made.

First, the flux qubit has the largest nonlinearity. This implies faster logic gates since suppressing transitions from the qubit states 0 and 1 to state 2 requires long pulses whose time duration scales as $1/|\omega_{10} - \omega_{21}|$[12]. The flux qubit allows operation times less than $\sim$ 1 ns, whereas for the phase qubit 10 ns is more typical. We note, however, that this increase in speed may not be usable. Generating precise shaped pulses is much more difficult on a 1 ns time scale, and transmitting these short pulses to the qubit with high fidelity will be more problematic due to reflections or other imperfections in the microwave lines.

Second, the choice between large and small junctions involve tradeoffs. Large junctions ($E_J \gg E_C$) require precise tuning of parameters (L/L_{J0} for the flux qubit) or biases (I/I_0 for the phase qubit) to produce the required nonlinearity. Small junctions ($E_J \sim E_C$) do not require such careful tuning, but become sensitve to $1/f$ charge fluctuations because E_C has relatively larger magnitude.

Along these lines, the coherence of qubits have been compared considering the effect of low-frequency $1/f$ fluctuations of the critical current[17]. These calculations include the known scaling of the fluctuations with junction size and the sensitivity to parameter fluctuations. It is interesting that the calculated coherence times for the flux and phase qubits are similar. With parameters choosen to give an oscillation frequency of $\sim$ 1 GHz for the flux qubit and $\sim$ 10 GHz for the phase qubit, the number of coherent logic-gate operations is even approximately the same.

4. BCS theory and the superconducting state

A more complete understanding of the Josephson effect will require a derivation of Eqs. 2.1a and 2.1b. In order to calculate this microscopically, we will first review the BCS theory of superconductivity[18] using a "pair spin" derivation that we believe is more physically clear than the standard energy-variational method. Although the calculation follows closely that of Anderson[19] and Kittel[20], we have expanded it slightly to describe the physics of the superconducting phase, as appropriate for understanding Josephson qubits.

In a conventional superconductor, the attractive interaction that produces superconductivity comes from the scattering of electrons and phonons. As illustrated in Fig. 3(a), to first order the phonon interaction scatters an electron from one momentum state to another. When taken to second order (Fig. 3(b)), the scattering of a virtual phonon produces a net attractive interaction between two pairs of electrons. The first-order phonon scattering rates are generally small, not because of the phonon matrix element, but because phase space is small for the final electron state. This implies that the energy of the second order interaction can be significant if there are large phase-space factors.

The electron pairs have the largest net interaction if every pair is allowed by phase space factors to interact with every other pair. This is explicitly created in the BCS wavefunction by including only pair states (Cooper pairs) with zero net momentum. Under this assumption and using a second quantized notation where $c_k^\dagger$ is the usual creation operator for an electron state of wavevector k, the most general form for the electronic wavefunction is

$$\Psi = \prod_k (u_k + v_k e^{i\phi_k} c_k^\dagger c_{-k}^\dagger)\,|0\rangle \ , \tag{4.1}$$

where u_k and v_k are real and correspond respectively to the probability amplitude for a pair state to be empty or filled, and are normalized by $u_k^2 + v_k^2 = 1$. For generality we have included a separate phase factor ϕ_k for each pair. Because each pair state is described as a two state system, the wavefunction may also be described equivalently with a "pair-spin" tensor product

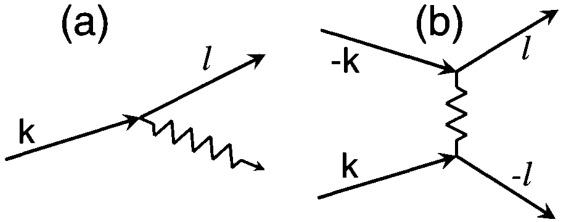

Fig. 3. Feynman diagram of electron-phonon interaction showing (a) first- and (b) second-order processes.

$$\Psi = \prod_k \begin{pmatrix} u_k \\ v_k e^{i\phi_k} \end{pmatrix} \otimes \ , \tag{4.2}$$

and the Hamiltonian given with Pauli matrices σ_{xk}, σ_{yk}, and σ_{zk}.

The kinetic part of the Hamiltonian must give Ψ in the ground state with pairs occupied only for $|k| < k_f$, where k_f is the Fermi momentum. If we define the kinetic energy of a single electron, relative to the Fermi energy, as ξ_k, then the kinetic Hamiltonian for the pair state is

$$H_K = -\sum \xi_k \sigma_{zk} \ . \tag{4.3}$$

The solution of $H_K \Psi = E_{k\pm}\Psi$ gives for the lowest energy, E_{k-}, the values $v_k = 1$ for $|k| < k_f$, and $v_k = 0$ for $|k| > k_f$, as required. An energy $E_{k+} - E_{k-} = 2\,|\xi_k|$ is needed for the excitation of pairs above the Fermi energy or the excitation of holes (removal of pairs) below the Fermi energy.

The potential part of the pair-spin Hamiltonian comes from the second-order phonon interaction that both creates and destroys a pair, as illustrated in Fig. 3(b). The Hamiltonian for this interaction is given by

$$H_\Delta = -\frac{V}{2} \sum_{k,l} (\sigma_{xk}\sigma_{xl} + \sigma_{yk}\sigma_{yl}) \ , \tag{4.4}$$

and can be checked to correspond to the second-quantization Hamiltonian $H_\Delta = -V \sum c_k^\dagger c_{-k}^\dagger c_k c_{-k}$ by using the translation $\sigma_{xk} \rightarrow c_k c_{-k} + c_k^\dagger c_{-k}^\dagger$ and $\sigma_{yk} \rightarrow i(c_k c_{-k} - c_k^\dagger c_{-k}^\dagger)$.

We will first understand the solution to the Hamiltonian $H_K + H_\Delta$ for the phase variables ϕ_k. This Hamiltonian describes a bath of spins that are all coupled to each other in the x-y plane (H_Δ) and have a distribution of magnetic fields in the z-direction (H_K). Because H_Δ is negative, each pair of spins becomes aligned with each other in the x-y plane, which implies that every spin in the bath has the same phase ϕ_k. This condition explains why the BCS wavefunction has only one phase $\phi = \phi_k$ for all Cooper pairs[21]. Because there is no preferred direction in the x-y plane, the solution to the Hamiltonian is degenerate with respect to ϕ and the wavefunction for ϕ is separable from the rest of the wavefunction. Normally, this means that ϕ can be treated as a classical variable, as is done for the conventional understanding of superconductivity and the Josephson effects. For Josephson qubits, where ϕ must be treated quantum mechanically, then the behavior of ϕ is described by an external-circuit Hamiltonian, as was done in Sec. 3.

For a superconducting circuit, where one electrode is biased with a voltage V, the voltage can be accounted for with a gauge transformation on each electron state $c_k^\dagger \rightarrow e^{i(e/\hbar)\int V dt} c_k^\dagger$. The change in the superconducting state is thus given by

$$\begin{aligned}
\Psi &\rightarrow \prod_k (u_k + v_k e^{i\phi} e^{i(e/\hbar)\int V dt} c_k^\dagger e^{i(e/\hbar)\int V dt} c_{-k}^\dagger)\,|0\rangle && (4.5)\\
&= \prod_k (u_k + v_k e^{i[\phi + i(2e/\hbar)\int V dt]} c_k^\dagger c_{-k}^\dagger)\,|0\rangle \ . && (4.6)
\end{aligned}$$

The change in ϕ can be written equivalently as

$$\frac{d\phi}{dt} = \frac{2eV}{\hbar} \ , \qquad (4.7)$$

which leads to the AC Josephson effect.

The solution for u_k and v_k proceeds using the standard method of mean-field theory, with

$$\begin{aligned}
\langle H_\Delta \rangle &= -\frac{V}{2} \sum_{k,l} (\sigma_{xk} \langle \sigma_{xl} \rangle + \sigma_{yk} \langle \sigma_{yl} \rangle) \ , && (4.8)\\
\langle \sigma_{xl} \rangle &= \left(u_l, v_l e^{-i\phi} \right) \cdot \sigma_x \cdot \begin{pmatrix} u_l \\ v_l e^{i\phi} \end{pmatrix} && (4.9)\\
&= 2 u_l v_l \cos\phi \ , && (4.10)\\
\langle \sigma_{yl} \rangle &= 2 u_l v_l \sin\phi \ . && (4.11)
\end{aligned}$$

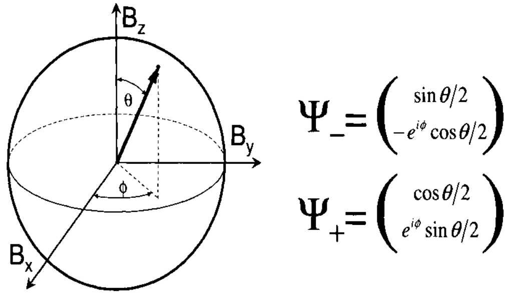

Fig. 4. Bloch sphere solution of the Hamiltonian $(\sigma_x, \sigma_y, \sigma_z) \bullet (B_x, B_y, B_z)$. The vector $\vec{B}$ gives the direction of the positive energy eigenstate.

Using the standard definition of the gap potential, one finds

$$\begin{aligned}
\Delta &= V \sum_l u_l v_l \ , && (4.12a)\\
H &= H_K + \langle H_\Delta \rangle && (4.12b)\\
&= -\sum_k (\sigma_{xk}, \sigma_{yk}, \sigma_{zk}) \cdot (\Delta\cos\phi, \Delta\sin\phi, \xi_k) \ . && (4.12c)
\end{aligned}$$

This Hamiltonian is equivalent to a spin 1/2 particle in a magnetic field, and its solution is well known. The energy eigenvalues of $H\Psi = E_{k\pm}\Psi$ are given by the total length of the field vector,

$$E_{k\pm} = \pm(\Delta^2 + \xi_k^2)^{1/2} \ , \qquad (4.13)$$

and the directions of the Bloch vectors describing the E_{k+} and E_{k-} eigenstates are respectively parallel and antiparallel to the direction of the field vector, as illustrated in Fig. 4. The ground state solution Ψ_{k-} is given by

$$\begin{aligned}
u_k &= \sqrt{\frac{1}{2}\left(1 + \frac{\xi_k}{E_k}\right)} \ , && (4.14)\\
v_k &= \sqrt{\frac{1}{2}\left(1 - \frac{\xi_k}{E_k}\right)} \ , && (4.15)\\
\phi_k &= \phi \ , && (4.16)
\end{aligned}$$

with the last equation required for consistency. The excited state Ψ_{k+} is similarly described, but with u_k and v_k interchanged and $\phi \rightarrow \phi + \pi$.

At temperature $T = 0$ the energy gap Δ may be solved by inserting the solutions for u_k and v_k into Eq. 4.12a

$$\Delta = V \sum_l \frac{\Delta}{2(\Delta^2 + \xi_k^2)^{1/2}} \; . \tag{4.17}$$

Converting to an integral by defining a density of states N_0 at the Fermi energy, and introducing a cutoff of the interaction V at the Debye energy θ_D, one finds the standard BCS result,

$$\Delta = 2\theta_D e^{-1/N_0 V} \; . \tag{4.18}$$

Two eigenstates E_{k-} and E_{k+} have been determined for the pair Hamiltonian. Two additional "quasiparticle" eigenstates must exist, which clearly have to be single-particle states. These states may be solved for using diagonalization techniques, giving

$$\Psi_{k0} = c_k^\dagger \, |0\rangle \; , \tag{4.19a}$$

$$\Psi_{k1} = c_{-k}^\dagger \, |0\rangle \; . \tag{4.19b}$$

Fortunately, these states may be easily checked by inspection. The kinetic part of the Hamiltonian gives $H_K \Psi_{k0,1} = 0$ since $\Psi_{k0,1}$ corresponds to the creation of an electron and a hole, and the electron-pair and hole-pair states have opposite kinetic energy. The potential part of the energy also gives $\langle H_\Delta \rangle \, \Psi_{k0,1} = 0$ since the interaction Hamiltonian scatters pair states. Thus the eigenenergies of $\Psi_{k0,1}$ are zero, and these states have an energy $E_k = |E_{k-}|$ above the ground state.

The quasiparticle operators that take the ground-state wavefunction to the excited states are

$$\gamma_{k0}^\dagger = u_k c_k^\dagger - v_k e^{-i\phi} c_{-k} \; , \tag{4.20}$$

$$\gamma_{k1}^\dagger = u_k c_{-k}^\dagger + v_k e^{-i\phi} c_k \; , \tag{4.21}$$

which can be easily checked to give

$$\gamma_{k0}^\dagger (u_k + v_k e^{i\phi} c_k^\dagger c_{-k}^\dagger) \, |0\rangle = c_k^\dagger \, |0\rangle \; , \tag{4.22}$$

$$\gamma_{k1}^\dagger (u_k + v_k e^{i\phi} c_k^\dagger c_{-k}^\dagger) \, |0\rangle = c_{-k}^\dagger \, |0\rangle \; . \tag{4.23}$$

A summary of these results is illustrated in Fig. 5, where we show the energy levels, wavefunctions, and operators for transitions between the four states. The quasiparticle raising and lowering operators $\gamma_{k0}^\dagger$, $\gamma_{k1}^\dagger$, γ_{k0}, and γ_{k1} produce transitions between the states and have orthogonality relationships similar to those of the electron operators.

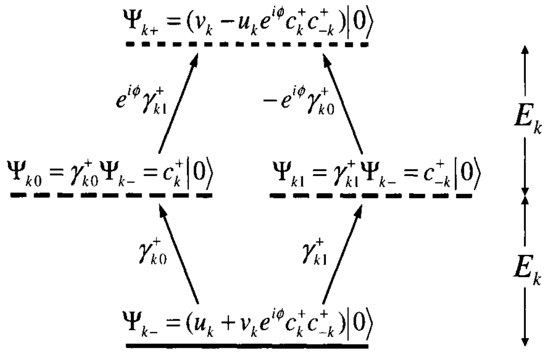

Fig. 5. Energy-level diagram for the ground-pair state (solid line), two quasiparticle states (dashed lines), and the excited-pair state (short dashed line).

It is interesting to note that the ground and excited pair states are connected by the two quasiparticle operators $e^{-i\phi}\gamma_{k1}^\dagger \gamma_{k0}^\dagger \Psi_{k-} = \Psi_{k+}$. Because the value $u_l v_l$ changes sign between Ψ_{k-} and Ψ_{k+}, and is zero for $\Psi_{k0,1}$, the gap equation 4.12a including the effect of quasiparticles is proportional to $\langle 1 - \gamma_{k0}^\dagger \gamma_{k0} - \gamma_{k1}^\dagger \gamma_{k1} \rangle$. Along with the energy levels, these results imply that the two types of quasiparticles are independent excitations.

5. The Josephson effect, derived from perturbation theory

We will now calculate the quasiparticle and Josephson current for a tunnel junction using first and second order perturbation theory, respectively. We note that our prior calculations have not been concerned with electrical transport. In fact, the electron operators describing the superconducting state have not been influenced by charge, and thus they correspond to the occupation of an effectively neutral state. Because a tunneling event involves a real transfer of an electron, charge must now be accounted for properly. We will continue to use electron operators for describing the states, but will keep track of the charge transfer separately.

When an electron tunnels through the barrier, an electron and hole state is created on the opposite (left and right) side of the barrier. The tunneling Hamiltonian for this process can be written as

$$
\begin{aligned}
H_T &= \overrightarrow{H}_{T+} + \overrightarrow{H}_{T-} + \overleftarrow{H}_{T+} + \overleftarrow{H}_{T-} &\text{(5.1a)}\\
&= \sum_{L,R} \Big(t_{LR} c_L c_R^\dagger + t_{-L-R} c_{-L} c_{-R}^\dagger + t_{LR}^* c_L^\dagger c_R \\
&\quad + t_{-L-R}^* c_{-L}^\dagger c_{-R} \Big) \,, &\text{(5.1b)}
\end{aligned}
$$

where t_{LR} is the tunneling matrix element, and the L and R indices refer respectively to momentum states k on the left and right superconductor. The first two terms $\overrightarrow{H}_{T+}$ and $\overrightarrow{H}_{T-}$ correspond to the tunneling of one electron from left to the right, whereas $\overleftarrow{H}_{T+}$ and $\overleftarrow{H}_{T-}$ are for tunneling to the left. The Hamiltonian is explicitly broken up into $\overrightarrow{H}_{T+}$ and $\overrightarrow{H}_{T-}$ to account for the different electron operators $c_k^\dagger$ and $c_{-k}^\dagger$ for positive and negative momentum.

The electron operators must first be expressed in terms of the quasiparticle operators γ because these produce transitions between eigenstates of the superconducting Hamiltonian. Equations 4.20, 4.21, and their adjoints are used to solve for the four electron operators

$$
\begin{aligned}
c_k &= u_k \gamma_{k0} + v_k e^{i\phi} \gamma_{k1}^\dagger & c_{-k} &= u_k \gamma_{k1} - v_k e^{i\phi} \gamma_{k0}^\dagger \\
c_k^\dagger &= u_k \gamma_{k0}^\dagger + v_k e^{-i\phi} \gamma_{k1} & c_{-k}^\dagger &= u_k \gamma_{k1}^\dagger - v_k e^{-i\phi} \gamma_{k0} \,.
\end{aligned}
\qquad (5.2)
$$

Substituting Eqs. 5.2 into 5.1b, one sees that all four terms of the Hamiltonian have operators $\gamma^\dagger$ that produce quasiparticles. We calculate here to first order the quasiparticle current from L to R given by $\overrightarrow{H}_{T+} + \overrightarrow{H}_{T-}$. The Feynman diagrams (a) and (b) in Fig. 6 respectively describe the tunneling Hamiltonian for the $\overrightarrow{H}_{T+}$ and $\overrightarrow{H}_{T-}$ terms. In this diagram a solid line represents a Cooper pair state in the ground state, whereas a quasiparticle state is given by a dashed line. Only one pair participates in the tunneling interaction, so only one of the three solid lines is converted to a dashed line. The line of triangles represents the tunneling event and is labeled with its corresponding H_T Hamiltonian, with the direction of the triangles indicating the direction of the electron tunneling. The $c_k^\dagger$ operators, acting on the L or R lead, is rewritten in terms of the γ operators and placed above or below the vertices. Since only $\gamma^\dagger$ operators give a nonzero term when acting on the ground state, the effect of the interaction is to produce final states $\Psi_f^{L,R}$ with total energy $E_R + E_L$, and with amplitudes given at the right of the figure.

The two final states in Fig 6(a) and (b) are orthogonal, as well as states involving different values of L and R. The total current is calculated as an incoherent sum over all possible final quasiparticle states, under the condition that the total quasiparticle energy for the final state is equal to the energy gained by the tunneling of the electron

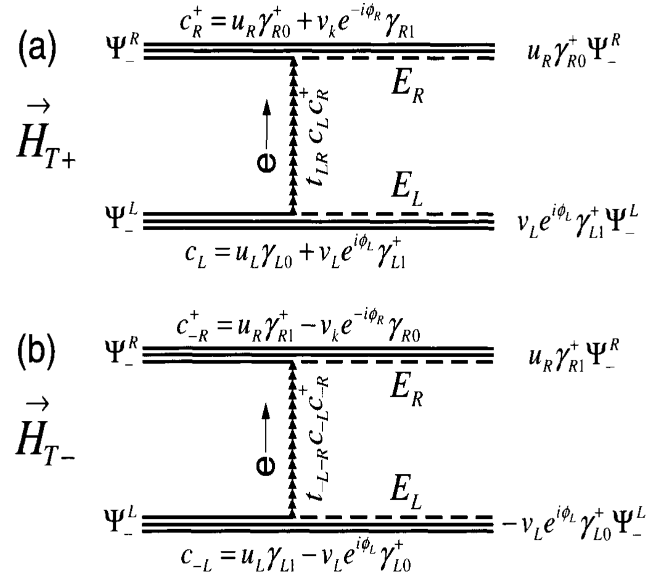

Fig. 6. First-order Feynmann diagrams for interaction $\overrightarrow{H}_{T+}$ (a) and $\overrightarrow{H}_{T-}$ (b). Solid lines are Cooper-pair states, dashed lines are quasiparticle excitations, and arrow-lines represents tunneling interaction. Electron operators arising from interaction are displayed next to vertices.

$$E_R + E_L = eV \,. \qquad (5.3)$$

The total current from L to R is given by e multiplied by the transition rate

$$
\begin{aligned}
\overrightarrow{I_{qp}} &= e\frac{2\pi}{\hbar} \sum_{L,R}^{(E_R+E_L=eV)} \left| \left\langle \Psi_f^L \right| \left\langle \Psi_f^R \right| \overrightarrow{H}_{T+} + \overrightarrow{H}_{T-} \left| \Psi_-^R \right\rangle \left| \Psi_-^L \right\rangle \right|^2 &\text{(5.4a)}\\
&= \frac{2\pi e}{\hbar} \sum_{L,R}^{(E_R+E_L=eV)} \left[\left| t_{LR} \right|^2 + \left| t_{-L-R} \right|^2 \right] (u_R v_L)^2 &\text{(5.4b)}\\
&= \frac{4\pi e}{\hbar} |t|^2 N_{0R} N_{0L} \int_{-\infty}^{\infty} v_L^2 \, d\xi_L \int_{-\infty}^{\infty} u_R^2 \, d\xi_R \, \delta(eV - E_L - E_R) \,, &\text{(5.4c)}
\end{aligned}
$$

where in the last equation we have expressed the conservation of energy with a Dirac δ-function, and have assumed matrix elements $|t|^2$ of constant strength. Because $E(\xi_k) = E(-\xi_k)$ and $u_k(\xi_k) = v_k(-\xi_k)$, one finds

$$\begin{aligned}
\overrightarrow{I_{qp}} &= \frac{4\pi e}{\hbar}|t|^2 N_{0R}N_{0L}\int_0^\infty (v_L^2 + u_L^2)d\xi_L \\
&\quad \int_0^\infty (u_R^2 + v_R^2)\,d\xi_R\,\delta(eV - E_L - E_R) \\
&= \frac{4\pi e}{\hbar}|t|^2 N_{0R}N_{0L}\int_0^\infty d\xi_L\int_0^\infty d\xi_R\,\delta(eV - E_L - E_R)\,. \qquad (5.5a)
\end{aligned}$$

This result is equivalent to the standard "semiconductor model" of the quasiparticle current, which predicts no current for $V < 2\Delta/e$, a rapid rise of current at $2\Delta/e$, and then a current proportional to V at large voltages. Note that Eq. 5.4c has a sum over the occupation probability v_L^2 of the pair state and the occupation probability u_R^2 of a hole-pair state, as is expected given the operators $c_L c_R^\dagger$ in the tunneling Hamiltonian. The final result of Eq. 5.5a does not have these factors because the occupation probability is unity when summed over the $\pm\xi_k$ states.

It is convenient to express the tunneling matrix element in terms of the normal-state resistance of the junction, obtained by setting $\Delta = 0$, with the equation

$$\begin{aligned}
1/R_N &\equiv \overrightarrow{I_{qp}}/V \qquad (5.6a) \\
&= \frac{4\pi e}{\hbar}|t|^2 N_{0R}N_{0L}\int_0^\infty d\xi_L\int_0^\infty d\xi_R\,\delta(eV - \xi_L - \xi_R)/V \qquad (5.6b) \\
&= \frac{4\pi e^2}{\hbar}|t|^2 N_{0R}N_{0L}\,. \qquad (5.6c)
\end{aligned}$$

We now calculate the tunneling current with second-order perturbation theory. The tunneling Hamiltonian, taken to second order, gives

$$H_T^{(2)} = \sum_i H_T\frac{1}{\epsilon_i}H_T\,, \qquad (5.7)$$

where ϵ_i is the energy of the intermediate state i. Because the terms in H_T have both $\gamma^\dagger$ and γ operators, the second-order Hamiltonian gives a nonzero expectation value for the ground state. This is unlike the first-order theory, which produces current only through the real creation of quasiparticles.

Because H_T has terms that transfer charge in both directions, $H_T H_T$ will produce terms which transfer two electrons to the right, two to the left, and with no net transfer. With no transfer, a calculation of the second-order energy gives a constant value, which has no physical effect. We first calculate terms for transfer to the right from $(\overrightarrow{H}_{T+} + \overrightarrow{H}_{T-})(\overrightarrow{H}_{T+} + \overrightarrow{H}_{T-})$, which gives nonzero expectation values only for $\overrightarrow{H}_{T+}\overrightarrow{H}_{T-} + \overrightarrow{H}_{T-}\overrightarrow{H}_{T+}$. The Feynman diagrams for these two terms are given in Fig. 7(a) and (b), where we have displayed only the amplitudes from the nonzero operators. The expectation value of these two Hamiltonian terms is given by

$$\begin{aligned}
\left\langle \overrightarrow{H_T^{(2)}} \right\rangle &= -\sum_{L,R}\left\langle \Psi_-^R\right|\left\langle \Psi_-^L\right|(v_R e^{-i\phi_R}u_L) \\
&\quad \times\frac{\gamma_{R0}\gamma_{L1}\gamma_{R0}^\dagger\gamma_{L1}^\dagger t_{LR}t_{-L-R} + \gamma_{R1}\gamma_{L0}\gamma_{R1}^\dagger\gamma_{L0}^\dagger t_{-L-R}t_{LR}}{E_R + E_L} \\
&\quad \times(u_R v_L e^{i\phi_L})\left|\Psi_-^L\right\rangle\left|\Psi_-^R\right\rangle \qquad (5.8a) \\
&= -2|t|^2 e^{i(\phi_L - \phi_R)}\sum_{L,R}(v_R u_R)(u_L v_L)\frac{1}{E_R + E_L} \qquad (5.8b) \\
&= -2|t|^2 e^{i\delta}N_{0R}N_{0L}\int_{-\infty}^\infty d\xi_R\int_{-\infty}^\infty d\xi_L\frac{\Delta}{E_R}\frac{\Delta}{E_L}\frac{1}{E_R + E_L} \qquad (5.8c) \\
&= -\frac{\hbar\Delta}{2\pi e^2 R_N}e^{i\delta}\int_{-\infty}^\infty d\theta_R\int_{-\infty}^\infty d\theta_L\frac{1}{\cosh\theta_R + \cosh\theta_L} \qquad (5.8d) \\
&= -\frac{\hbar\Delta}{2\pi e^2 R_N}e^{i\delta}\left(\frac{\pi}{2}\right)^2\,, \qquad (5.8e)
\end{aligned}$$

where we have used $t_{LR}^* = t_{-L-R}$ and assumed the same gap Δ for both superconductors. A similar calculation for transfer to the left gives the complex conjugate of Eq. 5.8e. The sum of these two energies gives the Josephson energy U_J, and using Eq. 2.5, the Josephson current I_J,

$$\begin{aligned}
U_J &= -\frac{1}{8}\frac{R_K}{R_N}\Delta\cos\delta\,, \qquad (5.9) \\
I_J &= \frac{\pi}{2}\frac{\Delta}{eR_N}\sin\delta\,, \qquad (5.10)
\end{aligned}$$

where $R_K = h/e^2$ is the resistance quantum. Equation 5.10 is the standard

Ambegaokar-Baratoff formula[22] for the Josephson current at zero temperature.

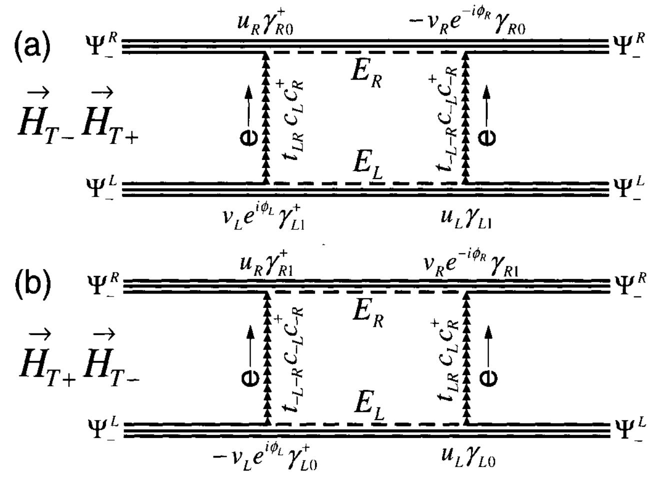

Fig. 7. Second-order Feynman diagrams for the transfer of two electrons across the junction. Only nonzero operators are displayed next to vertices.

The Josephson current is a dissipationless current because it arises from a new ground state of the two superconductors produced by the tunneling interaction. This behavior is in contrast with quasiparticle tunneling, which is dissipative because it produces excitations. It is perhaps surprising that a new ground state can produce charge transfer through the junction. This is possible only because the virtual quasiparticle excitations are both electrons and holes: the electron-part tunnels first through the junction, then the hole-part tunnels back. Only states of energy Δ around the Fermi energy are both electron- and hole-like, as weighted by the $(v_R u_R)(u_L v_L)$ term in the integral.

The form of the Josephson Hamiltonian can be understood readily by noting that the second-order Hamiltonian,

$$\vec{H}_{T+}\vec{H}_{T-} \sim |t|^2 \sum_{L,R} c_L c_{-L} c_R^\dagger c_{-R}^\dagger \tag{5.11}$$

$$= \frac{|t|^2}{2} \sum_{L,R} (\sigma_{xL}\sigma_{xR} + \sigma_{yL}\sigma_{yR}) \, , \tag{5.12}$$

corresponds to the pair-scattering Hamiltonian of Eq. 4.4. Comparing with the gap-equation solution, one expects $U_J \sim |t|^2 \, \Delta \cos\delta$, where the $\cos\delta$ term arises from the spin-spin interaction in the x-y plane.

We would like to make a final comment on a similarity between the BCS theory and the Josephson effect. In both of these derivations we see that a dissipative process that is described in first-order perturbation theory, such as phonon scattering or quasiparticle tunneling, produces in second order a new collective superfluid behavior. This collective behavior emerges from a virtual excitation of the dissipative process. Dissipation is normally considered undesirable, but by designing systems to *maximize* dissipation, it may be possible to discover new quantum collective behavior.

With this understanding of the Josephson effect and quasiparticle tunneling, how accurate is the description of the Josephson junction with the Hamiltonian corresponding to Eq. 5.9? There are several issues that need to be considered.

First, quasiparticle tunneling is a dissipative mechanism that produces decoherence. Although it is predicted to be absent for $V < 2\Delta/e$, measurements of real junctions show a small subgap current. This current is understood to arise from multiple Andreev reflections, which are described as higher-order tunneling processes. We thus need a description of the tunnel junction that easily predicts these processes for arbitrary tunneling matrix elements. This is especially needed as real tunnel junctions do not have constant matrix elements, as assumed above. Additionally, we would like to know whether a small number of major imperfections, such as "pinhole" defects, will strongly degrade the coherence of the qubit.

Second, quasiparticle tunneling has been predicted for an arbitrary DC voltage across the junction. However, the qubit state has $\langle V \rangle = 0$, but may excite quasiparticles with AC voltage fluctuations. This situation is difficult to calculate with perturbation theory. In addition, is it valid to estimate decoherence from quasiparticles at zero voltage simply from the junction resistance at subgap voltages?

Third, how will the Josephson effect and the qubit Hamiltonian be modified under this more realistic description of the tunnel junction?

All of these questions and difficulties arise because perturbation theory has been used to describe the ground state of the Josephson junction. The BCS theory gives basis states that best describe quasiparticle tunneling for large voltages, not for $V \to 0$. A theory is needed that solves for the Josephson effect *exactly*, with this solution then providing the basis states for understanding quasiparticle tunneling around $V = 0$. This goal is fulfilled by the theory of quasiparticle bound states, which we will describe next.

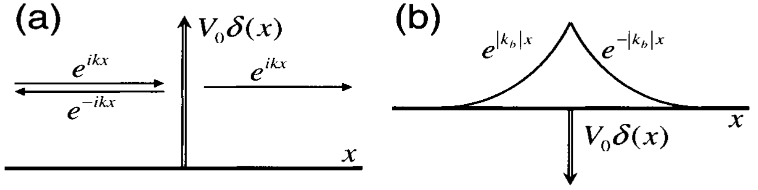

Fig. 8. Plot of potential *vs.* coordinate x with a positive delta-function tunnel barrier $V_0\delta(x)$. Scattering of plane wave states is shown in (a), whereas (b) is a plot of the bound-state wavefunction. The delta-function barrier is negative in (b), as required for producing a bound state.

6. The Josephson effect, derived from quasiparticle bound states

We begin our derivation of an exact solution for the Josephson effect with an extremely powerful idea from mesoscopic physics: electrical transport can be calculated under very general conditions by summing the current from a number of *independent* "conduction channels", with the transport physics of each conduction channel determined only by its channel transmission probability τ_i[23, 24]. For a Josephson junction, the total junction current I_j can be written as a sum over all channels i

$$I_j = \sum_i I_j(\tau_i)\,, \tag{6.1}$$

where $I_j(\tau)$ is the current for a single channel of transmission τ, which may be solved for theoretically. For a tunnel junction, the number of channels is estimated as the junction area divided by the channel area $(\lambda_f/2)^2$, where λ_f is the Fermi wavelength of the electrons. Of course, the difficulty of determining the distribution of the channel transmissions still remains. This often may be estimated from transport properties, and under some situations can be predicted from theory[25, 26, 27].

Because transport physics is determined *only* by scattering parameterized by τ, we may make two simplifying assumptions: the transport can be solved for using plane waves, and the scattering from the tunnel junction can be described by a delta function. The general theory has thus been transformed into the problem of one-dimensional scattering from a delta function, and an exact solution can be found by using a simple and clear physical picture.

Central to understanding the Josephson effect will be the quasiparticle bound state. To understand how to calculate a bound state[28, 29], we will first consider a normal-metal tunnel junction and with a δ-function barrier $V_0\overline{\delta}(x)$, as illustrated in Fig. 8. For an electron of mass m and wavevector k, the wavefunctions on the

left and right side of the barrier are

$$\Psi_L = Ae^{ikx} + Be^{-ikx}\,, \tag{6.2}$$
$$\Psi_R = Ce^{ikx}\,, \tag{6.3}$$

where A, B, and C are respectively the incident, reflected, and transmitted electron amplitudes. From the continuity equations

$$\Psi_L = \Psi_R \tag{6.4}$$
$$\frac{d\Psi_L}{dx} = \frac{d\Psi_R}{dx} - \frac{2mV_0}{\hbar^2}\Psi_R \tag{6.5}$$

evaluated at $x = 0$, the amplitudes are related by

$$A + B = C \tag{6.6}$$
$$ikA - ikB = ikC - \frac{2mV_0}{\hbar^2}C\,. \tag{6.7}$$

The transmission amplitude and the probability are

$$\frac{C}{A} = \frac{1}{1+i\eta}\,, \tag{6.8}$$
$$\tau = \left|\frac{C}{A}\right|^2 = \frac{1}{1+\eta^2}\,, \tag{6.9}$$

where $\eta = mV_0/\hbar^2 k$. The bound state can be determined by finding the pole in the transmission amplitude. A pole describes how a state of finite amplitude may be formed around the scattering site with zero amplitude of the incident wavefunction, which is the definition of a bound state. The pole at $\eta = i$ gives $k_b = -imV_0/\hbar^2$, and a wavefunction around the scattering site $\Psi_R = Ce^{(mV_0/\hbar^2)x}$. This describes a bound state only when V_0 is negative, as expected.

A superconducting tunnel junction will also have bound states of quasiparticles excitations. These bound states describe the Josephson effect since virtual quasiparticle tunneling was necessary for the perturbation calculation in the last section. The Bogoliubov-deGennes equations describe the spatial wavefunctions, whose eigenstates are given by the solution of the Hamiltonian

$$H\varphi^{\pm}e^{i\kappa x} = \left(\pm k_f \frac{\hbar^2\kappa}{m}\sigma_z + \Delta\sigma_x\right)\varphi^{\pm}e^{i\kappa x}\,, \tag{6.10}$$

where $\varphi^{\pm}e^{i\kappa x}$ are the slowly varying spatial amplitudes of the exact wavefunction $\varphi^{\pm}e^{i\kappa x}e^{\pm ik_f x}$. As illustrated in Fig. 9, the $\pm k_f\kappa$ term corresponds to the kinetic

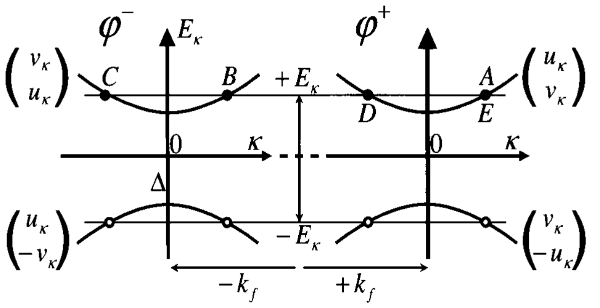

Fig. 9. Plot of quasiparticle energies E_κ verses momentum κ near the $\pm k_f$ Fermi surfaces. The two-component eigenfunctions are also displayed for each of the four energy bands. Also indicated are the quasiparticle states A-E used for the bound-state calculation.

energy at the $\pm k_f$ Fermi surfaces using the approximation $(k_f+\kappa)^2/2 \simeq$ const.$+$ $k_f\kappa$. As expected for a spin-type Hamiltonian, the two eigenvalues are

$$E_\kappa = \pm(\xi_\kappa^2 + \Delta^2)^{1/2} , \tag{6.11}$$

where $\xi_\kappa = \hbar^2 k_f \kappa / m$ is the kinetic energy of the quasiparticle referred to the Fermi energy. The eigenvectors are also displayed in Fig. 9, where u_κ and v_κ are given by Eqs. 4.14 and 4.15. Because the two energy bands represent quasiparticle excitations, the lower band is normally filled and its excitations correspond to the creation of hole states.

We can solve for the quasiparticle bound states by first writing down the scattering wavefunctions in the left and right superconducting electrodes. An incoming quasiparticle state, point A in Fig. 9, is reflected off the tunnel barrier to states B and C and is transmitted to states D and E [30]. The wavefunctions are then given by

$$\Psi_L = A\begin{pmatrix} u \\ ve^{i\phi_L} \end{pmatrix} e^{i\kappa x} + B\begin{pmatrix} v \\ ue^{i\phi_L} \end{pmatrix} e^{i\kappa x} + C\begin{pmatrix} u \\ ve^{i\phi_L} \end{pmatrix} e^{-i\kappa x} \tag{6.12}$$

$$\Psi_R = D\begin{pmatrix} v \\ ue^{i\phi_R} \end{pmatrix} e^{-i\kappa x} + E\begin{pmatrix} u \\ ve^{i\phi_R} \end{pmatrix} e^{i\kappa x} , \tag{6.13}$$

where we have used the relations $v \equiv v_\kappa = u_{-\kappa}$ and $u \equiv u_\kappa = v_{-\kappa}$, and we have included the phases ϕ_L and ϕ_R of the two states. The continuity conditions Eqs. 6.4 and 6.5, solved for both the components of the spin wavefunction, gives the matrix equation

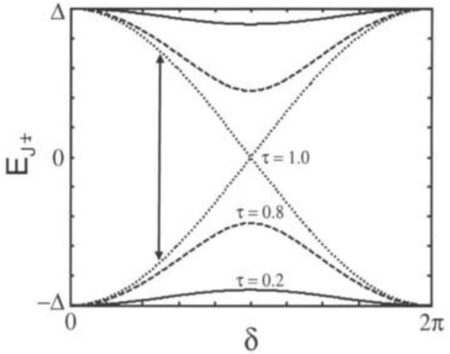

Fig. 10. Plot of quasiparticle bound-state energies E_{J-} and E_{J+} vs. the phase difference δ across the junction, for three values of tunneling transmission τ. Quasiparticles are produced by vertical transitions from the E_{J-} to E_{J+} band. As indicated by the arrow, the energy gap $E_{J+} - E_{J-}$ is always greater than $\sqrt{2}\Delta$ at $\delta = \pi/2$.

$$A\begin{pmatrix} u \\ v \\ u \\ v \end{pmatrix} = \begin{pmatrix} -v & -u & v & u \\ -u & -v & ue^{-i\delta} & ve^{-i\delta} \\ -v & u & -v(1-i2\eta) & u(1+i2\eta) \\ -u & v & -ue^{-i\delta}(1-i2\eta) & ve^{-i\delta}(1+i2\eta) \end{pmatrix} \begin{pmatrix} B \\ C \\ D \\ E \end{pmatrix} . \tag{6.14}$$

The scattering amplitudes for B-E have poles given by the solution of

$$(u^4 + v^4)(1+\eta^2) - 2(uv)^2(\eta^2 + \cos\delta) = 0 . \tag{6.15}$$

Using the relations $u^2 + v^2 = 1$, $E_J = E_k = \Delta/2uv$, and $\tau = 1/(1+\eta^2)$, the energies of the quasiparticle bound states are

$$E_{J\pm} = \pm\Delta[1 - \tau\sin^2(\delta/2)]^{1/2} . \tag{6.16}$$

Because these two states have energies less than the gap energy Δ, they are energetically "bound" to the junction and thus have wavefunctions that are localized around the junction.

The dependence of the quasiparticle bound-state energies on junction phase is plotted in Fig. 10 for several values of τ. The ground state is normally filled, similar to the filling of quasiparticle states of negative energy. The energy E_{J-} corresponds to the Josephson energy, as can be checked in the limit $\tau \to 0$ to give

$$E_{J-} \simeq -\Delta + \frac{\Delta\tau}{4} - \frac{\Delta\tau}{4}\cos\delta . \tag{6.17}$$

This result is equivalent to Eq. 5.9 after noting that the normal-state conductance of a single channel is $1/R_N = 2\tau/R_K$.

The current of each bound state is given by the derivative of its energy

$$I_{J\pm} = \frac{2\pi}{\Phi_0}\frac{\partial E_{J\pm}}{\partial\delta}\,, \tag{6.18}$$

in accord with Eq. 2.5. Since the curvature of the upper band is opposite to that of the lower band, the currents of the two bands have opposite sign $I_{J+} = -I_{J-}$. For level populations of the two states given by $f_\pm$, the average Josephson current is $\langle I_J\rangle = I_{J-}(f_- - f_+)$. For a thermal population, $f_\pm$ are given by Fermi distributions, and the Josephson current in the tunnel junction limit gives the expected Ambegaokar-Baratoff result

$$\begin{aligned}\langle I_J\rangle &= \frac{\pi}{2}\frac{\Delta(T)}{eR_N}\sin\delta\cdot\left(\frac{1}{e^{-\Delta/kT}+1}-\frac{1}{e^{\Delta/kT}+1}\right) && (6.19)\\ &= \frac{\pi}{2}\frac{\Delta(T)}{eR_N}\tanh(\Delta/2kT)\sin\delta\,. && (6.20)\end{aligned}$$

7. Generation of quasiparticles from nonadiabatic transitions

In this description of the Josephson junction, the Josephson effect arises from a quasiparticle bound state at the junction. Two bound states exist and have energies E_{J+} and E_{J-}, with the Josephson current from the excited state being of opposite sign from that of the ground state. We will discuss here the small-voltage limit[31, 32], which can be fully understood within a semiclassical picture by considering that a linear increase in δ produces nonadiabatic transitions between the two states.

The junction creates "free quasiparticles", those with $E \geq \Delta$, via a two-step process. First, a transition is made from the ground to the excited bound state. This typically occurs because a voltage is placed across the junction, and the linear change of δ causes the ground state not to adiabatically stay in that state. For a high-transmission channel, the transition is usually made around $\delta \approx \pi$, where the energy difference between the states is the lowest and the band bending is the highest. Because this excited state initially has energy less than Δ, the state remains bound until the phase changes to 2π and the energy of the quasiparticle is large enough to become unbound and diffuse away from the junction. The quasiparticle generation rate is thus governed by $d\delta/dt$ and will increase as V increases.

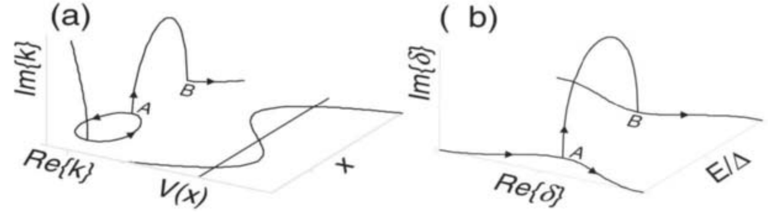

Fig. 11. Plot of semiclassical solutions for the tunneling through a barrier (a) and tunneling through an energy gap (b). Imaginary solutions to k and δ are used to calculate the tunneling rates.

The quasiparticle transition rate can be predicted using a simple semi-classical method. We will first review WKB tunneling in order to later generalize this calculation to energy tunnelling. In Fig. 11(a), we plot a cubic potential $V(x)$ versus x and its solution $k^2 = 2m[E - V(x)]/\hbar^2$. The solution for k is real or imaginary depending on whether E is greater or less than $V(x)$. A semi-classical description of the system is the particle oscillating in the well, as described by the loop in the solution of Re$\{k\}$. A solution in the imaginary part of k connects a turning point on this loop, labeled A, with the turning point of the free-running solution, labeled B. The probability of tunneling each time the trajectory passes point A is given by the standard WKB integral of the imaginary action

$$\begin{aligned} W &= \exp[-2S] && (7.1)\\ S &= (1/\hbar)\left|\int dx\,\mathrm{Im}\,p\right| && (7.2)\\ &= \left|\int_{x_A}^{x_B} dx\,\mathrm{Im}\,k\right|. && (7.3)\end{aligned}$$

The transition rate for a nonadiabatic change in a state may be calculated in a similar fashion. In Fig. 11(b) we plot the solution of Eq. 6.16 for δ versus E. In the "forbidden" region of energy $|E| < \Delta\sqrt{1-\tau}$, the solution of δ has an imaginary component. As the bias of the system changes and the system trajectory moves past point A, then this state can tunnel to point B via the connecting path in the imaginary part of δ. The probability for this event is given by Eq. 7.1 with S given by the integral of the imaginary action

$$S = (1/\hbar)\int dE\,t_{\mathrm{imag}}\,, \tag{7.4}$$

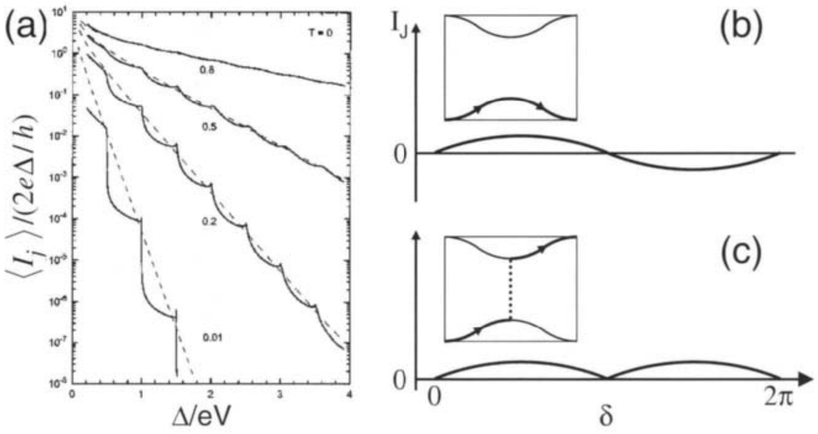

Fig. 12. (a) Plot of average junction current $\langle I_j \rangle$ versus inverse DC voltage V for transmission coefficients $\tau = 0.8, 0.5, 0.2$, and 0.01 (from Ref. [32]). Solid lines are from exact calculation, and dashed lines are from predictons of Eqs. 7.8 and 7.6. The time dependence of the Josephson current I_J is plotted for the ground state (b) and for a transition (c), where the insets show the trajectory of the bound states as E_J *vs.* δ.

where we define an imaginary time by

$$t_{\text{imag}} = \left| \frac{\operatorname{Im}\delta}{d\delta/dt} \right| . \tag{7.5}$$

Rewriting Eq. 6.16 as $(E/\Delta)^2 = 1 - \tau(1 - \cos\delta)/2$ and using $d\delta/dt = (2e/\hbar)V$, one finds the action is given by the integral

$$\begin{aligned} S &= \frac{\Delta}{2eV} \int_{-\sqrt{1-\tau}}^{\sqrt{1-\tau}} d\epsilon \ \operatorname{Im}\left\{ -\arccos\left[1 + (\varepsilon^2 - 1)2/\tau \right] \right\} \qquad (7.6) \\ &\simeq \frac{\Delta}{eV} \times \begin{cases} (1-\tau)\pi/2 & (\tau \to 1) \\ \ln(2/\tau) & (\tau \to 0) \\ (1-\tau)\left[\ln(2/\tau) + \sqrt{\tau}(\pi/2 - \ln 2)\right] , & \text{(interp.)} \end{cases} \end{aligned}$$

where the last interpolation formula approximates well a numerical solution of Eq. 7.6. The limiting expression for $\tau \to 1$ gives the standard Landau-Zener formula appropriate for a two-state system. In the tunnel-junction limit $\tau \to 0$ one finds

$$W = (\tau/2)^{2\Delta/eV} . \tag{7.7}$$

For the case of a constant DC bias voltage V, the total junction current $\langle I_j \rangle$ may be calculated with this transition rate and an attempt rate $\Gamma = (2e/h)V$

given by the frequency at which δ passes $\pi/2$. Using Eq. 7.6 and setting the power of quasiparticle generation $2\Delta\Gamma W$ to the electrical power $\langle I_j \rangle V$, one finds

$$\langle I_j \rangle = \frac{2e\Delta}{\pi\hbar} W . \tag{7.8}$$

This prediction is plotted in Fig. 12(a) and shows very good agreement with the results of exact calculations[32]. Only the steps in voltage are not reproduced, which are understood as arising from the quantization of energy eV from multiple Andreev reflection of the quasiparticles. The steps are not expected to be reproduced by the semiclassical theory since this theory is an expansion around small voltages, or equivalently, large quantization numbers.

The junction current may also be determined from the energies of the two bound states. For a constant voltage across the junction, we use Eq. 2.5 to calculate the charge transferred across the junction after a phase change of 2π

$$\begin{aligned} Q_j &= \int_0^{2\pi/(d\delta/dt)} I_j \, dt && (7.9) \\ &= \frac{2\pi}{\Phi_0} \int_0^{2\pi/(d\delta/dt)} \frac{dU_J}{d\delta} dt && (7.10) \\ &= \frac{[U_J(2\pi) - U_J(0)]}{V} , && (7.11) \end{aligned}$$

which gives the expected result that the change of energy equals $Q_j V$. When the junction remains in the ground state, the energy is constant $U_J(2\pi) - U_J(0) = 0$ and no net charge flows through the junction. Net charge is transferred, however, after a transition. The charge transfer $2\Delta/V$ multiplied by the transition rate gives an average current $Q_j \Gamma W$ that is equivalent to Eq. 7.8.

Equation 6.18 may be used to calculate the time dependence of the Josephson current, as illustrated in Fig. 12(b) and (c). When the system remains in the ground state (b), the junction current is sinusoidal and averages to zero. For the case of a transition (c), the current before the transition is the same, but the Josephson current remains positive after the transition (see Eq. 5.4 of Ref. [32]). The transition itself also produces charge transfer from multiple-Andreev reflections(MAR) [31, 33]

$$Q_{\text{MAR}} = 2\Delta(1-\tau)^{1/2}/V . \tag{7.12}$$

This result is perhaps surprising - the junction current at finite voltage arises from transfer of charge Q_{MAR} *and* a change in the Josephson current. The relative contribution of these two currents is determined by the relative size of the gap in the bound states. For $\tau \to 1$, all of the junction current is produced by Josephson current, whereas for $\tau \to 0$ (tunnel junctions) the current comes from Q_{MAR}.

For small voltages, the transition event must transfer a large amount of charge $Q_{\rm MAR}$ in order to overcome the energy gap. In comparing this semi-classical theory with the exact MAR theory, $Q_{\rm MAR}/e$ has an integer value and represents the order of the MAR process and the number of electrons that are transferred in the transition. This description is consistent with Eq. 7.7 describing the transition probability for an n-th order MAR process, where $n = 2\Delta/eV$, and $\tau/2$ represents the matrix element for each order.

From this example it is clearly incorrect to picture the quasiparticle and Josephson current as separate entities, as suggested by the calculations of perturbation theory. To do so ignores the fact that quasiparticle tunneling, arising from a transition between the bound states, also changes the Josephson contribution to the current from $\delta = \pi$ to 2π.

8. Quasiparticle bound states and qubit coherence

The quasiparticle bound-state theory can be used to predict both the Josephson and quasiparticle current in the zero-voltage state, as appropriate for qubits. In this theory an excitation from the E_{J-} bound state to the E_{J+} state is clearly deleterious as it will change the Josephson current, fluctuating the qubit frequency and producing decoherence in the phase of the qubit state. For an excitation in one channel, the fractional change in the Josephson current is $\sim 1/N_{\rm ch}$, where $N_{\rm ch}$ is the number of conduction channels. The subgap current-voltage characteristics can be used to estimate $N_{\rm ch}$, which gives an areal density of $\sim 10^4/\mu{\rm m}^2$ [10, 34]. For a charge qubit with junction area $10^{-2}\mu{\rm m}^2$, the qubit frequency changes fractionally by $\sim 1/N_{\rm ch} \sim 10^{-2}$ for a single excitation, and gives strong decoherence. Although the phase qubit has a smaller change $(1/N_{\rm ch})I_0/4(I_0 - I) \sim 2 \times 10^{-5}$, the excitation of even a single bound state is clearly unwanted.

Fortunately, these quasiparticle bound states should not be excited in tunnel junctions by the dynamical behavior of the qubit. The E_{J-} to E_{J+} transition is energetically forbidden because the energy of the qubit states are typically choosen to be much less than 2Δ. Thus, the energy gap of the superconductor protects the qubit from quasiparticle decoherence.

If a junction has "pinhole" defects, where a few channels have $\tau \to 1$, then the energy gap will shrink to zero at $\delta = \pi$. However, only the flux qubit will be sensitive to quasiparticles produced at these defects since it operates near $\delta = \pi$. In contrast, the phase qubit always retains an energy gap of at least $\sqrt{2}\Delta$ around its operating point $\delta = \pi/2$ (see arrow in Fig. 10). We note this idea implies that a phase qubit can even be constructed from a microbridge junction, which has some channels[26] with $\tau = 1$. Although the phase qubit is completely insensitive to pinhole defects, this advantage is probably unimportant because Al-based tunnel junctions have oxide barriers of good quality.

Pinhole defects also change the Josephson potential away from the -cos δ form. This modification is typically unimportant because the deviation is smooth and can be accounted for by a small effective change in the critical current.

The concept that the energy gap Δ protects the junction from quasiparticle transitions suggests that superconductors with nonuniform gaps may not be suitable for qubits. Besides the obvious problem of conduction channels with zero gap, channels with a reduced gap may cause stray quasiparticles to be trapped at the junction. The high-T_c superconductors, with the gap suppressed to zero at certain crystal angles, are an obvious undesirable candidate. However, even Nb could be problematic since it has several oxides that have reduced or even zero gap. Nb based tri-layers may also be undesirable since the thin Al layer near the junction slightly reduces the gap around the junction. In contrast, Al may not have this difficulty since its gap *increases* with the incorporation of oxygen or other scattering defects. It is possible that these ideas explain why Nb-based qubits do not have coherence times as long as Al qubits[6, 10].

9. Summary

In summary, Josephson qubits are nonlinear resonators whose critical element is the nonlinear inductance of the Josephson junction. The three types of superconducting qubits, phase, flux, and charge, use this nonlinearity differently and produce qubit states from a cubic, quartic, and cosine potential, respectively.

To understand the origin and properties of the Josephson effect, we have first reviewed the BCS theory of superconductivity. The superconducting phase was explicitly shown to be a macroscopic property of the superconductor, whose classical and quantum behavior is determined by the external electrical circuit. After a review of quasiparticle and Josephson tunneling, we argued that a proper microscopic understanding of the junction could arise only from an exact solution of the Josephson effect.

This exact solution was derived by use of mesoscopic theory and quasiparticle bound states, where we showed that Josephson and quasiparticle tunneling can be understood from the energy of the bound states and their transitions, respectively. A semiclassical theory was used to calculate the transition rate for a finite DC voltage, with the predictions matching well that obtained from exact methods.

This picture of the Josephson junction allows a proper understanding of the Josephson qubit state. We argue that the gap of the superconductor strongly protects the junction from quasiparticle tunneling and its decoherence. We caution that an improper choice of materials might give decoherence from quasiparticles that are trapped at sites near the junction.

We believe a key to future success is understanding and improving this remarkable nonlinearity of the Josephson inductance. We hope that the picture given here of the Josephson effect will help researchers in their quest to make better superconducting qubits.

Acknowledgements

We thank C. Urbina, D. Esteve, M. Devoret, and V. Shumeiko for helpful discussions. This work is supported in part by the NSA under contract MOD709001.

References

[1] M. A. Nielsen and I. L. Chuang, *Quantum Computation and Quantum Information* (Cambridge University Press, Cambridge, 2000).
[2] Y. Nakamura, C. D. Chen, and J. S. Tsai, Phys. Rev. Lett. **79**, 2328 (1997).
[3] Y. Nakamura, Y. A. Pashkin, T. Yamamoto, and J. S. Tsai, Phys. Rev. Lett. **88**, 047901 (2002).
[4] D. Vion, A. Aassime, A. Cottet, P. Joyez, H. Pothier, C. Urbina, D. Esteve, and M. H. Devoret, Science **296**, 886 (2002).
[5] S. Han, Y. Yu, Xi Chu, S. Chu, and Z. Wang, Science **293**, 1457 (2001); Y. Yu, S. Han, X. Chu, S. Chu, and Z. Wang, Science **296**, 889 (2002).
[6] J. M. Martinis, S. Nam, J. Aumentado, and C. Urbina, Phys. Rev. Lett. **89**, 117901 (2002).
[7] I. Chiorescu, Y. Nakamura, C. J. P. M. Harmans, and J. E. Mooij, Science **299**, 1869 (2003).
[8] A.J. Berkley, H. Xu, R.C. Ramos, M.A. Gubrud, F.W. Strauch, P.R. Johnson, J.R. Anderson, A.J. Dragt, C.J. Lobb, and F.C.Wellstood, Science **300**, 1548 (2003).
[9] Yu. A. Pashkin, T. Yamamoto, O. Astafiev, Y. Nakamura, D. V. Averin, and J. S. Tsai, Nature **421**, 823 (2003).
[10] R. W. Simmonds, K. M. Lang, D. A. Hite, D. P. Pappas, and J. M. Martinis, submitted to Phys. Rev. Lett.
[11] M.H. Devoret, *Quantum Fluctuations in Electrical Circuits*, in "Fluctuations Quantiques", Elsevier Science (1997).
[12] M. Steffen, J. M. Martinis, and I. L. Chuang, Phys. Rev. B **68**, 2245xx (2003).
[13] Audrey Cottet, Ph.D. thesis (2002).
[14] R. Rouse, S. Han, J. Lukens, Phys. Rev. Lett. **75**, 1614 (1995).
[15] R. Koch, private communication.
[16] J. E. Mooij, T. P. Orlando, L. Levitov, L. Tian, C. H. van der Wal, S. Lloyd, Science **285**, 1036 (1999)
[17] D. J. VanHarlingen, B. L. T. Plourde, T. L. Robertson, P. A Reichardt, and J. Clarke, Proceedings of the 3rd International Workshop on Quantum Computing, to be published.
[18] J. Bardeen, L. N. Cooper, and J. R. Schrieffer, Phys. Rev. **108**, 1175 (1957).
[19] P. W. Anderson, Phys. Rev. **112**, 1900 (1958).

[20] C. Kittel, *Quantum Theory of Solids*, John Wiley (1987).
[21] U. Eckern, G. Schon, V. Ambegaokar, Phys. Rev. B **30**, 6419 (1984).
[22] V. Ambegaokar and A. Baratoff, Phys. Rev. Lett. **11**, 104 (1963).
[23] C. W. J. Beenakker, Phys. Rev. Lett. **67**,3836 (1991).
[24] C. W. J. Beenakker, Rev. Mod. Phys. **69**, 731 (1997)
[25] Y. Naveh, Vijay Patel, D. V. Averin, K. K. Likharev, and J. E. Lukens, Phys. Rev. Lett. **85**, 5404 (2000).
[26] O. N. Dorokhov, JETP Lett. **36**, 318 (1982).
[27] K. M. Schep and G. E. W. Bauer, Phys. Rev. Lett. **78**, 3015 (1997).
[28] A. Furusaki and M. Tsukada, Physica B **165-166**, 967 (1990).
[29] S. V. Kuplevakhaskii and I. I. Fal'ko, Sov. J. Low Temp. Phys. **17**, 501 (1991).
[30] Our notation for incoming and outgoing states is choosen to correspond to the boundry conditions for scatttering in Ref. [32].
[31] D. Averin and A. Bardas, Phys. Rev. Lett. **75**, 1831 (1995).
[32] E. N. Bratus', V. S. Shumeiko, E. V. Bezuglyi, and G. Wendin, Phys. Rev. B **55**, 12666 (1997).
[33] E. N. Bratus, V. S. Shumeiko, and G. A. B. Wendin, Phys. Rev. Lett. **74**, 2110 (1995).
[34] K.M. Lang, S. Nam, J. Aumentado, C. Urbina, J. M. Martinis, IEEE Trans. on Appl. Supercon. **13**, 989 (2003).

Course 14

JOSEPHSON QUANTUM BITS BASED ON A COOPER PAIR BOX

Denis Vion

CEA-Saclay, Orme des merisiers,
91191 Gif sur Yvette Cedex , France

D. Estève, J.-M. Raimond and J. Dalibard, eds.
Les Houches, Session LXXIX, 2003
Quantum Entanglement and Information Processing
Intrication quantique et traitement de l'information

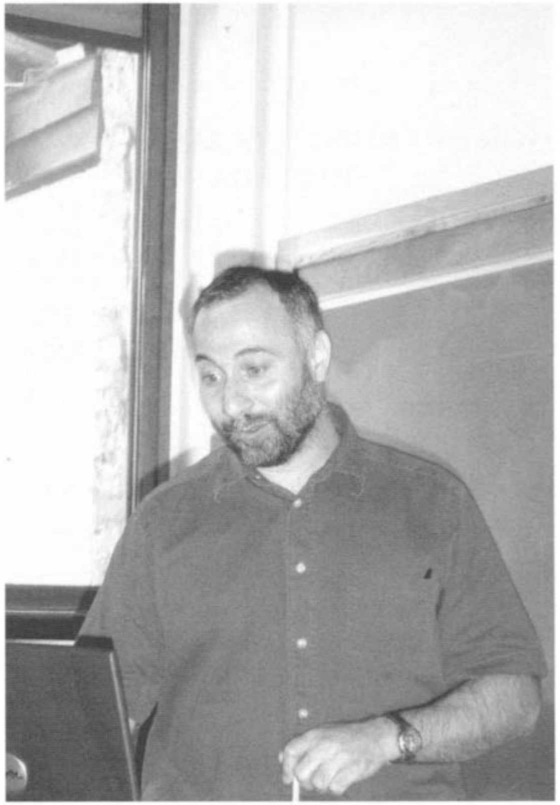

Contents

1. Introduction

The present chapter is devoted to a particular type of electrical circuit that has been used to develop solid state quantum bit prototypes. These circuits being superconducting and involving tunneling of Cooper pairs between two superconducting electrodes, they belong to the family of Josephson qubits previously introduced in this book [1]. They are all based on the same simple device, the Cooper pair box (CPB), and are all driven by a gate electrode coupled to the charge of a small electrode. For that reason, they are often considered as forming the so-called "charge qubits" sub-family, although they essentially share the same physics with other Josephson qubits [2, 3]: their quantum state can be easily manipulated, whereas reading this state out with a high efficiency is a difficult task. Moreover, preserving their quantum coherence is a challenge (even at ultra low temperature) due to their "macroscopic" character.

This chapter is organized in six sections. After this introduction, the second section presents the Cooper pair box device in its basic version and in its improved version: the split CPB. The energy spectrum is derived as a function of the external parameters controlling the Hamiltonian and the physical properties of the corresponding eigenstates are pointed out. In the third section, we show how the two lowest energy eigenstates form a qubit, how this qubit can be manipulated with DC voltage pulses or resonant microwave pulses, and how it can be measured following various strategies. Three experiments that have demonstrated coherent control of the CPB state are also presented. Then, in section 4, we present a very simple approach to decoherence in CPBs. Considering a particular CPB device (the Quantronium) as an example, we list its different possible decoherence sources and we calculate the different physical quantities that characterize how coherence of its quantum state is lost. From these considerations, we infer design rules for Josephson qubits. Then, we present different experiments that have been used to measure the effective coherence time of a real device. Finally, we address in section 5 the problem of making a 2-qubit-gate with two capacitively coupled CPBs.

2. The Cooper pair box

2.1. The basic Cooper pair box circuit

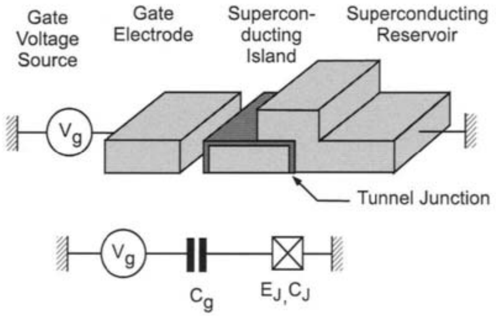

Fig. 1. *The basic Cooper pair box. Top: Schematic representation of the Cooper pair box showing the superconducting island and reservoir, the Josephson junction with energy E_J and capacitance C_J, the gate, and the voltage source V_g. Bottom: Corresponding electrical schematic drawing.*

The basic Cooper pair box (CPB) is the simplest device which combines Josephson [4] and Coulomb blockade effects [5]. It is a simplified version of a Josephson device proposed in 1987 [6], and consists [7] of a small BCS superconducting electrode, called the island, connected to a BCS superconducting reservoir by a Josephson junction with capacitance C_J and Josephson energy E_J. The island can be biased by a voltage source V_g in series with a gate capacitance C_g (see Fig. 1). In addition to E_J, the box has a second characteristic energy, the Coulomb energy E_C of a single Cooper Pair in excess in the island, with respect to electrical neutrality:

$$E_C = \frac{(2e)^2}{2C_\Sigma}, \tag{2.1}$$

where $C_\Sigma = C_g + C_J$ is the total capacitance of the island and e the electron charge. CPBs fabricated by conventional electron beam lithography having a capacitance C_Σ in the fF range (typical size of the junctions is 100nm × 100nm), E_C is typically of order of a few $k_B K$ (k_B is the Boltzmann constant). When the thermal energy $k_B T$ is reduced much below the BCS superconducting energy gap Δ of the electrodes, and when $E_C < 4\Delta$, all the electrons in the island and in the reservoirs are paired [8]. The Cooper pairs can tunnel through the Josephson junction and the only remaining degree of freedom of the system is the integer number **N** of Cooper pairs in excess or deficit on the island. Due to tunneling, **N** fluctuates quantum mechanically and has to be treated as an operator $\widehat{\mathbf{N}}$, whose eigenstates $|\mathbf{N}\rangle_c$ (index c stands for "pure charge") obey

$$\widehat{\mathbf{N}}\,|\mathbf{N}\rangle_c = \mathbf{N}\,|\mathbf{N}\rangle_c\,,\ \mathbf{N} \in \mathbb{Z}$$

and form a complete basis for the quantum states of the box.

Introducing the operator $\widehat{\theta}$ conjugated to $\widehat{\mathbf{N}}$ by the dimensionless relationship $[\widehat{\theta}, \widehat{\mathbf{N}}] = \mathbf{i}$, one defines the variable $\theta \in [0, 2\pi[$, which is the phase of the Cooper pair condensate in the island. From the conjugation relationship, one deduces the effect of the operators $\exp(\mathbf{i}\widehat{\theta})$ and $\exp(-\mathbf{i}\widehat{\theta})$ on charge states:

$$\exp(\pm\mathbf{i}\widehat{\theta})\,|\mathbf{N}\rangle_c = |\mathbf{N} \pm 1\rangle_c\,. \tag{2.2}$$

The Hamiltonian of the CPB can now be expressed as a function of the $\widehat{\mathbf{N}}$ and/or $\widehat{\theta}$ operators.

2.2. Hamiltonian and energy spectrum

The Hamiltonian of the whole CPB circuit (including its voltage source) is written:

$$\widehat{H}(N_g) = \widehat{H}_{el} + \widehat{H}_J = E_C(\widehat{\mathbf{N}} - N_g)^2 - E_J \cos\widehat{\theta}\,, \tag{2.3}$$

where the first term corresponds to the electrostatic energy of the circuit, $N_g = C_g V_g/(2e)$ being the reduced gate charge, and where the second term accounts for the energy cost of a phase difference θ across the Josephson junction and is responsible for the tunneling of Cooper pairs. In order to find the eigenenergies and the corresponding eigenstates of the system, (2.3) is rewritten in a form involving only $\mathbf{N}$ or only θ. Using (2.2), one finds the Hamiltonian in the charge representation,

$$\widehat{H} = \sum_{\mathbf{N}\in\mathbb{Z}} \left[E_C(\mathbf{N} - N_g)^2\, |\mathbf{N}\rangle_c\, \langle\mathbf{N}|_c - \frac{E_J}{2}(|\mathbf{N}\rangle_c\, \langle\mathbf{N}+\mathbf{1}|_c + |\mathbf{N}+\mathbf{1}\rangle_c\, \langle\mathbf{N}|_c) \right]. \tag{2.4}$$

The energy spectrum associated to this Hamiltonian is discrete and periodic in N_g with period 1. We call $|k\rangle$ the energy eigenstates and E_k their associated energies sorted in increasing order, starting from $k = 0$ for the ground state:

$$\widehat{H}\,|k\rangle = E_k\,|k\rangle\,, k \in \mathbb{N}. \tag{2.5}$$

For a given N_g, the lowest energy eigenstates can be found in the charge representation by truncating the pure charge state basis and by diagonalizing a finite version of the matrix that corresponds to (2.4).

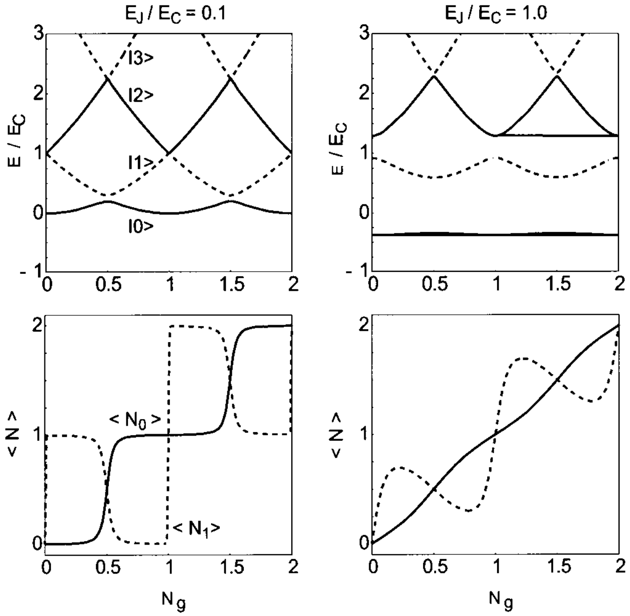

Fig. 2. Top: Energy levels of a Cooper pair box, normalized by the Cooper pair Coulomb energy E_C, as a function of the gate charge bias N_g, and for E_J/E_C ratios equal to 0.1 (left) and 1 (right). Bottom: Corresponding expectation values of the dimensionless box charges $\langle N\rangle$, for the energy eigenstates $|0\rangle$ (solid lines) and $|1\rangle$ (dotted lines).

Using $\widehat{\mathbf{N}} = (\mathbf{1}/\mathbf{i})\partial/\partial\theta$ in (2.3), one instead obtains the Hamiltonian in the phase representation and the Schrödinger equation for the $\Psi_k(\theta) = \langle\theta\,|k\rangle$ wavefunctions:

$$E_C(\frac{1}{\mathbf{i}}\frac{\partial}{\partial\theta} - N_g)^2\Psi_k(\theta) - E_J\cos(\theta)\Psi_k(\theta) = E_k\Psi_k(\theta)\,. \tag{2.6}$$

Both representations can of course be used equivalently to find the energy spectrum, which depends on N_g and on the E_J/E_C ratio, as shown on Fig. 2. When $E_J/E_C \ll 1$, the energy levels are very close to the electrostatic energies, except in the vicinity of the so-called charge degeneracy points defined by $N_g = 1/2\,(\mathrm{mod}\,1)$, where the degeneracy between the two lowest energy charge states is lifted up by an amount E_J. With increasing E_J/E_C, the modulation by N_g of the lowest eigenenergies becomes weaker and weaker.

It is interesting to note that except for precise combinations of E_J/E_C and N_g values, the energy spectrum of a CPB is highly anharmonic. Consequently, manipulating $|0\rangle$ and $|1\rangle$ without exciting higher energy states is possible. These two states are thus regarded as defining a qubit. We now compute explicitly the $|0\rangle$ and $|1\rangle$ states in order to evaluate their physical properties, which will be used to measure the quantum bit state.

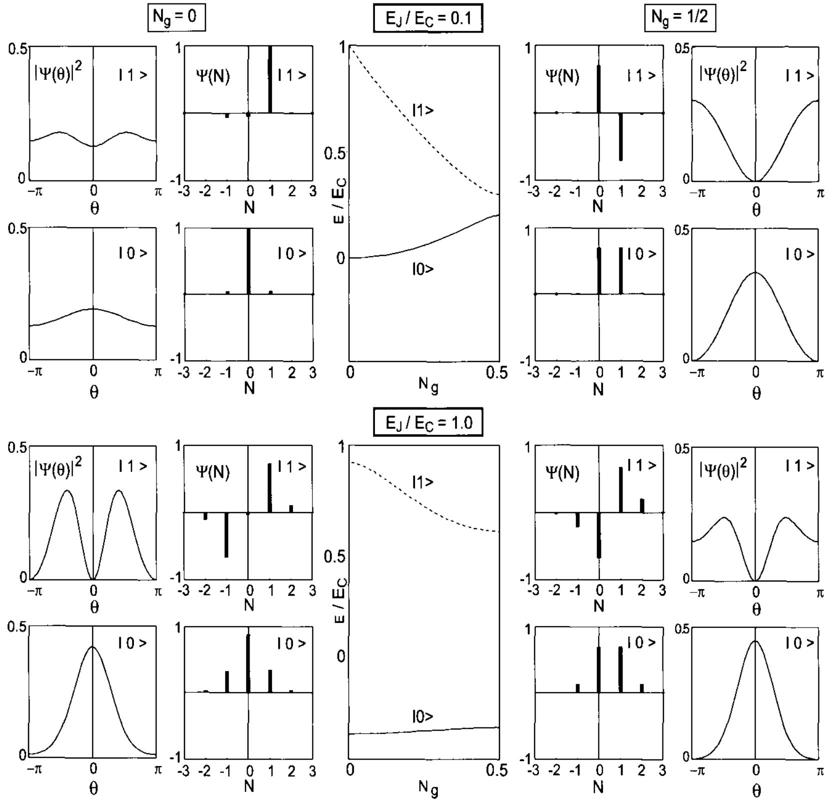

Fig. 3. Eigenenergies (middle panels) and wavefunctions of the $|0\rangle$ and $|1\rangle$ states in the charge and phase representations, for $N_g = 0$ (left panels) and for $N_g = 1/2$ (right panels), and for E_J/E_C ratios equal to 0.1 (top panels) and 1 (bottom panels). The $\Psi_k(N)$ eigenvectors are directly represented since they can be chosen real, whereas the $\Psi_k(\theta)$ wavefunctions are represented by their modulus squared.

2.3. *Eigenstates in the charge and phase representations*

Over an N_g period like the interval [0, 1] and for $E_J/E_C < 2$, the energy eigenstates $|k\rangle = \sum_{\mathbf{N}\in\mathbb{Z}} a_{kN} \, |\mathbf{N}\rangle_c$ can be found with a high accuracy by simply diagonalizing a matrix (2.4) truncated to only seven charge states. The corresponding $\Psi_k(\theta)$ functions can be found by Fourier transform of the $|k\rangle$'s expressed in the charge representation or by solving directly the Schrödinger equation (2.6). This equation is close to a Mathieu equation and its solutions are [9]

$$\left\{ \begin{array}{l} E_k = E_C \mathcal{M}_A(k+1-(k+1)/4[\mathrm{mod}\ 2] + 2n_g(-1)^k, q) \\ \Psi_k(\theta) = \frac{\exp(\mathrm{i}N_g\theta)}{\sqrt{2\pi}}[\mathcal{M}_C(a,q,\frac{\theta}{2}) + \mathbf{i}(-1)^{k+1}\mathcal{M}_S(a,q,\frac{\theta}{2})] \end{array} \right. , \tag{2.7}$$

where $a = 4E_k/E_C$, $q = -2E_J/E_C$, $\mathcal{M}_C$ and $\mathcal{M}_S$ are the even and odd Mathieu functions, and $\mathcal{M}_A$ is the function giving the characteristic values of $\mathcal{M}_C$. Figure 3 shows the two lowest stationary states $|0\rangle$ and $|1\rangle$ both in the charge and phase representations, for $N_g = 0$ and $N_g = 1/2$, and for two different E_J/E_C ratios. For $E_J/E_C \ll 1$, the situation is rather simple since $|0\rangle$ and $|1\rangle$ are very close to the pure charge states $|\mathbf{0}\rangle_c$ or $|\mathbf{1}\rangle_c$ at $N_g \simeq 0$, and correspond to the symmetric and antisymmetric superpositions of these charge states at $N_g = 1/2$. In this limit, it is useful to restrict the basis to $(|\mathbf{0}\rangle_c\,, |\mathbf{1}\rangle_c)$, so that the Hamiltonian looks like that for a spin 1/2 (like any other two-level-system [10]), after dropping out a constant term that depends on N_g only:

$$\widehat{H} = -\frac{1}{2}\vec{\sigma}.\vec{H}\,, \tag{2.8}$$

where $\vec{\sigma} = \hat{\sigma}_x\vec{x} + \hat{\sigma}_y\vec{y} + \hat{\sigma}_z\vec{z}$ is the vector of Pauli matrices and $\vec{H} = E_J\vec{x} + E_C(1-2N_g)\vec{z}$. Introducing the angle $\alpha = \arctan\left[E_J/\left\{E_C(1-2N_g)\right\}\right]$, the eigenenergies and the eigenstates are in this case $\mp E_J\sqrt{1+\cot^2\alpha}$ and

$$\left\{ \begin{array}{l} |0\rangle = \cos(\alpha/2)\,|\mathbf{0}\rangle_c + \sin(\alpha/2)\,|\mathbf{1}\rangle_c \\ |1\rangle = -\sin(\alpha/2)\,|\mathbf{0}\rangle_c + \cos(\alpha/2)\,|\mathbf{1}\rangle_c \end{array} \right. , \tag{2.9}$$

respectively. For $E_J/E_C \sim 1$, the $|0\rangle$ and $|1\rangle$ states are, for any N_g, made up of coherent superpositions with significant contributions from at least three or four pure charge states (see Fig. 3), so that neither θ nor **N** are "good quantum numbers".

2.4. *Expectation value of the box charge*

The expectation value of the charge on the island or its dimensionless equivalent $\langle N_k\rangle = \langle k|\,\widehat{\mathbf{N}}\,|k\rangle$ is an interesting quantity which can be used to discriminate

$|0\rangle$ from $|1\rangle$, and thus to read out a CPB-based-qubit. It depends linearly on the derivative of the energy levels with respect to N_g:

$$\frac{\partial \hat{H}}{\partial N_g} = 2E_C(N_g - \widehat{\mathbf{N}}) \Longrightarrow \langle N_k \rangle = N_g - \frac{1}{2E_C}\frac{\partial E_k}{\partial N_g} . \tag{2.10}$$

It is plotted in Fig. 2 for the two regimes already considered. For $E_J/E_C \ll 1$ and close to half integer values of N_g, $\langle N_0 \rangle$ and $\langle N_1 \rangle$ vary as opposite rounded staircases. Within the two charge states approximation, one deduces from (2.9) the shape of the steps for $N_g \in [0, 1]$: $\langle N_0 \rangle = \sin^2 \alpha/2$ and $\langle N_1 \rangle = \cos^2 \alpha/2$. When E_J/E_C is increased, the steps are more and more rounded and have to be calculated numerically. It is important to note that the difference $\Delta N_{10} = \langle N_1 \rangle - \langle N_0 \rangle$ vanishes at the charge degeneracy points.

2.5. *The split Cooper pair box*

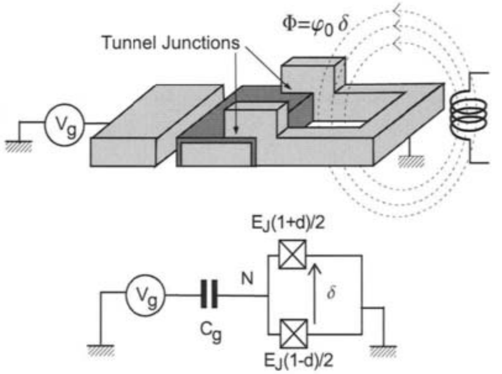

Fig. 4. *The split Cooper pair box. Top: Schematic representation showing the island, the two Josephson junctions connected to form a grounded superconducting loop, the gate circuit, and the magnetic flux bias. Bottom: Corresponding electrical drawing.*

The split Cooper pair box is an improved CPB with a tunable Josephson energy and a second access port. It is obtained by splitting its Josephson junction into two junctions with respective Josephson energies $E_J(1 + d)/2$ and $E_J(1 - d)/2$, where $d \in [0, 1]$ is an asymmetry coefficient (see Fig. 4). These two junctions are connected together to form a superconducting loop which can be biased by a magnetic flux Φ. Notice that the split CPB is similar to another Josephson device, the Bloch transistor [11] (also called the single Cooper pair transistor) that was first described in 1985. The split box has two degrees of freedom, which can be chosen either as the phase differences $\widehat{\delta}_1$ and $\widehat{\delta}_2$ across each junction, or as the linear forms $\widehat{\theta} = (\widehat{\delta}_1 - \widehat{\delta}_2)/2$ and $\widehat{\delta} = \widehat{\delta}_1 + \widehat{\delta}_2$, which represent the phase of the island introduced previously and the phase difference across the series combination of the two junctions, respectively. The conjugate variable of $\widehat{\delta}$ is the integer number K of Cooper pairs which tunneled through both junctions.

The electrostatic "Hamiltonian" of the split CPB is that of a basic box [see (2.3)] with C_J representing now the sum of the two junction capacitances. Its Josephson "Hamiltonian" is the sum of the Josephson terms of the two junctions:

$$\widehat{H}_J^* = -E_J\frac{1+d}{2}\cos(\widehat{\delta}_1) - E_J\frac{1-d}{2}\cos(\widehat{\delta}_2) \tag{2.11}$$

$$= -E_J\cos(\frac{\widehat{\delta}}{2})\cos(\widehat{\theta}) + dE_J\sin(\frac{\widehat{\delta}}{2})\sin(\widehat{\theta}) . \tag{2.12}$$

The superconducting loop of a split CPB is designed such that its self inductance L is very small compared to the junction inductance $L_J = \varphi_0^2/E_J$, with $\varphi_0 = \hbar/2e$. Consequently, the magnetic potential energy term $\left(\varphi_0\hat{\delta} - \Phi\right)^2/2L$ attached to this inductance strongly fixes δ, which can be considered as a classical parameter $\delta = \Phi/\varphi_0$ imposed by the magnetic flux. Finally, the Hamiltonian of the split box is

$$\widehat{H}(N_g, \delta) = E_C(\widehat{\mathbf{N}} - N_g)^2 - E_J^*(d, \delta)\cos[\widehat{\theta} + \Upsilon(d, \delta)] , \tag{2.13}$$

with [12]:

$$\begin{aligned} &E_J^*(d, \delta) = E_J\sqrt{\tfrac{1+d^2+(1-d^2)\cos(\delta)}{2}} \\ &\tan \Upsilon(d, \delta) = -d\tan(\tfrac{\delta}{2}) . \end{aligned} \tag{2.14}$$

A symmetric or almost symmetric ($d \approx 0$) split CPB is thus equivalent to a basic CPB but with a magnetostatically tunable [7] Josephson energy $E_J^* = E_J\cos(\delta/2)$. Its energy spectrum (see Fig. 5) is periodic in N_g (period 1) and 2π-periodic in δ, and can now be tuned by both the electric field applied to the gate electrode and by the magnetic flux threading the superconducting loop. For that reason, the split CPB has often been presented as a kind of artificial atom showing strong Stark and Zeeman effects.

Splitting the box has also a second interest: it opens a second access port to the device, which can be used to read out its quantum state [13–15]. The quantity to be measured on this port is the persistent current in the superconducting loop, its phase equivalent across the loop inductance, or the magnetic flux it produces. This persistent current is calculated below.

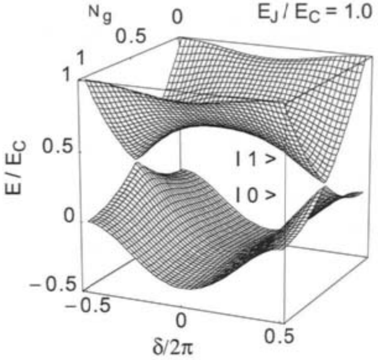

Fig. 5. Two lowest energy levels of a split Cooper pair box with $E_J/E_C = 1$, as a function of the two external parameters N_g and δ. The energy is normalized by the Cooper pair Coulomb energy E_C. The asymmetry coefficient $d = 2\%$ chosen here lifts up an energy degeneracy at $(N_g = 1/2, \delta = \pm\pi)$.

2.6. *Expectation value of the persistent current in the split box*

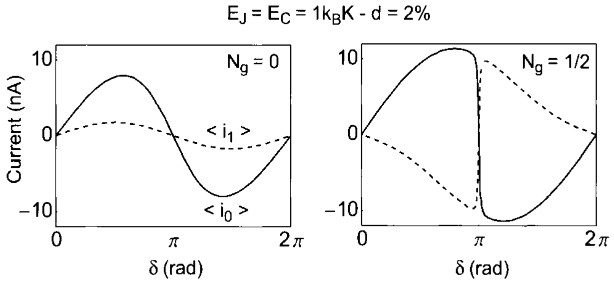

Fig. 6. Expectation value of the persistent loop currents $\langle i_0 \rangle$ for the ground state (solid line), and $\langle i_1 \rangle$ for the first excited state (dotted line), calculated for $E_C = E_J = 1\ k_B\text{K}$, $d = 2\%$, $N_g = 0$ (left panel) and $N_g = 1/2$ (right panel).

The $\widehat{\delta}$ and $\widehat{K}$ operators being conjugate to each other, the operator associated to the current circulating in the loop of the split CPB is

$$\widehat{I} = (-2e)\frac{d\widehat{K}}{dt} = (-2e)\left(-\frac{1}{\hbar}\frac{\partial \widehat{H}}{\partial \delta}\right) . \tag{2.15}$$

The average loop current $\langle i_k \rangle$ of state $|k\rangle$ follows thus the generalized Josephson

relation

$$\left\langle i_k(N_g, \delta)\right\rangle = \left\langle k\left|\widehat{I}\right|k\right\rangle = \frac{1}{\varphi_0}\frac{\partial E_k(N_g, \delta)}{\partial \delta} . \tag{2.16}$$

Like the energy spectrum, $\langle i_k \rangle$ currents are also 2π-periodic in δ and 1-periodic in N_g, the extrema of $\langle i_0 \rangle$ and $\langle i_1 \rangle$ being of the order of E_J/φ_0. Also, for N_g close to 1/2 and $E_J < 3E_c$, $\langle i_0 \rangle$ and $\langle i_1 \rangle$ have opposite signs, as shown in Fig. 6. Note that the difference $\Delta i_{10} = \langle i_1 \rangle - \langle i_0 \rangle$ vanishes at $\delta = 0$ for all N_g.

Given the physical properties of the $|0\rangle$ and $|1\rangle$ CPB's states, we can now consider the different strategies for implementing, for driving and for reading a qubit based on these states.

3. The Cooper pair box as a quantum bit

As previously mentioned, the two orthogonal states chosen to define a CPB-based-qubit are its two lowest energy eigenstates $|0\rangle$ and $|1\rangle$. By varying N_g, the quantum state of the box can be manipulated within this subspace, provided that the temperature is sufficiently low, that the N_g excursion is limited, and that the anharmonicity of the energy spectrum is large enough. To implement a qubit, the CPB has also to be coupled to a readout device able to discriminate its two states at a certain measuring point $\left(N_{gm}, \delta_m\right)$ in the space of the external parameters controlling its Hamiltonian. We consider here the case of a coupling between the box and its readout, weak enough so that it does not modify significantly the $|0\rangle$ and $|1\rangle$ states of the uncoupled box. When all these conditions are fulfilled, the CPB can be regarded as a fictitious dimensionless spin 1/2, $\vec{\sigma}$, with a Hamiltonian

$$\widehat{H}\left(N_g, \delta\right) = -\frac{1}{2}\vec{\sigma}.\vec{H}\left(N_g, \delta\right) . \tag{3.1}$$

This Hamiltonian can be expressed in any frame $R\{\vec{x}, \vec{y}, \vec{z}\}$ defined by

$$\left\{ \begin{array}{c} \vec{H}\left(N_{g0}, \delta_0\right) = h\nu_{01}\left(N_{g0}, \delta_0\right)\vec{z}\left(N_{g0}, \delta_0\right) \\ \partial\vec{H}/\partial N_g.\vec{y} = 0 \end{array} \right. , \tag{3.2}$$

where $\nu_{01}\left(N_g, \delta\right)$ is the transition frequency between $|0\rangle$ and $|1\rangle$ and $\left(N_{g0}, \delta_0\right)$ is a particular point in the parameter space. Note that the frame introduced with (2.8) when $E_J/E_C \ll 1$ is a limit case, for which the reference states $|\mathbf{0}\rangle_c$ and $|\mathbf{1}\rangle_c$ are almost equal to $|0\rangle$ and $|1\rangle$ for N_{g0} far away from the charge degeneracy point. The time variation of the spin state can be visualized in the so-called Bloch sphere picture, where the general quantum state

$$\cos(\theta_u/2)\exp(-\mathbf{i}\varphi_u/2)\,|0\rangle + \sin(\theta_u/2)\exp(\mathbf{i}\varphi_u/2)\,|1\rangle\ , \tag{3.3}$$

is represented by a vector with polar coordinates θ_u and φ_u, precessing around $\vec{H}$ with a frequency $|\vec{H}|/h$. We now consider the different ways of modifying $\vec{H}$ in order to manipulate $\vec{\sigma}$.

3.1. Manipulation of the Cooper pair box quantum state

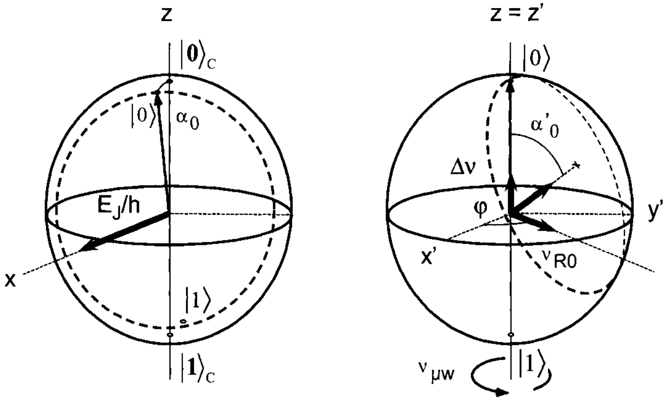

Fig. 7. Bloch sphere representations showing how the CPB state has been manipulated in two different types of experiments. The left sphere with two adjacent pure charge states at the north and south poles corresponds to a CPB with $E_J/E_C << 1$, which is driven to the charge degeneracy point with a fast dc gate pulse. The right sphere with energy eigenstates at the poles describes within the rotating wave approximation how a CPB is driven with microwave voltage pulses (see text for detailed explanation). The spin is represented by a thin arrow whereas fields are represented by bold arrows. The dotted lines show the spin trajectory, starting from the ground state.

3.1.1. Constant perturbation applied suddenly to the Hamiltonian

The first method that was used experimentally in 1999 [16] to prepare a CPB-based-qubit in a coherent quantum superposition of its 2 states consists in applying to its gate (or to a second gate specially designed for that purpose) a trapezoidal N_g pulse with rise and fall times much shorter than $1/\nu_{01}$. This method was implemented on CPBs with $E_J/E_C \ll 1$, the gate charge being initially tuned at a value N_g of the order of 0.3 during a time long enough so that the qubit has relaxed to its ground state $|0\rangle \simeq |\mathbf{0}\rangle_c$. On the Bloch sphere drawn in the pure charge state referential (see left panel of Fig. 7), the initial situation corresponds to the spin parallel to the vector $\vec{H} = E_J\vec{x} + E_C(1 - 2N_g)\vec{z}$, the latter making a small angle $\alpha_0 \sim E_J/E_C(1 - 2N_g) \ll 1$ with $\vec{z}$. Then N_g is brought suddenly to $N_{g0} = 1/2$ in a time so short that the evolution of the spin during this transition is negligible. Now $\vec{H} = E_J\vec{x}$ induces the Rabi precession of the spin around the x axis at the Rabi frequency

$$\nu_{Rabi} = E_J/h\,. \tag{3.4}$$

After a time t, the coherent superposition that is built has a weight $\cos^2\alpha_0 \cdot \sin^2\nu_{Rabi}t$ on $|\mathbf{1}\rangle_c$. N_g is then brought back suddenly to its initial value. The qubit precesses then around the initial $\vec{H}$ and can be measured (see section 3.2) in the $(|\mathbf{0}\rangle_c\,, |\mathbf{1}\rangle_c) \approx (|0\rangle\,, |1\rangle)$ basis. Any superposition state, i.e. any point on the Bloch sphere can thus be reached in a time shorter than $[E_J/2 + E_C(1 - 2N_g)]/h$, by applying first a single pulse and by waiting then during a precise time. Besides, it is interesting to notice (the result will be used in section 5) that if $\Delta N_g = N_{g0} - 1/2 \neq 0$, the maximum probability to measure the qubit in state $|\mathbf{1}\rangle_c$ after a single pulse is strongly reduced as

$$\frac{1}{1 + \left(2E_C\Delta N_g/E_J\right)^2}\,. \tag{3.5}$$

The present driving method has been used successfully by two research groups [16, 17]. It has the great advantage of inducing fast Rabi oscillations that can be observed even if the coherence time is rather short. On the other hand, one needs a very fast pulse generator with rise and fall times well below 100 ps. An alternative to this method is to use a harmonic perturbation.

3.1.2. Harmonic perturbation applied to the Hamiltonian

A second way to build superposed states is to apply a small resonant or almost resonant harmonic perturbation to the spin following the techniques developed in atomic physics and in Nuclear Magnetic Resonance. More precisely, a microwave pulse $\Delta N_g \cos(2\pi\nu_{\mu w}t + \varphi)$, with $\nu_{\mu w} \approx \nu_{01}$, is added to the DC gate voltage and introduces in the Hamiltonian (2.13) a perturbation, which is written in the spin formalism as:

$$\vec{H}_{ex} = 4E_C\Delta N_g \cos(2\pi\nu_{\mu w}t + \varphi)\left[\langle 1|\,\widehat{N}\,|0\rangle\,\vec{x} \,+ \Delta N_{10}\vec{z}\right]. \tag{3.6}$$

When $\nu_{\mu w}$ is close to ν_{01}, the effect of the longitudinal part $\vec{H}_{ex}.\vec{z}$ on the motion of $\vec{\sigma}$ can be neglected. Moreover the CPB is usually operated at the charge degeneracy point (see section 2) where $\Delta N_{10} = 0$, so that $\vec{H}_{ex}.\vec{z} = 0$. We are thus left with the transverse perturbation whose effect on $\vec{\sigma}$ is simpler to describe in a frame $R'\{\vec{x}', \vec{y}', \vec{z}'\}$ rotating at the frequency $\nu_{\mu w}$ around $\vec{z}' = \vec{z}$. Within the so-called rotating wave approximation [18], the free Hamiltonian and the perturbation correspond in R' to:

$$\vec{H} = h\Delta\nu\,\vec{z}' \text{ with } \Delta\nu = \nu_{01} - \nu_{\mu w} \tag{3.7}$$

$$\vec{H}_{ex} \simeq h\nu_{R0}\left[\vec{x}'\cos\varphi + \vec{y}'\sin\varphi\right] \text{ with } \nu_{R0} = 2E_C\Delta N_g\,\langle 1|\,\widehat{N}\,|0\rangle\,/h\,. \tag{3.8}$$

When no microwave signal is applied to the gate, $\vec{\sigma}$ precesses freely in R' around $\vec{z}'$ at the detuning frequency $\Delta\nu$, whereas during microwave pulses, it precesses around $\vec{H} + \vec{H}_{ex}$ (see right panel of Fig. 7) at the Rabi frequency

$$\nu_{Rabi} = \nu_{R0}\sqrt{1 + \left(\frac{\Delta\nu}{\nu_{R0}}\right)^2} ,$$

which is proportional to the dimensionless microwave amplitude ΔN_g when detuning $\Delta\nu$ is chosen well below ν_{R0}. Starting from $|0\rangle$, the probability to measure $|1\rangle$ after a single pulse with effective duration t is thus $\cos^2\alpha_0' \sin^2 \nu_{Rabi}t$, with $\tan\left(\alpha_0'\right) = \nu_{R0}/\Delta\nu$. Note that the rise and fall time of the microwave pulses do not need to be short and that the precession axis and the Rabi frequency are tunable through the three parameters ΔN_g, $\nu_{\mu w}$, and φ. Moreover, any single qubit gate (i.e. any rotator operating on the Bloch sphere) can be implemented with a sequence of resonant pulses along $\vec{x}'$ and $\vec{y}'$ only [19], and all the tricks developed in NMR like composite pulse techniques [18] are applicable. This microwave driving method has been successfully applied to a split box [20] with $E_J/E_C \sim 1$, and also to phase [2] and flux [3] Josephson qubits.

3.1.3. Adiabatic acceleration

Finally, we also mention here an alternative way to perform a rotation around $\vec{z}'$, using a technique transposed from the "Stark pulse technique" known in atomic physics [21]. It consists, starting from a freely evolving superposed state

$$a\,|0\rangle + b\exp\left[2\pi\nu_{01}\left(Ng_0, \delta_0\right)t\right]|1\rangle ,$$

in applying a closed adiabatic variation of the external parameters N_g and δ away from and back to the working point $\left(N_{g0}, \delta_0\right)$ in order to decrease or increase temporarily the deterministic relative dephasing speed $2\pi\nu_{01}\left(N_g, \delta\right)$ between components $|0\rangle\left(N_g, \delta\right)$ and $|1\rangle\left(N_g, \delta\right)$, without changing their weights. This method has been successfully tested with the split box mentioned above by moving adiabatically N_g away from and back to $\left(N_{g0} = 1/2, \delta_0 = 0\right)$ along the bold line of Fig. 12.

3.2. Readout of Cooper pair box quantum states

Many different strategies [13–16,22–24,26,27] have been proposed to distinguish the $|0\rangle$ and $|1\rangle$ states of a CPB. For some of them, the readout is coupled to the box charge whereas for others, it is coupled directly or indirectly to the δ phase degree of freedom of a split box. In all cases, an important distinction is whether the readout device is designed to perform a projective measurement onto some $|0\rangle'$ and $|1\rangle'$ states close to $|0\rangle$ and $|1\rangle$, or if it designed to perform a non projective measurement involving a relaxation process of the box from $|1\rangle$ to $|0\rangle$. A second characteristic is whether the readout is designed to be switched off during the box manipulation and then switched on to measure it with a signal to noise ratio larger than 1 in a single shot, or if it is designed to measure continuously a box which is periodically prepared in the same coherent state, so that the signal becomes detectable only after many repetitions. Although almost all possibilities have been considered in theoretical proposals, we describe below only the methods that have been really implemented experimentally. A last important property that will be considered in section 4 is the back-action that the readout induces onto the qubit and that can limit its coherence time.

3.2.1. Box charge used to build a current through an additional tunnel junction

At a time when no ultrasensitive electrometer would have been fast enough to discriminate the average charges $\langle N_1\rangle$ and $\langle N_0\rangle$ of a CPB-based-qubit in a time shorter than its relaxation time, Y. Nakamura and co-workers added to a split CPB with $E_J/E_C \ll 1$ a clever readout, which demonstrated in 1999 the first Rabi oscillations of an electrical circuit (see Fig. 8). A small and very opaque additional tunnel junction is connected to the island and biased with a voltage V such that an extra Cooper pair can enter the island and be broken into two electrons which then tunnel sequentially through the junction with rates Γ_{qp1} and Γ_{qp2} [16]. In the $|0\rangle$ state, this cyclic process gives rise to a finite current through the junction, the Josephson quasiparticle current (JQP) [28]. When the box is in its $|1\rangle$ state at $N_{g0} \sim 0.2 - 0.4$ with $\langle N_1\rangle \sim 1$, it relaxes to its $|0\rangle$ state with $\langle N_0\rangle \sim 0$ in a single JQP cycle with a relaxation rate Γ_{qp1}. By repeating rapidly the preparation of the $|1\rangle$ state, the JQP current can then be made larger than in the $|0\rangle$ state, the difference being used to measure the qubit state. Note that the coupling between the box and the readout being weak, the measured states are very close to $|0\rangle$ and $|1\rangle$, although the measurement is not projective and resets automatically the qubit to $|0\rangle$. This method is by design not single shot and the voltage V is applied continuously while the same preparation of the state is repeated, using the fast trapezoidal N_g pulse technique described in section 3.1.1.

3.2.2. Capacitive coupling to an electrometer

The most natural way for discriminating the two CPB states is to measure the expectation value $\langle N\rangle$ of its island charge by coupling it capacitively to an electrometer. The basic single electron transistor (SET) [5] was the first electrometer used to characterize the $|0\rangle$ state of a CPB by measuring the 2e periodic Coulomb staircase [7] mentioned in section 2.4. This device has a maximum bandwidth of a few kHz and is far from being fast enough to measure the $|1\rangle$ state before it relaxes to $|0\rangle$. A faster version of the SET, the RFSET, was invented in 1998 [25]

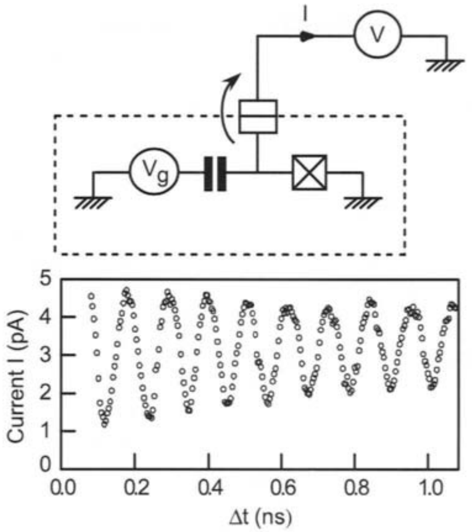

Fig. 8. First demonstration of quantum coherent control of an electrical circuit by Y. Nakamura et al. Top: simplified diagram of the setup, which includes a CPB and a readout made of a voltage biased additional opaque tunnel junction connected to the island. When fast DC pulses are applied repetitively to the CPB gate, the Josephson quasiparticle current I through the readout junction reflects the occupation probability of the CPB charge states $|\mathbf{0}\rangle_c$ and $|\mathbf{1}\rangle_c$ (see text). Bottom: Rabi oscillations of the CPB state measured by the variation of I. *Courtesy of Y. Nakamura et al., NEC, Japan.*

and was used by P. Delsing et al. [17] to measure a split CPB with $E_J/E_C \ll 1$, using the setup shown in Fig. 9. This RFSET includes a SET made up of an island defined by two tunnel junctions in series, biased with a voltage source. At DC voltages lower than or of the order of the Coulomb gap, the IV curve of the SET is modulated by the average charge of the CPB capacitively coupled to its island. By inserting the SET in parallel with the capacitance of a tank circuit that resonates in the radiofrequency domain and by applying a quasi-resonant RF signal to the ensemble, one measures a reflection coefficient that depends on the charge coupled to SET. The coupling between the RFSET and the CPB being weak, this readout is of the projective type. Besides, it can in principle be switched on and off with both the DC voltage and the RF input signal. Moreover, its sensitivity of the order of $10^{-5}e/\sqrt{Hz}$ is high enough and its back-action onto the qubit during the measurement is low enough that it can be operated in a single shot mode [27], provided that the qubit relaxation time is larger than or of order 1 μs. Unfortunately, at the time of writing (2003), it has proved difficult to measure a

CPB in this mode. Rabi oscillations [17] were demonstrated over a few nanoseconds with the fast trapezoidal N_g pulse technique and with the RFSET operated in the continuous mode (see Fig. 9).

An important point to notice is that a CPB-based-qubit measured through its average charge $\langle N\rangle$ is usually in the regime $E_J/E_C \ll 1$, for which the signal $\Delta N_{10} \sim 1$ is maximal as soon as $N_g \neq 1/2$. Consequently, its Coulomb energy E_C is rather high and its Hamiltonian is sensitive to any external charge fluctuations. It is well known that single charge devices like the CPB have always suffered from charged two-level-fluctuators, which play the role of additional noisy gate voltage sources and can thus induce decoherence of the qubit state (see section 4). It is thus interesting to increase E_J/E_C and to find an alternative to the measurement of $\langle N\rangle$.

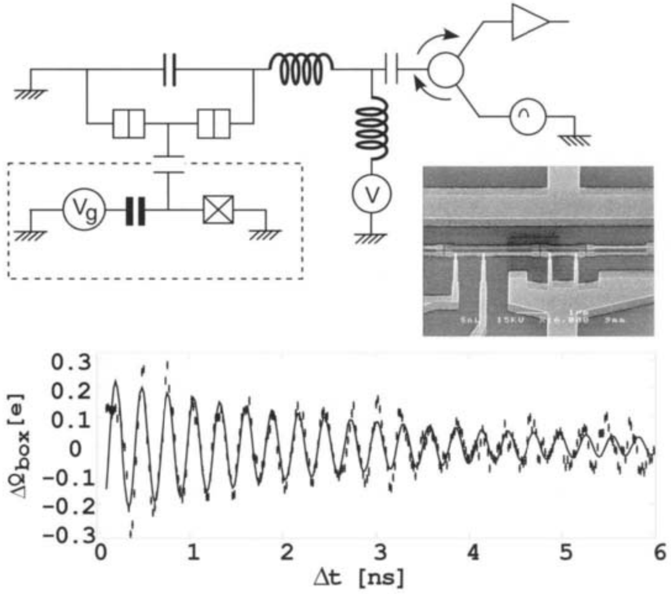

Fig. 9. Coherent control of a CPB by P. Delsing et al. Top: Simplified diagram of the setup showing that the CPB island is coupled capacitively to an RFSET, the RF reflecting power of which depends on the CPB average charge. Middle right: Scanning electron micrograph of the sample showing the SET on the left and the (split) box on the right. This sample was made by double angle shadow evaporation of aluminum through an e-beam patterned resist mask. Bottom: Rabi oscillations obtained with this readout, when applying repetitive fast DC pulses to the CPB gate. Here, ΔQ_{box} is the average charge on the box island. *Courtesy of the "Quantum Device Physics" group, Chalmers University of Technology, Göteborg, Sweden.*

3.2.3. Measurement of the split box persistent current: The Quantronium

A possible alternative to measurements of $\langle N \rangle$ consists in measuring the persistent current of a split box or the magnetic field it produces. For measuring the magnetic field, the superconducting loop of the split CPB can be coupled by mutual inductance to a SQUID or to a tank circuit whose effective inductance becomes different for the $|0\rangle$ and $|1\rangle$ CPB states, as proposed by A. Zorin et al. [14]. The latter technique is similar to that used for the RFSET and is currently under development.

We now describe the Quantronium, a setup proposed by D. Esteve [13] in order to discriminate the split box states directly through its loop persistent current. The circuit sketched in Fig. 10 consists of a split CPB with an additional current biased large Josephson junction with Josephson energy $E_{J0} \gg E_J$, inserted in the superconducting loop. During the manipulation of the qubit, the bias current I_b is kept small, so that the effective inductance of the additional junction is small and that the phase $\gamma = \arcsin(\varphi_0 I_b / E_{J0})$ across it behaves classically. The Quantronium is thus, during manipulation, a split box with $\delta = \Phi/\varphi_0 + \gamma$, the current biased junction playing only the role of an additional phase source for the split box. During the readout process, the additional junction is used to transfer adiabatically the information about the quantum state of the split box onto the phase γ, in analogy with the Stern & Gerlach experiment, where the spin state of a silver atom is entangled with its transverse position. For this transfer, a trapezoidal readout pulse $I_b(t)$ with a peak value slightly below the critical current $I_0 = E_{J0}/\varphi_0$ is applied to the circuit. Starting from $\delta = 0$, the phases $\langle \gamma \rangle$ and $\langle \delta \rangle$ grow during the current pulse and a state-dependent supercurrent develops in the loop. This current $\langle i \rangle$ adds algebraically to I_b in the large junction and modifies its switching rate Γ. By precisely adjusting the amplitude and duration of the $I_b(t)$ pulse, the large junction switches during the pulse to a finite voltage state with a large probability p_1 for state $|1\rangle$ and with a small probability p_0 for state $|0\rangle$ [13]. The switching of the large junction to the voltage state is then detected by measuring the voltage across it with an amplifier at room temperature. Although this measurement scheme is projective in a first step, it is nevertheless destructive due to the large amount of quasi particles produced when the voltage develops across the readout junction. Besides, it is designed to be single shot, its efficiency being expected to exceed $\eta = p_1 - p_0 = 95\%$ for a critical current $I_0 \sim 0.5 - 1\mu A$ and for the persistent currents plotted in Fig. 6. A Quantronium sample has been operated successfully (see Fig. 10) with the microwave N_g pulse technique, although the maximum overall efficiency of its readout was only $\eta \sim 20\%$. This sample has the longest coherence time observed so far (2004) in a Josephson qubit. The reasons for this success are analyzed in the next section devoted to decoherence of CPB-based- qubits.

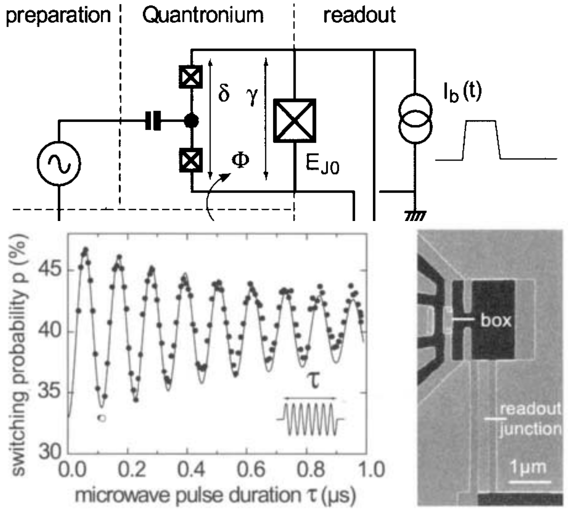

Fig. 10. Coherent control of a Quantroniun by the Quantronics group of CEA Saclay. Top: simplified diagram of the setup showing the readout Josephson junction inserted in the loop of a split box . A trapezoidal current pulse $I_b(t)$ is applied to this junction so that the latter switches out of its zero voltage state with a higher probability if the Quantronium is projected onto $|1\rangle$ than if it is projected onto $|0\rangle$. Bottom right: Scanning electron micrograph of a Quantronium made by double angle shadow evaporation of aluminum. Bottom left: Rabi oscillations obtained on a Quantronium with $E_J = 0.86 k_B K$ and $E_C = 0.68 k_B K$ when applying repetitively a resonant microwave pulse to the gate and a current pulse to the readout junction. Each experimental point is an average over 5×10^4 sequences.

4. Decoherence of Josephson charge qubits

4.1. Evaluation of decoherence: a simple approach

As with cany other quantum object, CPB-based-qubits are subject to decoherence due to their interaction with uncontrolled degrees of freedom present in their environment. From a general point of view, these interactions between the CPB and its environment entangle them in a complex way, which can be analyzed in principle by writing the total Hamiltonian of the system {CPB+environment} and by computing the evolution of the qubit reduced density matrix. Although this method has been used successfully for calculating decoherence induced by an RFSET [29] reading a CPB, it is in practice intractable in many cases. Moreover, it does not lead to analytical expressions showing directly the influence of each parameter and of each decoherence source, so that it is not always of great help for designing an experiment. Fortunately, decoherence during the free evolution of the qubit can be described in a much simpler way when the coupling between the qubit and its environment is weak. Indeed, an external parameter λ (such as N_g or δ) entering the Hamiltonian $\widehat{H} = -1/2\,\overrightarrow{\sigma} \cdot \overrightarrow{H}(\lambda)$ submitted to small quantum fluctuations from the external degrees of freedom can be treated as an operator of the environment. More precisely, each independent part X of the environment plays the role of an independent quantum noise source on the centered operator $\widehat{\lambda_0} = \widehat{\lambda} - \langle\lambda\rangle$. To first order, the coupling Hamiltonian between this source and the CPB is written

$$\widehat{H}_X = -1/2\left(\overrightarrow{D}_{\lambda} \cdot \overrightarrow{\sigma}\right)\widehat{\lambda}_0^X\,, \tag{4.1}$$

where $\overrightarrow{D}_{\lambda} \cdot \overrightarrow{\sigma}$ is the restriction of $-2\widehat{\partial H/\partial\lambda}$ to the $\{|0\rangle\,, |1\rangle\}$ space. Then, from the noise properties of each source X, one calculates separately three relevant quantities that characterize X-induced decoherence: the first two characterize the depolarization of the fictitious spin representing the qubit. They are the excitation $\Gamma_{\uparrow,X}$ and relaxation $\Gamma_{\downarrow,X}$ rates giving the probability per unit time of X-induced $|0\rangle \rightarrow |1\rangle$ and $|1\rangle \rightarrow |0\rangle$ transitions of the qubit, respectively. The third relevant quantity is the "dephasing function" $f_X(t) = \langle\exp[i\Delta\varphi_X(t)]\rangle$ involving the X-induced random dephasing $\Delta\varphi_X(t)$ between the two components of a superposed state $a(t)\,|0\rangle + b(t)\exp[i\Delta\varphi_X(t)]\,|1\rangle$ (note that $f_X(t)$ is not necessarily exponential and characterized by a rate). The evolution of the qubit density matrix is then easily deduced from the values of $\Gamma_{\uparrow,X}$, the values of $\Gamma_{\downarrow,X}$ and the $f_X(t)$ functions. Introducing the total dephasing function $F(t) = \prod_X f_X(t)$ and the total upward and downward rates $\Gamma_{\uparrow} = \sum_X \Gamma_{\uparrow,X}$ and $\Gamma_{\downarrow} = \sum_X \Gamma_{\downarrow,X}$, the diagonal elements evolve exponentially towards their equilibrium values $1 - \epsilon$ and $\epsilon = \Gamma_{\uparrow}/\Gamma_1$ with the characteristic rate $\Gamma_1 = \Gamma_{\uparrow} + \Gamma_{\downarrow}$, whereas off-diagonal elements decay as $F_2(t) = \exp[-\Gamma_1 t/2]F(t)$. In the next sections, we calculate explicitly $\Gamma_{\uparrow,X}$, $\Gamma_{\downarrow,X}$ and $f_X(t)$ for the main decoherence sources X , in the case when the noise $\widehat{\lambda}_0^X$ is Gaussian and can be fully characterized by a generalized quantum spectral density function of angular frequency ω [1]:

$$S_{\lambda_0}^X(\omega) = \frac{1}{2\pi}\int_{-\infty}^{+\infty} d\tau\left\langle\widehat{\lambda}_0^X(t)\widehat{\lambda}_0^X(t+\tau)\right\rangle\exp(-\mathbf{i}\omega\tau). \tag{4.2}$$

In this expression, the prefactor is chosen so that $S_{\lambda_0}^X(\omega)$ coincides in the classical limit and at low frequency with the spectral density of the engineer. Note that $S_{\lambda_0}^X(\omega)$ is defined for positive and negative ω's, the positive and negative parts being proportional to the number of environmental modes that can absorb and emit a quantum $\hbar\omega$, respectively.

4.2. Overview of decoherence sources in a CPB

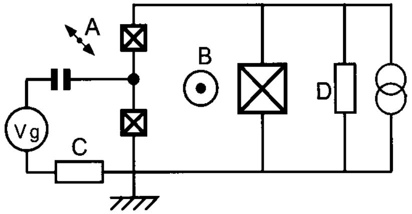

Fig. 11. Main decoherence sources in a Quantronium device. Quantum noise on N_g is generated by charged two-level-fluctuators (A) located near the CPB island and by voltage fluctuations of the series impedance (C) in the gate line. Quantum noise on δ is generated by fluctuations of the magnetic field (B) and by current fluctuations of the finite impedance (D) in parallel with the current bias source of the readout.

The uncontrolled degrees of freedom coupled to the idealized CPB of section 2 include those of the CPB substrate, those of the electrical lines of the driving and readout circuitry, and also the CPB's microscopic internal degrees of freedom which have been considered as frozen up to now. As an example, Fig. 11 shows the main decoherence sources in a Quantronium device (see section 3.2.3), which are now presented briefly.

Background charge noise First, microscopic charged two-level-fluctuators (A in Fig. 11) always present near the CPB island, either on the substrate or inside the Josephson junctions, are coupled to $\widehat{N}$ and act on the box as additional uncontrolled N_g sources. Although this background charge noise (BCN) is out of equilibrium and its generalized quantum spectral density is unknown, its classical spectral density $\widetilde{S}_{N_g,}^{BCN}(\omega) \sim B/|\omega|$ has been measured up to the MHz region, the values found for B being of order $10^{-7} - 10^{-9}$.

Impedance of the gate line The finite series impedance Z_g in the gate line (C in Fig. 11) can be regarded as an infinite collection of harmonic oscillators [1] also coupled to $\widehat{N}$ and inducing quantum noise on N_g. The circuit as seen from the pure Josephson element of the CPB (junction capacitance not included) is equivalent [9] to an effective gate capacitance C_Σ in series with a voltage source $\kappa_g V_g$ having an internal impedance Z_{eq}. In the weak coupling limit defined by $\kappa_g = C_g/C_\Sigma \ll 1$ and for all relevant frequencies, the real part of Z_{eq} is written:

$$\mathrm{Re}[Z_{eq}] \simeq \kappa_g^2 \,\mathrm{Re}[Z_g]\,. \tag{4.3}$$

At thermal equilibrium at temperature T, Z_{eq} generates voltage fluctuations whose spectral density S_u corresponds to N_g fluctuations with spectral density $S_{N_g}^{Z_g}$:

$$S_u = \frac{\hbar\omega}{2\pi}\left[1+\coth\left(\frac{\hbar\omega}{2k_BT}\right)\right]\mathrm{Re}[Z_{eq}], \tag{4.4}$$

$$S_{N_g}^{Z_g} = \left(\frac{C_\Sigma}{2e}\right)^2 S_u \simeq \kappa_g^2 \frac{\hbar^2\omega}{E_C^2}\left[1+\coth\left(\frac{\hbar\omega}{2k_BT}\right)\right]\frac{\mathrm{Re}[Z_g]}{R_k}\,, \tag{4.5}$$

where $R_k = h/e^2 \simeq 26k\Omega$.

Magnetic flux noise Fluctuations of the magnetic field threading the loop of a split CPB (B in Fig. 11), either due to the motion of vortices in the vicinity of the loop or more macroscopically due to the current noise in the wires producing the field, generate directly δ noise. When the noise source is a circuit inductively coupled to the loop, its spectral density can be easily derived following the same method as we follow below for calculating the back-action of a Quantronium readout.

Readout back-action For a CPB measured by an RFSET (see section 3.2.2), the stochastic tunneling of electrons into and out of the SET island generates quantum noise on N_g. The reader can refer to [27, 29] for a characterization of this noise. For the Quantronium, the back-action of the readout circuit is the quantum noise on δ induced by the finite admittance Y_R in parallel with its current source (D in Fig. 11). More precisely, when a bias current $I_b < I_0$ is applied to the Quantronium, small oscillations of the phase δ are centered on $\delta_0 \simeq \arcsin(I_b/I_0)$ and the readout junction behaves as an inductance $L_{J0} \simeq \varphi_0/[I_0\cos\delta_0]$ much smaller than the inductance L_J of the box junction. Y_R and L_{J0} form together an effective admittance $Y_{R,eq} = Y_R // L_{J0}$ that generates current fluctuations characterized by the spectral density

$$S_I = \frac{\hbar\omega}{2\pi}\left[1+\coth\left(\frac{\hbar\omega}{2k_BT}\right)\right]\mathrm{Re}[Y_R]. \tag{4.6}$$

$|Y_R|$ being much smaller than the effective inductance of the series combination of the two CPB Josephson junctions, this current I goes through $Y_{R,eq}$ and is converted into noise on voltage $v = \varphi_0 d\delta/dt = I/Y_{R,eq}$, or equivalently into a δ noise with spectral density

$$S_\delta^{Y_R} \simeq \left(\frac{1}{\varphi_0\omega}\right)^2 \frac{S_I}{\left|Y_R + \frac{1}{iL_{J0}\omega}\right|^2}\,. \tag{4.7}$$

Internal decoherence sources Finally, as examples of internal decoherence sources, one can think of out-of-equilibrium quasiparticles tunneling across the Josephson junctions or of an atom in the CPB Josephson junction jumping back and forth between two atomic sites so that a tunneling channel of the junction is open and closed randomly, such that it induces noise on E_J. Note that part of the decoherence of Josephson phase qubits has been attributed to this latter phenomenon [2].

4.3. *Depolarization of a Cooper pair box*

Relaxation and excitation proceed by exchange of an energy quantum $\hbar\Omega_{01}$ between the qubit and an oscillating field of the environment with pulsation $\omega = \Omega_{01} = 2\pi\nu_{01}$. Applying the Fermi golden rule to such processes gives:

$$\Gamma_{\downarrow,X} = \frac{\pi}{2}\left(\frac{D_{\lambda,\perp}}{\hbar}\right)^2 S_{\lambda_0,X}(\Omega_{01}), \tag{4.8}$$

$$\Gamma_{\uparrow,X} = \frac{\pi}{2}\left(\frac{D_{\lambda,\perp}}{\hbar}\right)^2 S_{\lambda_0,X}(-\,\Omega_{01})\,, \tag{4.9}$$

where the transverse part of $\overrightarrow{D}_\lambda$, $D_{\lambda,\perp} = 2|\langle 1|\widehat{\partial H/\partial\lambda}|0\rangle|$, is equal to $4E_C|\langle 0|\widehat{\mathbf{N}}|1\rangle|$ for all N_g noise sources and equal to $2\varphi_0|\langle 0|\widehat{\mathbf{I}}|1\rangle|$ for all δ noise sources, according to (2.13) and (2.15), respectively. Going further requires then specifying the origin of the noise. For the background charge noise, the spectral density is unfortunately unknown in the GHz range that corresponds to Ω_{01} so that no serious prediction of $\Gamma_{\downarrow,X}$ and $\Gamma_{\uparrow,X}$ can be made. For the gate line impedance $Z_g(\omega)$ at a temperature $T \ll \hbar\Omega_{01}/k_B$, $S_{N_g,Z_g}(-\Omega_{01})$ and $S_{N_g,Z_g}(\Omega_{01})$ obey detailed balance and

$$\frac{\Gamma_{\uparrow,Z_g}}{\Gamma_{\downarrow,Z_g}} = \exp(-\frac{\hbar\Omega_{01}}{k_B T}) \ll 1 .$$

Then, after substituting $D_{\lambda,\perp}$ and (4.5) at zero temperature in (4.8), one gets the relaxation rate

$$\Gamma_{\downarrow,Z_g} = 16\pi\kappa_g^2 \left|\langle 0|\widehat{\mathbf{N}}|1\rangle\right|^2 \frac{\mathrm{Re}[Z_g(\Omega_{01})]}{R_k}\Omega_{01} , \tag{4.10}$$

which takes the simpler form $\Gamma_{\downarrow,Z_g} = 4\pi\kappa_g^2\Omega_{01}\sin^2\alpha\,\mathrm{Re}[Z_g(\Omega_{01})]/R_k$ in the limit $E_J/E_C \ll 1$. In conclusion, a $\mathrm{Re}[Z_g(20\mathrm{GHz})]$ as large as 10Ω coupled with $\kappa_g \sim 1-2\%$ would induce relaxation of a CPB having a $1k_BK$ transition energy with a rate of only $0.1\sin^2\alpha$ MHz.

We evaluate now the relaxation induced by a resistance $R = 1/Y_R$ in parallel with the Quantronium readout junction. Substituting $D_{\lambda,\perp}$ and (4.7) at zero temperature in (4.8), one obtains after simple algebraic transformations:

$$\Gamma_{\downarrow,R} = \frac{2\left|\langle 0|\widehat{\mathbf{I}}|1\rangle\right|^2}{\hbar\Omega_{01}} \frac{R}{\left|1+\frac{R}{iL_{J0}\Omega_{01}}\right|^2} , \tag{4.11}$$

which simplifies to $\Gamma_{\downarrow,R} = 2|\langle 0|\widehat{\mathbf{I}}|1\rangle|^2 R/(\hbar\Omega_{01})$ for $R \ll L_{J0}\Omega_{01}$. At $N_g = 1/2$, $\langle 0|\widehat{\mathbf{I}}|1\rangle$ increases linearly with the asymmetry d between the box junctions. $\Gamma_{\downarrow,R}$ varies as d^2 and a Quantronium with a $1k_BK$ transition energy and an asymmetry $d = 5\%$ would relax with a rate of order 1 MHz under the influence of a readout resistance $R = 2\Omega$ at 20 GHz. Obtaining balanced junctions during the fabrication of a Quantronium is thus an important point.

4.4. *Random dephasing of a Cooper pair box*

In a semi-classical approach, the random phase $\Delta\varphi_X(t)$ between the two components of a superposed state is obtained by integration of the longitudinal fluctuations of $\widehat{H}_X$:

$$\Delta\varphi_X(t) = \frac{D_{\lambda,z}}{\hbar}\int_0^t \lambda_0^X(t')dt' , \tag{4.12}$$

where the longitudinal part of $\overrightarrow{D}_\lambda$, $D_{\lambda,z} = \langle 0|\widehat{\partial H/\partial\lambda}|0\rangle - \langle 1|\widehat{\partial H/\partial\lambda}|1\rangle \approx h\partial\nu_{01}/\partial\lambda$, is equal to $-2E_C\,\Delta N_{10}$ for all N_g noise sources and equal to $-\varphi_0\Delta i_{10}$ for all δ noises sources, according to sections 2.4 and 2.6. An important point to notice is that the coefficients of sensitivity to charge and phase noise, $D_{Ng,z}$ and $D_{\delta,z}$, vanish when ΔN_{10} and Δi_{10} are equal to zero, i.e. at $N_g = 0$ and $\delta = 0$, where the transition frequency is stationary. Then, $\lambda_0^X(t)$ being a Gaussian noise in most cases, the ensemble average $f_X(t) = \langle\exp[i\Delta\varphi_X(t)]\rangle$ is written

$$f_X(t) = \exp[-\left\langle\Delta\varphi_X^2(t)\right\rangle/2] \tag{4.13}$$

and depends only on the variance of the random phase, which can be calculated from the classical spectral density $\widetilde{S}_{\lambda_0}^X(\omega)$ of λ_0^X:

$$\left\langle\Delta\varphi_X^2(t)\right\rangle = \left(\frac{D_{\lambda,z}}{\hbar}t\right)^2 \int_{-\infty}^{+\infty} d\omega\, \widetilde{S}_{\lambda_0}^X(\omega)\mathrm{sinc}^2(\frac{\omega t}{2}) , \tag{4.14}$$

with $\mathrm{sinc}(x) = \sin(x)/x$. A full quantum calculation [9] of $f_X(t)$, based on a thermal average over a bath of harmonic oscillators linearly coupled to $\widehat{\lambda}$, gives the same result:

$$f_X(t) = \exp\left[-\frac{t^2}{2}\left(\frac{D_{\lambda,z}}{\hbar}\right)^2 \int_{-\infty}^{+\infty} d\omega\, S_{\lambda_0}^X(\omega)\mathrm{sinc}^2(\frac{\omega t}{2})\right] , \tag{4.15}$$

but with $\widetilde{S}_{\lambda_0}^X$ being replaced by its quantum analogue. Applied to the background charge noise, (4.15) becomes

$$f_{BCN}(t) = \exp\left[-B\left(\frac{2E_C\,\Delta N_{10}}{\hbar}\right)^2 t^2 \ln\frac{\tau}{t}\right] , \tag{4.16}$$

where τ is the time taken experimentally to define the average transition frequency, this time introducing a low frequency cutoff $1/\tau$ in the integral of (4.15). The function $f_{BCN}(t)$ decays almost as a Gaussian with an effective characteristic time $T_2^{*BCN} = [2\sqrt{B\ln(\tau/t)}E_C\,\Delta N_{10}/\hbar]^{-1}$ that decreases almost as $1/(N_g - 1/2)$ close to the charge degeneracy (see the ΔN_{10} variations of Fig. 2). Assuming $B \sim 10^{-8}$ and $\tau \sim 10^2 s$, one gets $T_2^{*BCN} \sim 50ns$ for a CPB with $E_J \sim E_C \sim 1k_BK$ operated at $N_g = 0.55$.

In contrast to $\widetilde{S}_{N_g}^{BCN}(\omega)$, spectral densities $S_{\lambda_0}^X(\omega)$ of other noise sources are often rather flat below a cut-off frequency ω_c, so that for $t > 1/\omega_c$, $S_{\lambda_0}^X(\omega) \approx S_{\lambda_0}^X(0)$ in the ω range where the sinc square term gives its main contribution to the integral in (4.15). Consequently, $f_X(t) \approx \exp[-\Gamma_\varphi^X t]$ with a decay rate

$$\Gamma_\varphi^X \approx \pi\left(\frac{D_{\lambda,z}}{\hbar}\right)^2 S_{\lambda_0}^X(\omega \approx 0) . \tag{4.17}$$

At 50 mK, spectral densities (4.5) and (4.7) vary only by a factor two below 200 MHz so that (4.17) holds for $t > 5ns$. Substituting the correct $D_{\lambda,\perp}$ and (4.5) [resp. (4.7)] at zero frequency in (4.17), one finds the contribution to random dephasing of the gate line circuit (resp. of the Quantronium readout):

$$\Gamma_{\varphi}^{Z_g} \approx 8\pi\kappa_g^2 \Delta N_{10}^2(N_{g0}) \frac{k_B T}{\hbar} \frac{R}{R_k} , \tag{4.18}$$

$$\Gamma_{\varphi}^{R} \approx \frac{1}{8\pi} \left(\frac{\Delta i_{10}(\delta_0)}{I_0 \cos \delta_0} \right)^2 \frac{k_B T}{\hbar} \frac{R_k}{R}, \tag{4.19}$$

where R is the resistance of the gate voltage source (4.18) and the resistance in parallel with the Quantronium readout junction in (4.19), in the 0.1-100 MHz frequency range. Taking the same CPB parameters as in the previous section and assuming an electronic temperature of 50 mK, one gets $\Gamma_{\varphi}^{Z_g} < 25\text{kHz}$ for $R = 10\Omega$, showing that the gate line is not an important dephasing channel. Assuming then typical values $I_0 \sim 500nA$ and $R = 100\Omega$ for a Quantronium readout circuit, one obtains $\Gamma_{\varphi}^{R} \sim 2\delta_0^2(rad)/\cos^2\delta_0\text{MHz}$. Therefore, Γ_{φ}^{R} is negligible close to $\delta_0 = 0$ and increases very rapidly up to about 100 MHz at the top of the readout current pulse, where δ approaches $\pi/2$.

4.5. Design rules and optimal working points

We now focus on the requirements that an experimental setup has to fulfill in order to demonstrate an operational CPB-based-qubit. First, the CPB has to be reset in its reference stable state $|0\rangle$ with a small probability of error $e \geq \epsilon = \Gamma_{\uparrow}/\Gamma_{1}$. This takes a reset time $t_r \sim e/\Gamma_1$ that defines the maximum repetition rate in an experiment. Secondly, during the manipulation of the state, the characteristic decay time T_2^* of $F_2(t)$ must be as long as possible in order to perform as many coherent single qubit or two qubit gate operations as possible. Consequently, $T_1 = 1/\Gamma_1$ and the characteristic decay time T_{φ}^* of the F function have to be maximized. For that purpose, a first action is of course to minimize all the noise spectral densities of section 4.2. A complementary approach is to choose a working point where the sensitivity to noise is minimal. For a split box, according to sections 4.3 and 4.4, T_1 and the T_{φ}^*'s can be maximized by choosing a manipulation point such that $\langle 1|\, I \,|0\rangle \simeq 0$ and such that the transition frequency is stationary with respect to both N_g and δ fluctuations. Figure 12 shows that the point ($N_g = 1/2, \delta = 0$) is such an "optimal manipulation point". But since both charge signal ΔN_{10} and current signal Δi_{10} vanish at this point, one has to apply a shift to N_g or δ at the end of the manipulation to measure the qubit state through the charge or phase port. Then, the elementary measuring time t_{m0}, defined as the time during which the readout interacts with the qubit after the

preparation of a particular quantum state, is constrained in a way that depends on the readout strategy. When the readout absorbs the transition energy of the qubit as described in section 3.2.1, the readout port must be the main relaxation channel in order to avoid errors. Therefore, the values of $\Gamma_{\downarrow,X}$ and t_{m0} must obey $1/\Gamma_1 \simeq 1/\Gamma_{\downarrow} \simeq 1/\Gamma_{\downarrow,readout} \leq t_{m0}$. In all other cases, a readout error probability smaller than e_r requires $e_r T_1 > t_{m0}$. Consequently, we wish to maximize T_1 during readout by choosing a measurement point where $\langle 1|\, I \,|0\rangle \simeq 0$ as well. Moreover, t_{m0} has to be longer than T_{φ}^* since the qubit density matrix has to become diagonal before a projective measurement is completed. Since dephasing is required only during measurement, it is thus a good design rule to implement a switchable readout device such that T_{φ}^* decreases by several orders of magnitude when the readout is switched on, whereas T_1 remains long. Moving away from an "optimal manipulation point" along a "slow relaxation line" is just such a switch. Finally, it is convenient to have a single shot readout, able to distinguish the two qubit states with a small error rate e_r within the time t_{m0}. Otherwise, repeating several times the preparation and the measurement of the same quantum state is required to reach the same target error rate. The Quantronium has been designed to fulfill all the requirements mentioned here and has demonstrated experimentally good quantum coherence properties, which are presented in the next

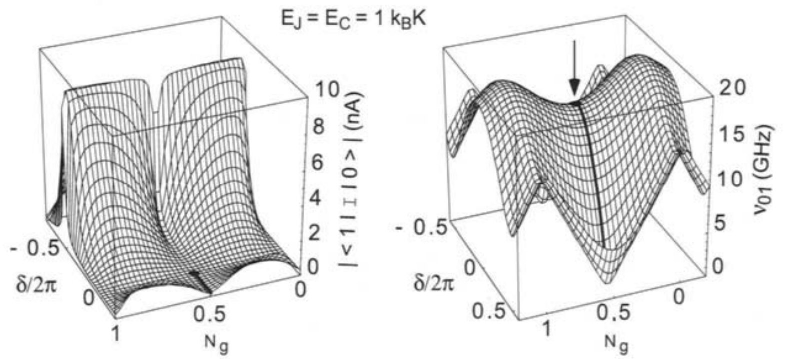

Fig. 12. Sensitivity to decoherence of a Quantronium with $E_J = E_C = 1k_BK$ and $d = 2\%$, as a function of its reduced external parameters N_g and $\delta/2\pi$. Left box: Loop current matrix element between states $|0\rangle$ and $|1\rangle$. This matrix element and consequently the relaxation rate of the qubit are minimal along the lines $\delta = 0$ and $N_g = 1/2$. Right box: Transition frequency of the Quantronium. The arrow indicates the stationary point ($N_g = 1/2$, $\delta = 0$) where pure dephasing vanishes to first order. Consequently, this is the optimal point for coherent manipulation of the Quantronium. For reading out the state, the working point is adiabatically moved along the bold solid line, where relaxation of the qubit induced by quantum noise on δ is minimal.

4.6. Experimental characterization of decoherence

The results presented below have been obtained with a Quantronium sample similar to that shown in Fig. 10, with $E_J = 0.86 k_B K$, $E_C = 0.68 k_B K$, and an asymmetry d between the CPB junctions not precisely known, but lower than 5%. We first measured the relaxation time at the optimal working point by switching on the readout at some variable time t_d after applying a microwave π pulse that prepares the qubit in state $|1\rangle$ (see Fig.13). A rough estimation of the readout resistance of the setup giving $R(20GHz) = 1\Omega - 5\Omega$, the experimental $T_1 = 1.8\mu s$ could be explained by an asymmetry coefficient $d \sim 5\% - 2\%$.

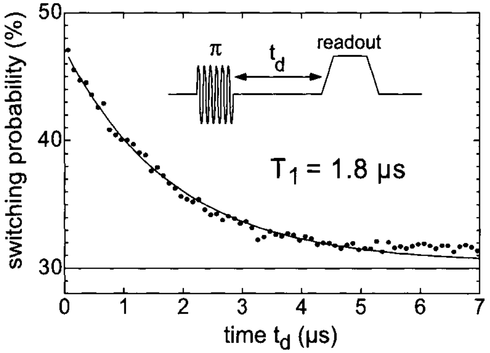

Fig. 13. Decay of the switching probability of the Quantronium's readout junction as a function of the delay between a microwave π pulse and the readout current pulse. The solid line is a fit of the data (dots) by an exponential shifted by the signal measured when no microwave is applied (horizontal bottom line).

Then, spectroscopic measurements (see Fig. 14) of ν_{01}were performed by applying to the gate a weak continuous microwave irradiation suppressed just before the readout current pulse. The variations of the switching probability as a function of the microwave frequency, display a resonance peak whose position ν_{01} as a function of N_g and δ leads to a precise determination of E_J and E_C. The resonance line shape being the Fourier transform of $F_2(t)$, the full line width at half-maximum $\Delta\nu_{01}$ leads to an effective coherence time $T_2^* = c/\Delta\nu_{01}$with $c \sim 1/\pi$ depending on the exact line shape. As expected, $\Delta\nu_{01}$ was found to be minimal at the optimal point ($N_g = 1/2, \delta = 0$), where $\Delta\nu_{01} = 0.8$ MHz. Consequently, $2T_1 \gg T_2^* \simeq 0.4\mu s \simeq T_\varphi^*$ and decoherence is dominated by random dephasing. When departing from the optimal point, the line broadens very rapidly. For $N_g \neq 1/2$, it also becomes structured and not reproducible (see top right panel of Fig. 14) due to individual charged two-level-fluctuators. Nevertheless, the general trend (see bottom panel of Fig. 14) is that $\Delta\nu_{01}$ varies more or less linearly with $N_g - 1/2$ and δ, the proportionality coefficients $\partial\Delta\nu_{01}/\ \partial(\delta/2\pi)$ and $\partial\Delta\nu_{01}/\ \partial N_g$ being of order 0.3GHz. Noticing that ν_{01} varies quadratically in the vicinity of the optimal point so that $D_{\lambda,z} \approx h\partial\nu_{01}/\partial\lambda \propto \lambda \propto \Delta\nu_{01}$, one deduces from section 4.4, that both charge and phase noises are peaked at low frequencies and that the random dephasing functions should decay as Gaussians. This effect is well understood for the charge noise, which is dominated by the 1/f contribution of microscopic origin. Using the actual parameters of the sample in (4.16), the experimental $\partial\Delta\nu_{01}/\ \partial N_g$ leads to an amplitude $B \simeq 10^{-7}$ for the BCN, a value in agreement with previous measurements on similar Josephson devices. By contrast, the origin of the low frequency phase noise is not understood. An important point to mention here is that the experimental value of T_2^* at the optimal working point corresponds to that estimated by taking into account the second order contribution of the charge and phase noises.

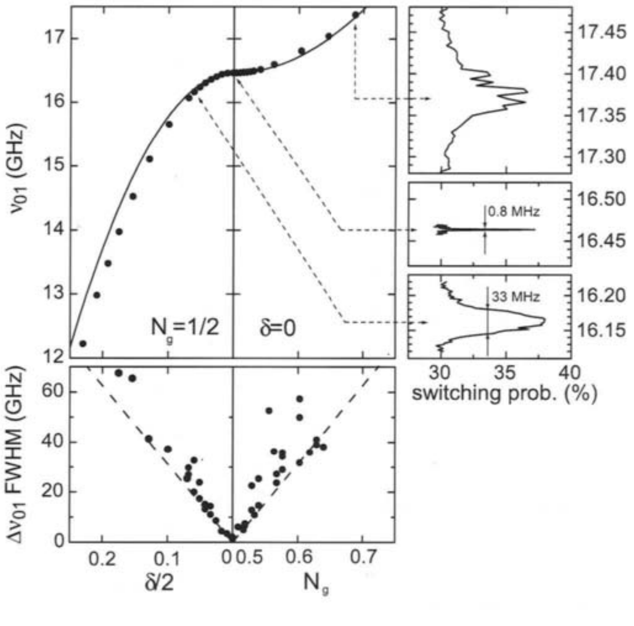

Fig. 14. Spectroscopy of a Quantronium. Top left panel: transition frequency as a function of δ at $N_g = 1/2$ and as a function of N_g at $\delta = 0$. The solid line is a fit that gives E_J and E_C. Right panels: resonance lines recorded with a small microwave power at three different working points (same scale for all lines). Bottom left panel: Full width at half-maximum $\Delta\nu_{01}$ of the resonance lines. Due to a slow and large charged two-level-fluctuator (TLF), data points can vary by a factor 2. The dotted lines indicate that $\Delta\nu_{01}$varies linearly with the external parameters when this TLF is stable.

The direct measurement of the coherence time T_2^* during free evolution was obtained by performing a Ramsey-fringe-like experiment (see also [21]). One applies to the gate two slightly off-resonance $\pi/2$ microwave pulses separated by a delay Δt during which the spin representing the qubit state precesses freely at frequency $\Delta\nu$ in the equatorial plane of the Bloch sphere. Whereas the first pulse simply sends the spin onto the equator, the second one converts the phase accumulated during Δt into a longitudinal component of the spin. The probability to measure $|1\rangle$ at the end of the sequence oscillates as $\cos^2(\pi\Delta\nu\Delta t)$ with an amplitude that decays as $F_2(t)$. Figure 15 shows the result of such an experiment performed at the optimal manipulation point. Although the low signal to noise ratio and the long term drift due to 1/f noise prevents determination of wether the decay of the oscillations is more Gaussian than exponential, a fit of the data leads to $T_2^* \simeq 0.5\mu s$, a value that corresponds to that previously deduced from the resonance line width. Given the transition period $1/\nu_{01} \sim 60$ps, the coherence time T_2^* corresponds to about 8000 free precession turns around the z axis. Assuming that a bit flip can be performed with a microwave pulse of only 30 oscillations, i.e. in a time ~ 2ns, T_2^* corresponds also to the time required for about 250 bit flips.

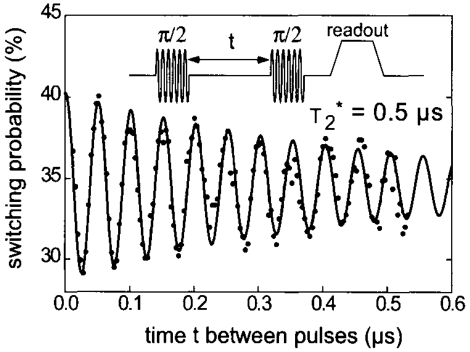

Fig. 15. Ramsey fringe experiment on a Quantronium: When two $\pi/2$ microwave pulses detuned with $\Delta\nu = 20.6$ MHz and separated by Δt are applied to the gate, the switching probability of the readout junction oscillates as a function of Δt with frequency $\Delta\nu$. Each experimental point (dot) is an average over 50000 sequences. The solid line is a fit by an exponentially decaying cosine, the decay time constant of which corresponds to the coherence time T_2^*.

The coherence can also be maintained artificially during a time longer than T_2^* using NMR-like echo sequences [18]. An intermediate π pulse is inserted in a Ramsey sequence, a time $\Delta t_1 < \Delta t$ after the first $\pi/2$ pulse (see Fig. 16). Assuming for instance that all rotations are performed around the y' axis of the Bloch sphere, the effect of this π pulse is to change rapidly the phase of the spin from $\varphi = 2\pi\Delta\nu\Delta t_1$ to $\varphi = \pi - 2\pi\Delta\nu\Delta t_1$. Then, the phase grows again by an amount $2\pi\Delta\nu(\Delta t - \Delta t_1)$ before the last $\pi/2$ pulse. The probability to measure $|1\rangle$ at the end of the sequence is $\sin^2[\pi\Delta\nu(\Delta t - 2\Delta t_1)]$. When $\Delta t_1 = \Delta t/2$, this probability is thus less sensitive to $\Delta\nu$ fluctuations than the Ramsey function $\cos^2(\pi\Delta\nu\Delta t)$. In other words, a π pulse in the middle of an echo sequence makes the spin go a longer (resp. shorter) path along the equator when the precession speed is faster (resp. slower), so that the ending point is the same from sequence to sequence, provided that $\Delta\nu$ is constant within a sequence. Figure 16 compares a Ramsey sequence and an echo sequence with variable Δt_1 performed at $N_g = 0.52$ and $\delta = 0$, where T_2^* is reduced to 30ns. For $\Delta t = 2\Delta t_1 \sim 20T_2^*$, the amplitude of the echo is still 20% of the maximum amplitude whereas the Ramsey signal is of course zero. This result confirms that decoherence is essentially due to charge noise at frequencies lower than $1/\Delta t \sim 1$ MHz. Although mapping the amplitude of the echo as a function of Δt for different working points can give much information on the shape of noise spectral densities, no complete study could be made on the sample presented here.

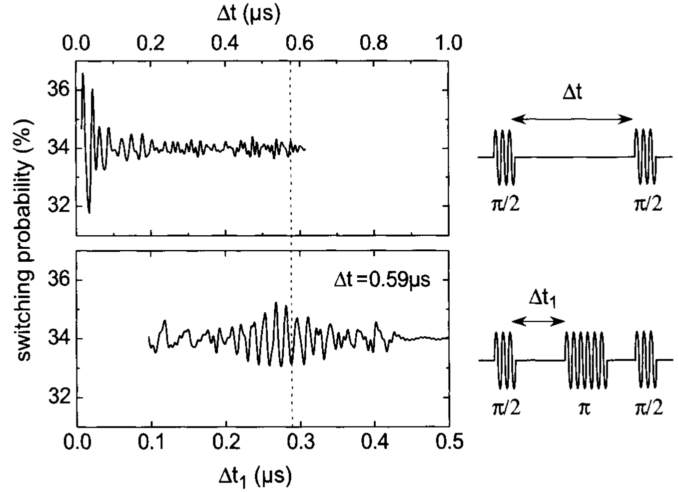

Fig. 16. Comparison between a Ramsey and an echo sequence (top right and bottom right pictograms, respectively) with a Quantronium circuit operated at the working point ($N_g = 0.52$, $\delta = 0$) with a detuning $\Delta\nu = 41$MHz. Top panel: Ramsey fringes of the Quantronium's switching probability indicating a coherence time of only 30 ns. Bottom panel: Echo signal taken at fixed $\Delta t = 0.59\mu s$ as a function of Δt_1. Very close to $\Delta t_1 = \Delta t/2$, the amplitude of the echo is maximum and equal to about 20% of the signal at $\Delta t = 0$. The dashed vertical line indicates Δt_1 and points out that the Ramsey signal has completely disappeared for the same Δt.

5. Two-qubit-gates with capacitively coupled Cooper pair boxes

Being able to implement any quantum algorithms requires adding to all possible single qubit operations a two-qubit gate such that the ensemble forms a so-called universal set of gates [30]. Many coupling schemes of two (or more) CPBs have been proposed to realize such 2-qubit gates. The nature of the coupling can be either capacitive or inductive. In the first case, two CPB islands are coupled by a capacitor, whereas in the second case, the loops of two split CPBs are coupled by a mutual inductance or galvanically by an inductor or an additional Josephson junction. Although ideally the coupling should be switchable and tunable, using a constant coupling is of course simpler. In this paper, we restrict ourselves to the constant capacitive coupling between two CPBs, which is the only scheme that has been implemented at the time of writing.

The Hamiltonian of two CPBs indexed 1 and 2, the islands of which are coupled by a capacitor C_C, is the sum of two terms (2.3) with Josephson energies including eventually a phase term if the box is split and with Cooper pair Coulomb energies involving now $C_\Sigma \approx C_g + C_J + C_C$, and of a coupling term

$$E_{CC}(\widehat{\mathbf{N}}_1 - N_{g1})(\widehat{\mathbf{N}}_2 - N_{g2}) \text{ with } E_{CC} \approx E_{C1}E_{C2}\frac{C_C}{(2e)^2}\,. \tag{5.1}$$

Within the spin formalism and when $E_J/E_C \ll 1$, Hamiltonian (5.1) is rewritten in the pure charge state basis $(|\mathbf{0}\rangle_{c1}\,, |\mathbf{1}\rangle_{c1}) \otimes (|\mathbf{0}\rangle_{c2}\,, |\mathbf{1}\rangle_{c2})$:

$$\begin{aligned}\widehat{H}(N_{g1}, N_{g2}) = &-\frac{1}{2}\left\{E_{J1}\widehat{\sigma}_{X1} + \left[(1-2N_{g1})E'_{C1} + (1-2N_{g2})\frac{E_{CC}}{2}\right]\widehat{\sigma}_{Z1}\right\}\\ &-\frac{1}{2}\left\{E_{J2}\widehat{\sigma}_{X2} + \left[(1-2N_{g2})E'_{C2} + (1-2N_{g1})\frac{E_{CC}}{2}\right]\widehat{\sigma}_{Z2}\right\}\\ &+\frac{E_{CC}}{4}\widehat{\sigma}_{Z1}\widehat{\sigma}_{Z2}\,,\end{aligned} \tag{5.2}$$

where constant terms that depend only on N_{g1} and N_{g2} have been dropped. The coherent evolution induced by this Hamiltonian has been experimentally demonstrated [31] with two strongly coupled ($E_{CC} \sim E_{J1,2}$) CPBs, using the fast DC gate pulses (see section 3.1.1) to the charge co-degeneracy point $N_{g1} = N_{g2} = 1/2$, and using the readout technique described in section 3.2.1. A conditional operation close to the Controlled-NOT gate has also been demonstrated [32] with the same system. The main idea behind this experiment is to regard the $\widehat{\sigma}_{Z1}\widehat{\sigma}_{Z2}$ coupling as shifting the CPB2 charge degeneracy point by a quantity that depends on the state of CPB1. Indeed, this degeneracy point is defined by $(1-2N_{g2})E'_{C2} + (1-2N_{g1} \mp 1/2)E_{CC}/2 = 0$. A gate 2 pulse bringing CPB2 to the charge degeneracy when CPB1 is in state $|\mathbf{0}\rangle_{c1}$, brings it $\Delta N_{g2} = 1/2 - E_{CC}/4E'_{C2}$ away from the degeneracy when CPB1 is in state $|\mathbf{1}\rangle_{c1}$. According to section 3.1.1, the maximum probability of $|\mathbf{1}\rangle_{c2}$ after the pulse drops rapidly with ΔN_{g2} as $1/\{1 + [2E_C\Delta N_{g2}/E_J]^2\}$, so that bit 2 can be flipped when bit 1 is in state $|\mathbf{0}\rangle_{c1}$, whereas it is almost unchanged when bit 1 is in state $|\mathbf{1}\rangle_{c1}$. Figure 17 shows the experimental results obtained by the NEC group with such a C-NOT.

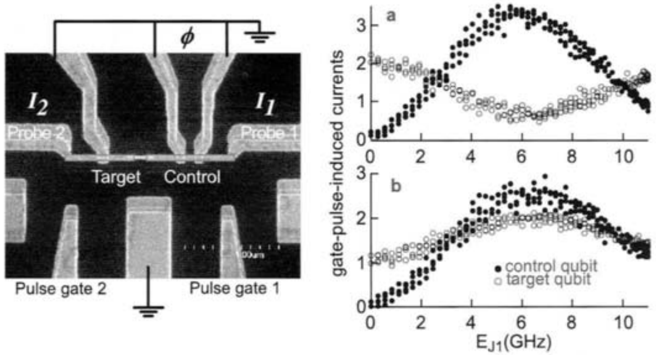

Fig. 17. Demonstration of a C-NOT-type quantum gate with two capacitively coupled CPBs by T. Yamamoto and co-workers. Left: Scanning electron micrography of the device. The qubits are manipulated using the fast dc pulse technique. Here, the target qubit is prepared in the pure charge state $|\mathbf{0}\rangle_c$ (a) or $|\mathbf{1}\rangle_c$ (b) whereas the control qubit is prepared with a dc pulse of constant width in a superposition state that depends on the Josephson energy E_{J1} of qubit 1. Finally, a gate 2 pulse performs the CNOT as explained in the text. Right panels: Anticorrelation (a) and correlation (b) between the two probe currents as a function of E_{J1}. *Courtesy of T. Yamamoto et al., NEC, Japan.*

Another type of gate can be developed by working in the uncoupled energy eigenbasis $(|0\rangle_1\,, |1\rangle_1) \otimes (|0\rangle_2\,, |1\rangle_2)$ at fixed $N_{g1} = N_{g2} = 1/2$, where $\langle 0|\,\widehat{\mathbf{N}}\,|0\rangle = \langle 1|\,\widehat{\mathbf{N}}\,|1\rangle = 1/2$. The Hamitonian (5.1) is now rewritten as

$$\widehat{H}(N_{g1}, N_{g2}) = -\frac{1}{2}h\nu_1\widehat{\sigma}_{Z1} - \frac{1}{2}h\nu_2\widehat{\sigma}_{Z2} + K\widehat{\sigma}_{X1}\widehat{\sigma}_{X2}\,, \tag{5.3}$$

with $K = E_{CC}\left|{}_1\langle 1|\,\widehat{\mathbf{N}}_1\,|0\rangle_1\right|\left|{}_2\langle 1|\,\widehat{\mathbf{N}}_2\,|0\rangle_2\right|$, the corresponding matrix being

$$\widehat{H} = \begin{pmatrix} \begin{bmatrix} -h\overline{\nu} & K \\ K & h\overline{\nu} \end{bmatrix} & [0] \\ [0] & \begin{bmatrix} -\frac{h\Delta\nu}{2} & K \\ K & \frac{h\Delta\nu}{2} \end{bmatrix} \end{pmatrix}_{(|00\rangle,|11\rangle,|01\rangle,|10\rangle)}\,, \tag{5.4}$$

with $\overline{\nu} = (\nu_1 + \nu_2)/2$ and $\Delta\nu = \nu_1 - \nu_2$. In the weak coupling limit defined by $C_C \ll C_{\Sigma 1,2}$, the coupling strength $K/h\overline{\nu}$ between $|00\rangle$ and $|11\rangle$ is always weak, whereas coupling strength $2K/h\Delta\nu$ between $|01\rangle$ and $|10\rangle$ can be varied by adjusting the difference between the two qubit transition frequencies. By equating ν_1 and ν_2, this coupling is maximized and $|01\rangle$ and $|10\rangle$ are simply swapped in a time $t_{SWAP} = \pi\hbar/2K$, whereas $|00\rangle$ and $|11\rangle$ are almost unchanged. When applying the effective coupling during $t_{SWAP}/2$, one obtains the so-called $\sqrt{iSWAP}$ gate, which entangles $|01\rangle$ and $|10\rangle$ in a simple and efficient way and which forms a universal set of gates when complemented with 1-qubit operations. Moreover, the $\widehat{\sigma}_{X1}\widehat{\sigma}_{X2}$ nature of the coupling has the great advantage of conserving the property of a vanishing random dephasing at the optimal manipulation point. An experiment aiming at testing such an $\sqrt{iSWAP}$ gate prototype with two capacitively coupled Quantroniums is currently in preparation.

6. Conclusions

As anticipated in 1995 immediately after the first successful characterization of a Cooper pair box [7], this device has been shown to have sufficiently good quantum properties to be used for building quantum bit prototypes. In less than ten years, two different schemes for driving the quantum state of a CPB and three very different readouts were developed and tested in several laboratories [16, 17, 20, 25]. Spectroscopy and coherent free and driven quantum evolution were demonstrated over times ranging from a few nanoseconds up to about a microsecond. Other Josephson qubits were also able to reach comparable results and Josephson qubits should now be considered as a single family, the sub-families having only historical justifications. The research community involved in the development of Josephson qubits has made great progress in understanding how decoherence occurs in electrical circuits and "quantum electrical engineering" was really born. The concept of optimal manipulation and measuring points of such circuits could for instance be formulated and experimentally tested. Moreover, experimental protocols for characterizing decohering effects and decoherence sources are continuously improving. With the development of more complex manipulations of Josephson qubits, methods to limit decoherence such as NMR-like echoes and spin locking have already been or are about to be tested. Preliminary experiments on two coupled CPB-based-qubits have demonstrated in 2003 a first solid-state-two-qubit-gate prototype. Nevertheless, the route towards a real quantum processor incorporating, for instance, quantum error correcting circuits is still long. A good quantum-non-demolition single-shot-readout is still lacking, the precision of qubit manipulations is still weak compared to that achieved in quantum optics, and coherence times must be increased by one or two orders of magnitude to start implementing simple algorithms. Finally, the scalability of Josephson qubits is still to be demonstrated. To conclude, although we do not think that any serious prediction can be made about the future existence or not of a (Josephson) Quantum computer, we are convinced that developing Josephson qubits is a very valuable program of research that paves the way towards a truly quantum electronics and toward machines in which quantum physics will manifest itself at a more "macroscopic" scale.

Acknowledgements

A large part of the physics presented here, including the development of the CPB and of the Quantronium is the fruit of a collective work in the "Quantronics group", which is part of the condensed matter physics division (SPEC) of CEA-Saclay, France. We warmly thank the other permanent members of the group, P. Orfila, P. Senat, P. Joyez, H. Pothier, C. Urbina, M. Devoret and D. Esteve, and also the past and present post-docs and Ph.D. students, E. Turlot, P. Lafarge, V. Bouchiat, A. Cottet, A. Aassime, and E. Collin for their direct participation in the development of Josephson qubits. We also gratefully acknowledge the research group of J.S. Tsai, Y. Nakamura, and T. Yamamoto from the "NEC Fundamental Research Lab" (Tsukuba, Japan) and the "Quantum Device Physics" group headed by Per Delsing at Chalmers University of Technology (Göteborg, Sweden) for providing material included in this chapter. We also should like to thank very much all the people we have been collaborating with over the past ten years, in particular I. Chuang from IBM, J. Martinis from NIST, O. Buisson from CRTBT, the group of H. Mooij from Delft University, the group of G. Schön from Karlsruhe, and all our colleagues from the SQUBIT european projects. Finally, I thank N. Birge and P. Meeson who helped to improve this text.

References

[1] See chapter by M. Devoret in this book.
[2] See chapter by J. Martinis in this book.
[3] See chapter by H. Mooij in this book.
[4] A. Barone and G. Paternò, *Physics and applications of the Josephson effect* (Wiley, New York, 1982).
[5] *Single Charge Tunneling*, edited by H. Grabert and M. H. Devoret (Plenum Press, New York, 1992).
[6] M. Büttiker, Phys. Rev. B **36**, 3548 (1987).
[7] V. Bouchiat et al., Physica Scripta **76**, 165 (1998).

[8] P. Lafarge et al., Nature **365**, 422 (1993).

[9] A. Cottet, *Implementation of a quantum bit in a superconducting circuit*, Thesis, University Paris VI, Paris (2002).

[10] C. Cohen-Tannoudji, B. Diu and F. Laloë, *Mécanique quantique T II*, Hermann, Paris.

[11] D. V. Averin, K. K. Likharev, in *Mesoscopic Phenomena in Solids*, edited by B. L. Altshuler, P. A. Lee, and R. A. Webb (Elsevier, Amsterdam, 1991).

[12] A.B. Zorin, Phys. Rev. Lett. **76**, 4408 (1996).

[13] A. Cottet, D. Vion, P. Joyez, P. Aassime, D. Esteve, M.H. Devoret, Physica C **367**, 197 (2002).

[14] A. B. Zorin, Physica C **368**, 284 (2002).

[15] J. R. Friedman and D. V. Averin, Phys. Rev. Lett. **88**, 50403 (2002).

[16] Y. Nakamura, Yu. A. Pashkin and J. S. Tsai, Nature **398**, 786, (1999)

[17] T. Duty et al., cond-mat / 0305433 (2003).

[18] See chapter by J. Jones in this book.

[19] See chapter by I. Chuang in this book.

[20] D. Vion et al., Science **296**, 886 (2002).

[21] See chapter by M. Brune in this book.

[22] F. W. J. Hekking et al., in *Electronic Correlations: from Meso- to Nanophysics*, T. Martin, G. Montambaux and J. Trân Thanh Vân, eds. (EDP Sciences, 2001), p. 515.

[23] I. Siddiqi et al., cond-mat/0312553 (2003).

[24] See chapter by R. Schoelkopf in this book.

[25] R.J. Schoelkopf *et al.*, Science, 280, 1238 (1998).

[26] A. Cottet et al., Workshop on "Macroscopic Quantum Coherence and Computing", Naples, Italy (2001).

[27] A. Aassime et al., Phys. Rev. Lett., **86**, 3376 (2001).

[28] T.A. Fulton, P.L. Gammel, D.J. Bishop, L.N.Dunkleberger, and G.J. Dolan, Phys. Rev. Lett. 63,1307 (1989).

[29] Y. Makhlin, G. Schön and A. Schnirman, Rev. Mod. Phy, **73**, 357 (2001)

[30] M.A. Nielsen and I.L. Chuang, Quantum Computation and Quantum Information (Cambridge University Press, Cambridge, 2000).

[31] Yu. A. Pashkin et al., Nature **421**,823 (2003).

[32] T. Yamamoto et al., Nature **425**, 941 (2003).